UNDERSTANDING NEUTRON ATYPICAL FEATURES IN ION IRRADIATION TESTING OF NUCLEAR MATERIALS

A Dissertation

by

YONGCHANG LI

Submitted to the Graduate and Professional School of
Texas A&M University
in partial fulfillment of the requirements for the degree of

DOCTOR OF PHILOSOPHY

Chair of Committee,	Lin Shao
Committee Members,	Tahir Cagin
	Kelvin Xie
	Karim Ahmed
Head of Department,	Ibrahim Karaman

December 2021

Major Subject: Materials Science and Engineering

ABSTRACT

Testing nuclear materials performance under extreme radiation conditions is required in materials screening and development for advanced reactors. However, the current testing reactors around the world cannot satisfy such needs due to their low efficiency in damage introduction. Ion accelerators have been widely used for the past decades to emulate reactor neutron damages, with efficiency in damage creation at least three orders of magnitudes higher than a testing reactor. However, such accelerated testing brings complexity, including the surface effect and the injected interstitials effect. We propose the methods to quantitively determine the region affected by the injected interstitial effects and the surface effects in ion-irradiated metals.

The free surface effects and the injected interstitials effect on void swelling were systematically studied based on a series of self-ion irradiation of single crystal pure Fe. The void denuded zone width Δx obtained from the summation of the width measured from TEM images and sputtering thickness loss calculated by using SRIM. Δx is linearly proportional to $(D_v/K)^{1/4}$, where D_v is the vacancy diffusivity and K is the averaged dpa rate in the near-surface region. The activation energy of Δx is $1.65 \pm 0.03\ eV$ for Fe self-ion irradiation. The sudden drop of void densities near the surface determines the region affected by the surface effect. Rate theory simulations by using MOOSE code were used for comparison. The deviation of voids sizes from the expected dpa dependence is used to define the region influenced by the interjected interstitial effects.

A safe zone map for Fe irradiated by Fe ions was established. For the 1 MeV irradiation, although voids appeared after irradiation, the whole region is affected by both the surface effect and the injected interstitials effect, and there is no safe analysis zone. Therefore, the capability to accurately identify the safe zone is critical for any attempt to use local dpa dependence to predict swelling as a function of damage level. Especially for the low energy irradiations, which were used very frequently in previous studies, it may have a narrow region that can be safely used for the analysis.

DEDICATION

To my family, my friends and everyone who have helped me and guided me in my life and studies.

ACKNOWLEDGEMENTS

I am extremely grateful to my advisor and committee chair Dr. Lin Shao, for his guidance and encouragement to my Ph.D. study. Dr. Shao has also given me a lot of help and support in my life ever since I came to Texas A&M University in 2018. His advice and support have helped me mature both in life and research. The principles and guidance he has imparted to me will continue to help me in the future.

I would like to thank my committee members, Dr. Tahir Cagin, Dr. Kelvin Xie, and Dr. Karim Ahmed, for their guidance and support throughout the research.

I would also like to thank Xuemei Wang, our lab manager. Since the first day I came to the lab, she trained me a lot on working on the accelerators. Her passion and meticulous attitude in solving problems also impressed me. I could not finish my Ph.D. research without Dr. Shao and Xuemei's support.

I would like to offer great thanks to Dr. Frank Garner for his great help on my writing and manuscript.

Finally, thanks everyone for the helps to my life and research.

CONTRIBUTORS AND FUNDING SOURCES

Contributors:

This work was supervised by a dissertation committee consisting of Professors Lin Shao and Karim Ahmed of the Department of Nuclear Engineering and Professors Tahir Cagin and Kelvin Xie of the Department of Material Science and Engineering.

The MOOSE modeling part in this study collaborated with Zhihan Hu of the Department of Nuclear Engineering.

All other work conducted for the thesis (or) dissertation was completed by the student independently.

Funding source:

Triad National Security, LLC, through award M2101345-01-47042-00001.

TABLE OF CONTENTS

Page

LIST OF FIGURES

Page

LIST OF TABLES

Page

CHAPTER 1

INTRODUCTION

This chapter will briefly introduce some advanced generation IV reactors, the mechanisms of materials degradation in reactors, the methods to test materials by using testing reactors and accelerators. The atypical neutron features will also be introduced.

1.1 Advanced Generation IV Reactors

There are 443 operable reactors in the world that produce about 394,282 MWe electricity, which is more than 10% of global electricity (As of August 2021) [1]. And also, around 57 reactors are under construction, which predicted can generate 62,694 MWe electricity [1]. In the USA, approximately 20% of the electricity was provided by using around 93 reactors.

With the increase of the worldwide electricity demand and also the cleaner energy requirement, the advanced generation IV nuclear power plants have been proposed to be the new power source in the future, which is safer, more sustainable, more economically and has low “carbon cost” than the traditional fossil fuel power plants.

Generally, the generation IV reactor including six kinds of technologies. Three thermal reactors: Molten Salt Reactor (MSR), Very High Temperature Reactor (VHTR),

Supercritical Water Reactor (SCWR), and three fast reactors: Gas-cooled Fast Reactor (GFR), Sodium-cooled Fast Reactor (SFR), Lead-cooled Fast Reactor (LFR) [2].

Compared with traditional pressurized water reactor (PWR) and boiling water reactor (BWR), materials in new generation IV reactors required higher radiation tolerance and higher operating temperature resistance, as Table 1.1 shown [3].

Table 1.1 Reactor core environment and materials for traditional light water reactors and advanced generation IV reactors [3].

System	Coolant	Pressure (MPa)	T_{in}/T_{out} (℃)	Neutron spectrum, maximum dose (dpa)	Fuel	Cladding
Pressurized water reactor (PWR)	Water (single phase)	16	290/320	Thermal, around 80 dpa	UO_2 (or MOX)	Zirconium alloy
Boiling water reactor (BWR)	Water (two phase)	7	280/288	Thermal, around 7 dpa	UO_2 (or MOX)	Zircaloy
Molten Salt Reactor (MSR)	Molten salt, like: FLiNaK	0.1	700/1000	Thermal, around 200 dpa	Salt	Not applicable

Table 1.1 Continued:

System	Coolant	Pressure (MPa)	T_{in}/T_{out} (℃)	Neutron spectrum, maximum dose (dpa)	Fuel	Cladding
Very High Temperature Reactor (VHTR)	Helium	7	600/1000	Thermal, < 20 dpa	UO_2, UCO	SiC or ZrC coating and surrounding graphite
Supercritical Water Reactor (SCWR)	Supercritical water	25	290/600	Thermal, around 30 dpa Fast, around 70 dpa	UO_2	F-M (12Cr, 9Cr, etc.) (Fe–35Ni–25Cr-0.3Ti), Incoloy 800, ODS, Inconel 690, 625, and 718
Gas-cooled Fast Reactor (GFR)	Helium, supercritical CO_2	7	450/850	Fast, around 80 dpa	MC	Ceramic
Sodium-cooled Fast Reactor (SFR)	Sodium	0.1	370/550	Fast, around 200 dpa	MOX or U-Pu-Zr or MC or MN	F-M or F-M ODS
Lead-cooled Fast Reactor (LFR)	Lead or lead-bismuth	0.1	600/800	Fast, around 150 dpa	MN	High-Si F-M, ODS, ceramics, or refractory alloys

1.2 Materials Degradation in Reactors

As discussed in the last section, the advanced generation IV reactors required higher working temperatures and longer lifetimes, which means larger irradiation and higher radiation damage level. The nuclear materials for traditional pressurized water reactors (PWR) and boiling water reactors (BWR) are no more applicable for new requirements.

Materials under such extreme environments are at huge challenges for safety, reliability, and sustainability. For example, irradiation-assisted stress corrosion cracking (IASCC) has been widely observed in light water reactors and advanced generation IV reactors due to the change of grain boundary composition and microstructure of the materials under a high neutron irradiation environment [4-5]. The stress corrosion cracking can lead to the unexpected and widespread failure of the component [6]. Figure 1.1 shows the stress cross cracking observed on nickel-based alloy 690 under irradiated and unirradiated conditions separately [7].

Irradiation hardening is another generic problem of materials in reactors [8-12]. The defect clusters generated by irradiation near the Frank-Read sources can raise the stress required to expand the loops. Also, the irradiation-induced voids and precipitates, like interstitials, will play a role in blocking dislocation loops' move, leading to the increased requirement of stress [25]. As shown in Figure 1.2, the yield strength increases for both fcc and bcc metals with the increase of irradiation dose [25]. Also, the ductility will be

reduced with increasing irradiation dose. The irradiation hardening will change the mechanical properties of nuclear materials and affect the safety of reactors.

Another very important material degradation due to radiation damage that needs to be considered is void swelling. Due to the irradiation, vacancies will be created in collision cascades. The accumulation of enormous amounts of vacancies can lead to cavities' nucleation and growth, resulting in the dimension change of the nuclear material [13-14]. For example, figure 1.3 shows around 30% void swelling that caused dimensional changes of cold-worked 316 stainless steels after around 80 dpa neutron irradiation in the EBR-II reactor [15]. Not only will it result in volume changes, void swelling will also lead to severe embrittlement and irradiation creep at elevated temperatures [16].

In this paper, all the studies are based on the void swelling data analysis.

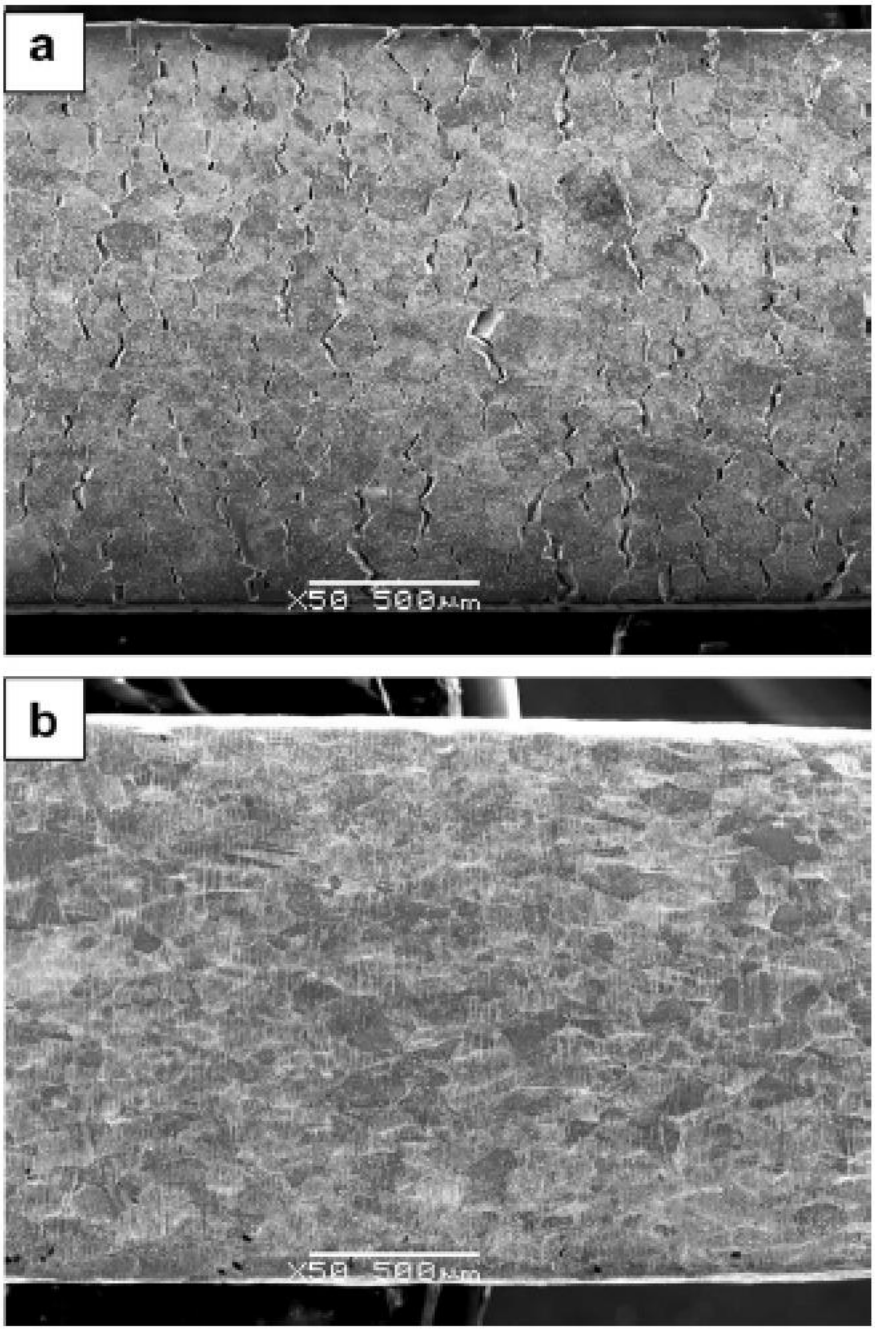

Figure 1.1(a) Stress cross cracking observed on the nickel-based alloy 690 after irradiation, (b) and under unirradiated conditions [7].

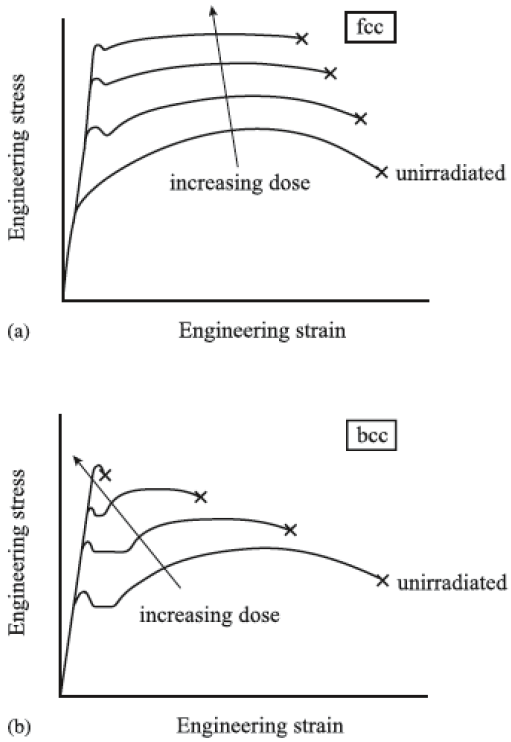

Figure 1. 2 Stress and strain curves of (a) fcc and (b)bcc metals [25].

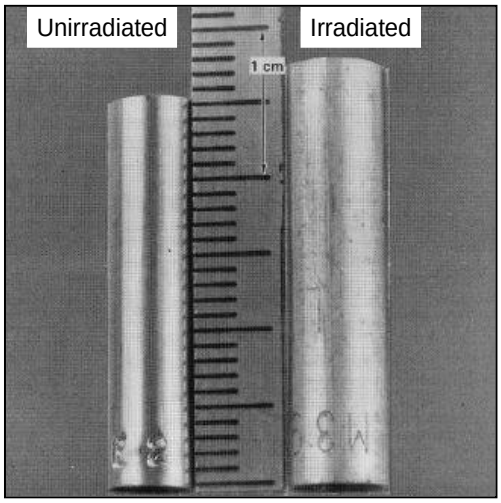

Figure 1. 3 Stress and strain curves of (a) fcc and (b)bcc metals [25].

1.3 Neutron Irradiation and Ion Irradiation

Materials in nuclear reactors are subjected to a very harsh working environment with combined radiation, stress, and high temperature effects. For generation IV reactors, the operating temperature is much higher than traditional light water reactors, as shown in table 1.1. Also, some of the new advanced generation IV reactors have a longer lifetime, which means the reactor materials will suffer higher neutron radiation damage (higher dpa). Therefore, developing new materials with better radiation and temperature tolerance becomes the critical issue of economy and safety for the advanced generation IV reactors.

The USA testing reactors, for example, Advanced Test Reactor (ATR) [17] and High Flux Isotope Reactor (HFIR) [18], can reach around ten dpa per year. Russia's fast 60MW sodium-cooled testing reactor BOR-60 [19-20] can achieve around 20 dpa every year. Obviously, the materials testing of ultra-high damage levels in advanced generation IV reactors (up to 200 dpa) will be costly and inefficient by using testing reactors. However, the damage rate of ion irradiation can be at least three orders higher than the damage by using testing reactors [21-23], as shown in Figure 1.4.

In the reactors, nuclei will collide with each other fiercely due to the recoil of very high-energy neutrons. The energy will be transferred to the atom of structure materials once the high-energy neutrons bombard it. The collision cascades will generate along the path of the energetic atom and extend the distance around a few nanometers [24]. The collision cascades produced by the atom collision are shown in Figure 1.5 [24-25]. Within a few picoseconds, after a cascade is formed, point defects (interstitials and vacancies) begin to

recombine, and the structure recovers toward its original state. However, a small fraction of the damage will be left behind without recovery. This residual damage accumulates in various ways to form various extended defects, with dislocations being a strongly biased sink for interstitials, leading to incomplete defect recombination, void nucleation, and material growth.

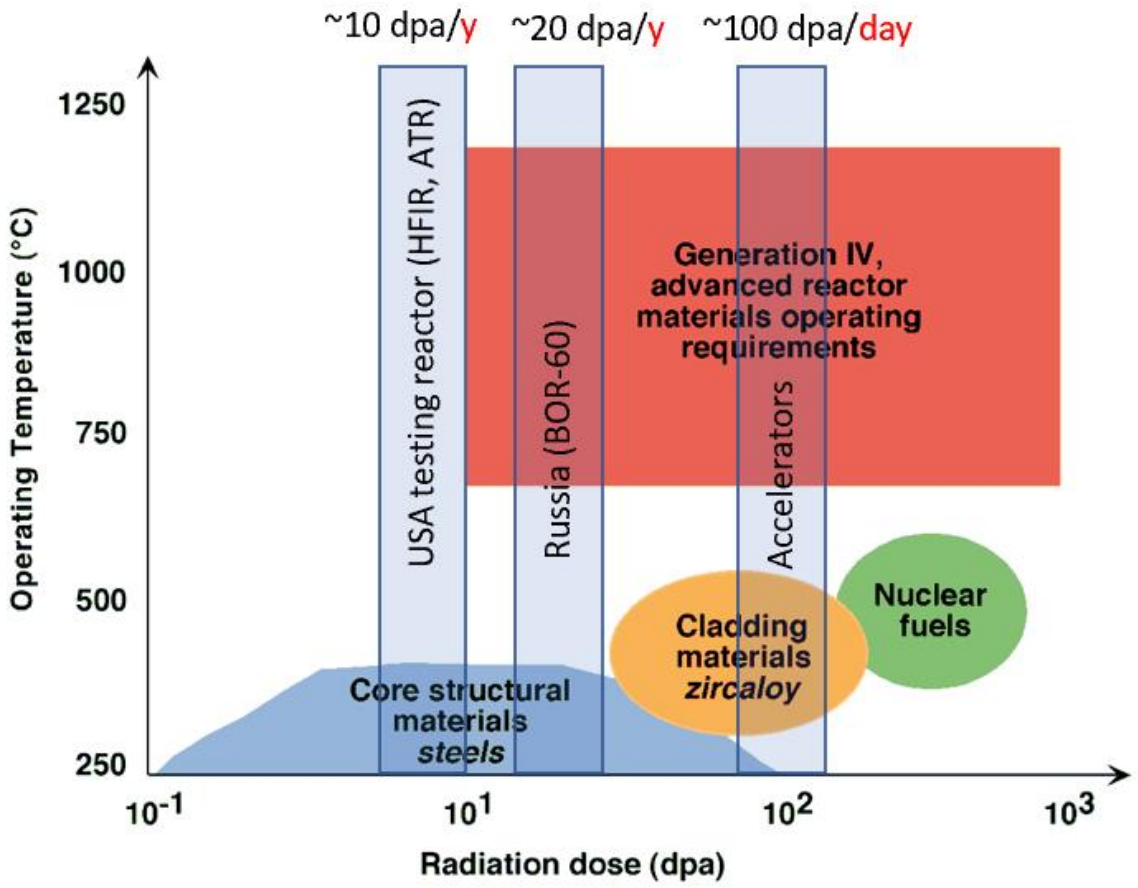

Figure 1.4 Operating conditions of advanced generation IV reactors and comparison between testing reactors and accelerators [17-23].

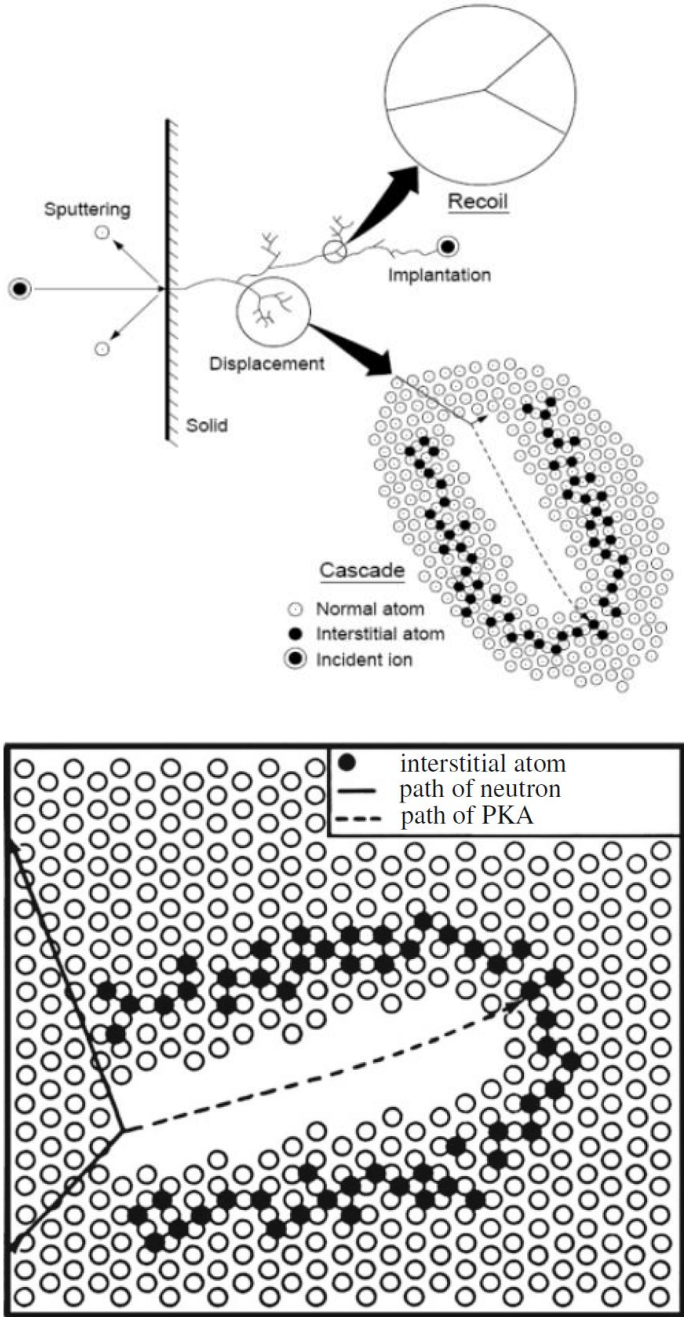

Figure 1. 5 Schematic of damage cascade produced by neutrons [24-25].

Figure 1.6 shows the damage morphology of different irradiation particles with the same energy of 1MeV on nickel. The 1 MeV electrons will generate the isolated Frenkel pairs, and protons can produce some small clusters. Larger clusters will form due to the heavy ions and neutrons irradiation [25]. Both the heavy ions and neutrons have similar average energy transfer per PKA (primary knock-on atom) and displacement efficiency. Also, both can produce dense cascades. Ion irradiation by using accelerators has been widely used as a vicarious method to test the neutron damage of nuclear materials due to the similar damage morphology of neutrons and the orders of efficiency than testing reactors, as shown in Figure 1.4.

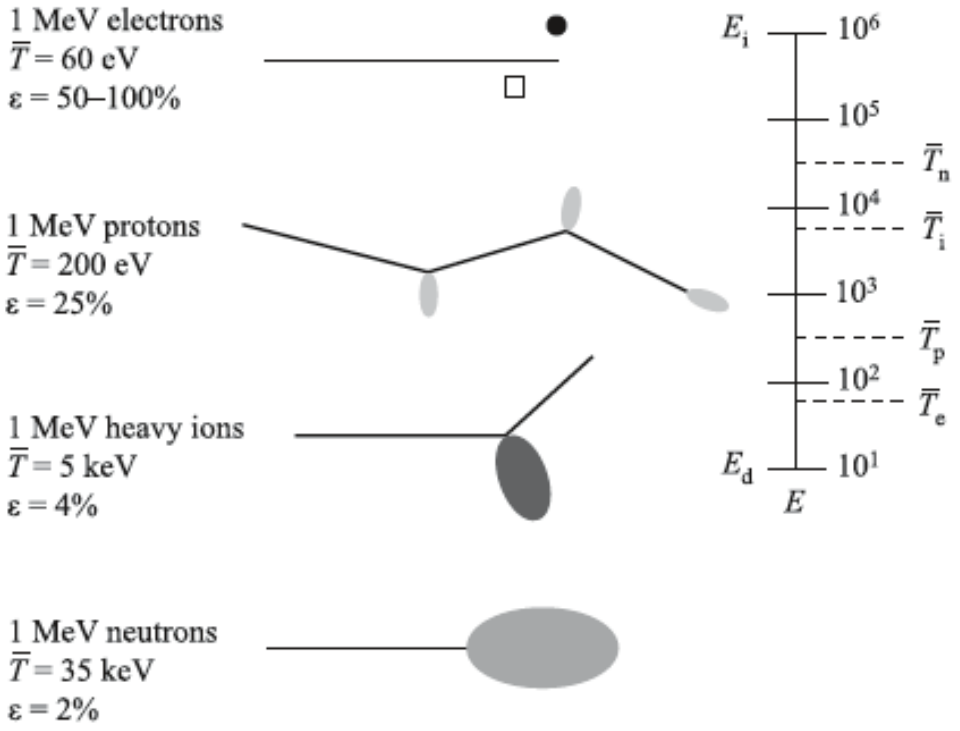

$\bar{T}$: the average energy transfer per PKA (Primary Knock-on Atom).
ϵ: the efficiency of producing freely migrating defects.
E_d: the displacement energy.
E_i: the projectile energy.

Figure 1. 6 Description of damage morphologies for irradiation with various particles of the same energy [25-26].

1.4 Neutron-Atypical Features

However, the neutron-atypical feature is a phenomenon that must be considered when doing the neutron damage analysis by using ion irradiation [25,27]. “Neutron-atypical” means it occurs only in accelerator testing but not in reactor testing. The neutron-atypical phenomenon including defect imbalance, surface defect sink effects, beam rastering effects, dpa rate effects, and carbon contamination effects [21,28-30].

Two primary neutron atypical features will be briefly introduced: defect imbalance and surface defect sink effect.

1.4.1 Defect Imbalance

In ion irradiation, interstitials and vacancies will distribute a little differently due to the collisions (both correlated and uncorrelated collisions). Generally, interstitials will distribute deeper than vacancies, and void swelling in the range of injected interstitials can be suppressed [31]. Such phenomena are defined as defect imbalance.

Figure 1.7 (a) plots the distribution of implanted 3.5 MeV iron ions calculated by using the Boltzmann Transport Equation (BTE) model [31]. The distribution is very close to the result predicted by using SRIM. Figure 1.7 (b) shows the subtle difference in the distribution between interstitials and vacancies. Figure 1.7 (c) indicates the net vacancy-rich and interstitial-rich regions calculated using the density difference values among

vacancies, interstitials, and implanted Fe ions. All values in Figure 1.7 are normalized to one incident 3.5 MeV Fe ion [31].

Because the momentum transfer from the incident ion to the host atoms is somewhat preferred to the incident direction, a vacancy will be produced. As a result, the scattered atom moves deeper and occupies the position as interstitials [31].

The defect imbalance effect is pretty strong for the incident ions with lower energy, as shown in Figure 1.8 [31]. A peak density value of the net vacancy shows at the surface, then drops in the deeper region, increases a little subsequently, and drops quickly at the deeper depth.

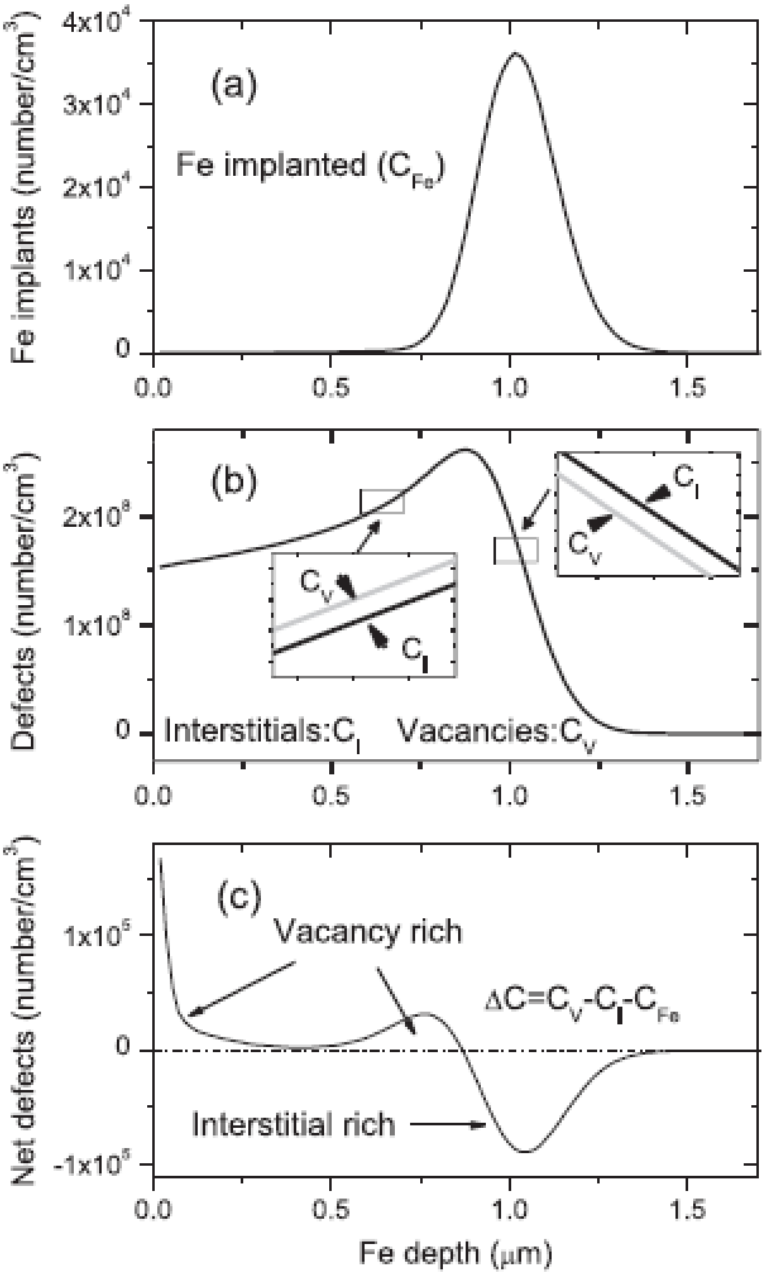

Figure 1. 7 (a) Predicted distribution of implanted 3.5 MeV Fe ions into pure Fe, (b) Predicted distribution of interstitials and vacancies, (c) Predicted vacancy rich and interstitial rich region [31]. (All values are normalized to one incident iron ion.)

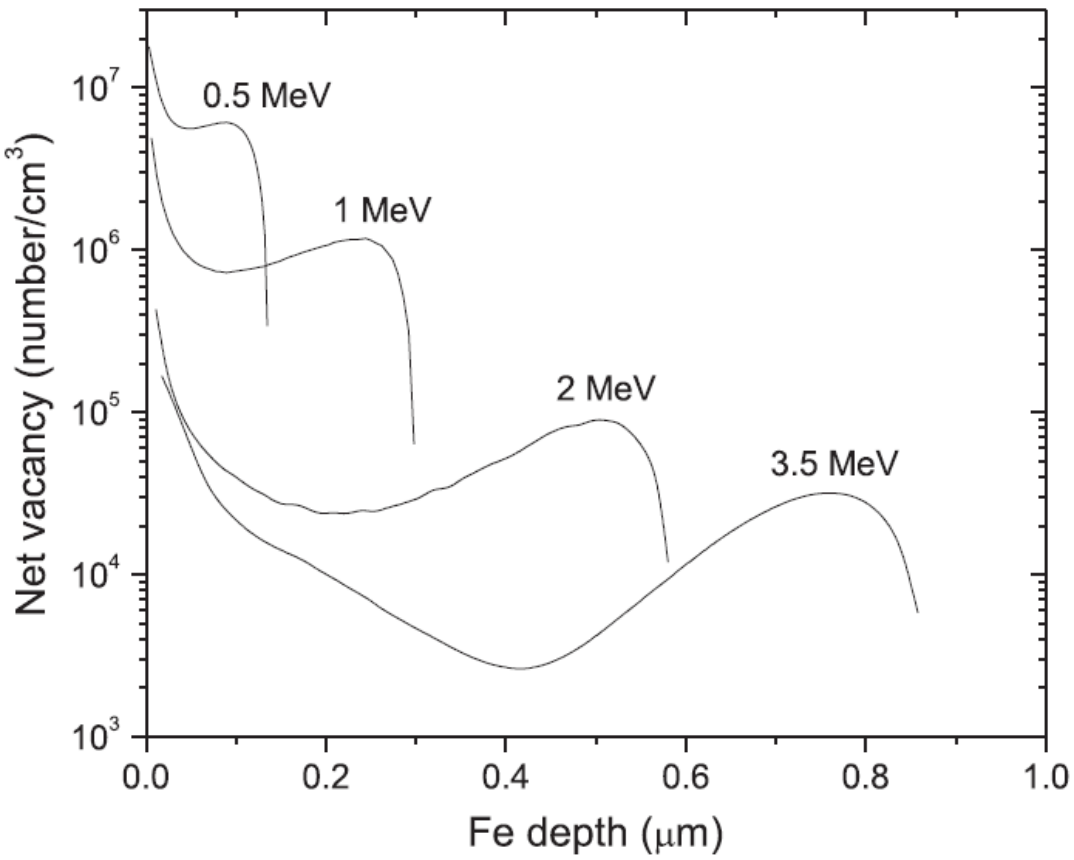

Figure 1. 8 Predicted net vacancy distribution in pure Fe irradiated by Fe ions with different energies [31].

A miscalculation of void swelling may be introduced if the studied region is selected close to the peak region of implanted ions. Since the defect imbalance effect, the void swelling will be suppressed near the peak implanted ion range. Therefore, such regions must be excluded during the studies by using ion irradiation, especially the void swelling studies, to avoid erroneous results.

However, in void swelling studies of metals irradiated by ions, this effect is not clearly understood. In chapter 4, self-ion irradiations were performed on high purity single crystal Fe with different energy and dose. Based on the void swelling data analysis, a new method will be introduced to select the survey region, which will not be affected by the defect imbalance phenomenon.

1.4.2 Surface Defect Sink Effect

As the vacancy-rich region shown in Figure 1.7 and Figure 1.8, the void nucleation is expected to occur at the first time and have a peak value of void swelling in the vicinity of the surface. However, the experiment result shows a suppressed void swelling in the near-surface region, as Figure 1.9 shown [31]. Since the surface will act as sinks to remove point defects, for example, interstitials and vacancies [32-34], then a denuded zone will form due to the loss of defects (interstitials and vacancies), and the void swelling will be suppressed at the surface.

The surface defect sink effect in void swelling will affect the reliability of ion irradiation. However, on the other hand, it can be used to remove defects by introducing internal free surfaces in materials engineering [35]. The strong effect of internal free surface to void swelling has been reported [36].

In Figure 1.10 (a), the high purity Fe was irradiated by 3.5 MeV Fe ions at 475℃ with the dose of 150 peak dpa [36], a small denuded zone with the depth around 100nm was observed by using transmission electron microscopy (TEM). In Figure 1.10 (b), a trench

was made by using the technique of focused ion beam at the depth of 1.7 μm under the surface. As Figure 1.10 (a) shown, this position is beyond the region of any injected Fe ions, then there should be no significant interstitials loss to the trench [36]. After irradiation, a wider denuded zone, around 400 nm, was observed at the surface. Figure 1.10 (c) provides the TEM micrograph with a trench at the depth of 1.16 μm, where is short of the peak implanted region [31, 36]. It clearly shows that the swelling was eliminated by the denuded zone, and all the voids were removed by free surfaces.

The region of the void denuded zone is easy to be avoided from the observation of TEM micrographs. However, the deeper region where voids formed may still be affected by the surface if the vacancy supersaturation is high enough to nucleate voids under the diminishing effect of point defects. Thus, the results may be imprecise if the testing region for nuclear materials using ion irradiation is not deep enough to avoid any surface effect.

In chapter 3, self-ion irradiations were performed on high purity single crystal Fe with different energy and dose. Based on the void swelling data analysis, a quantitative method is provided to define the surface affected zone based on self-consistency of swelling dependence on local dpa values.

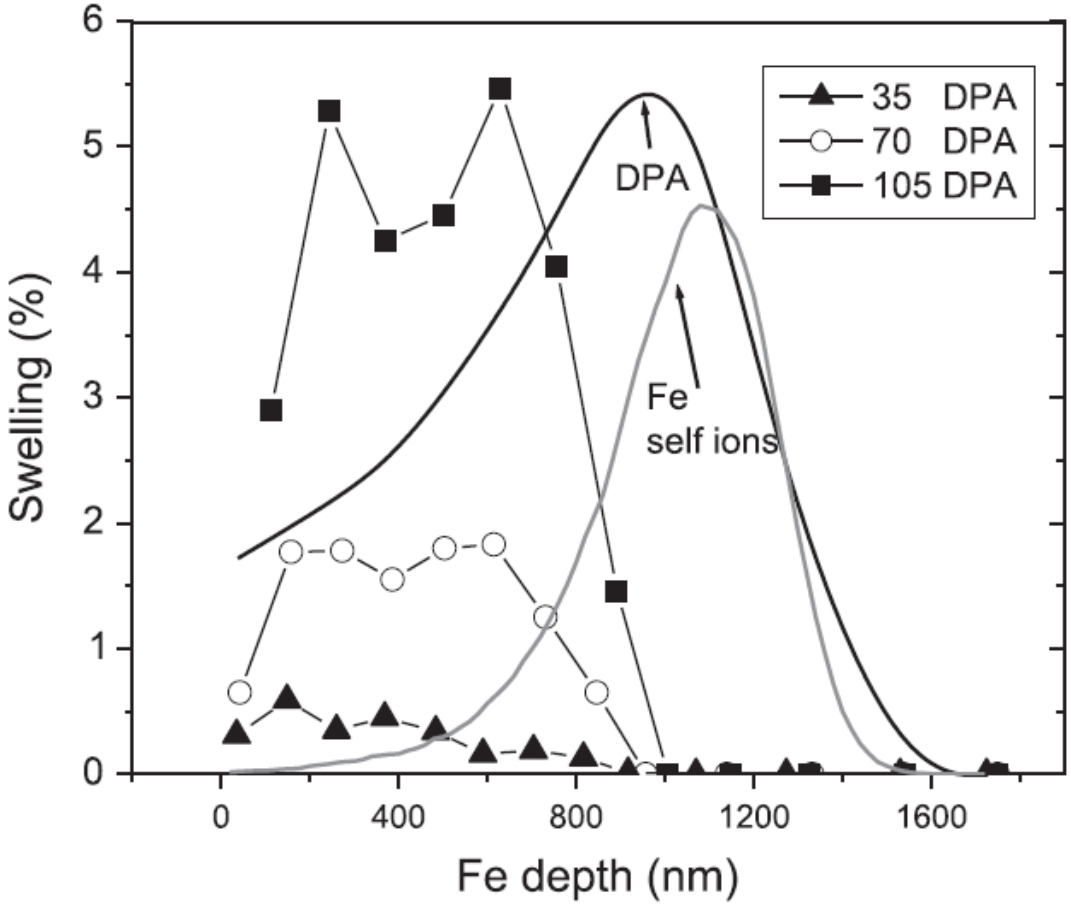

Figure 1. 9 Predicted net vacancy distribution in pure Fe irradiated by Fe ions with different energies [31].

(a)

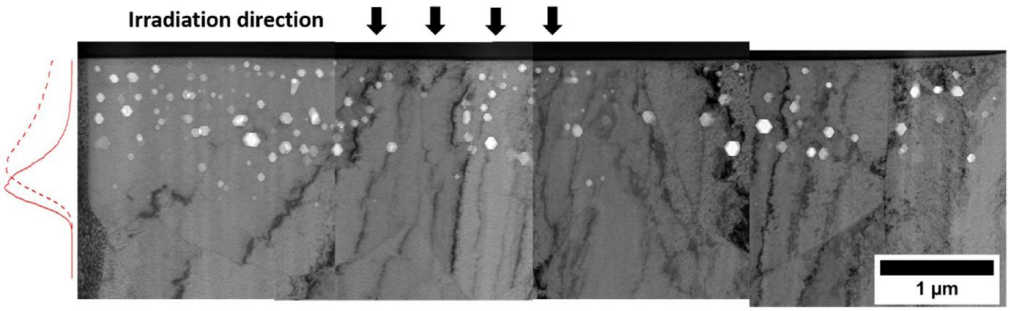

(b)

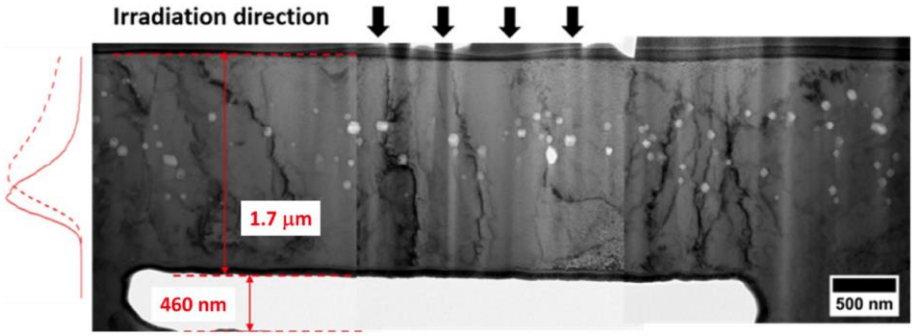

(c)

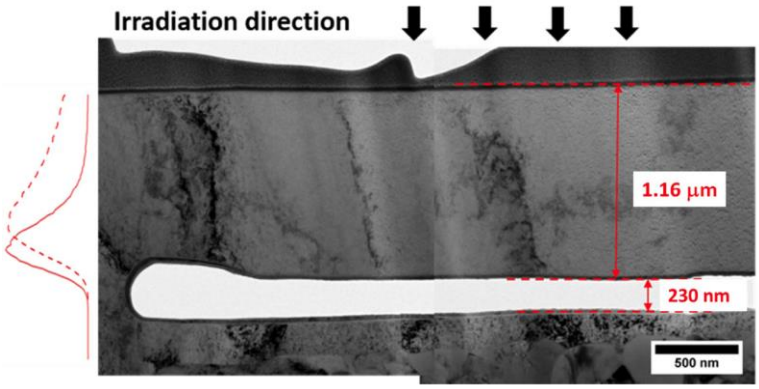

Figure 1. 10 (a) TEM micrograph of irradiated Fe without any trench; (b) TEM micrograph of irradiated Fe with the trench at depth 1.7 μm; (c) TEM micrograph of irradiated Fe with the trench at depth 1.16 μm [26].

Reference

[1] www.world-nuclear.org, 2021.

[2] Locatelli, Giorgio, Mauro Mancini, and Nicola Todeschini. "Generation IV nuclear reactors: Current status and future prospects." Energy Policy 61 (2013): 1503-1520.

[3] Zinkle, Steven J., and G. S. Was. "Materials challenges in nuclear energy." Acta Materialia 61, no. 3 (2013): 735-758.

[4] Scott, P. "A review of irradiation assisted stress corrosion cracking." Journal of nuclear materials 211, no. 2 (1994): 101-122.

[5] Sieradzki, Karl, and R. C. Newman. "Stress-corrosion cracking." Journal of physics and chemistry of solids 48, no. 11 (1987): 1101-1113.

[6] Was, Gary S., and Stephen M. Bruemmer. "Effects of irradiation on intergranular stress corrosion cracking." Journal of nuclear materials 216 (1994): 326-347.

[7] Teysseyre, S., Z. Jiao, E. West, and G. S. Was. "Effect of irradiation on stress corrosion cracking in supercritical water." Journal of nuclear materials 371, no. 1-3 (2007): 107-117.

[8] Xiao, Xiazi. "Fundamental mechanisms for irradiation-hardening and embrittlement: a review." Metals 9, no. 10 (2019): 1132.

[9] Hunn, J. D., E. H. Lee, T. S. Byun, and L. K. Mansur. "Ion-irradiation-induced hardening in Inconel 718." Journal of nuclear materials 296, no. 1-3 (2001): 203-209.

[10] Hu, Xunxiang, Takaaki Koyanagi, Makoto Fukuda, NAP Kiran Kumar, Lance L. Snead, Brian D. Wirth, and Yutai Katoh. "Irradiation hardening of pure tungsten exposed to neutron irradiation." Journal of Nuclear Materials 480 (2016): 235-243.

[11] Azevedo, C. R. F. "A review on neutron-irradiation-induced hardening of metallic components." Engineering Failure Analysis 18, no. 8 (2011): 1921-1942.

[12] Pokor, C., Y. Brechet, P. Dubuisson, J-P. Massoud, and X. Averty. "Irradiation damage in 304 and 316 stainless steels: experimental investigation and modeling. Part II: Irradiation induced hardening." Journal of nuclear materials 326, no. 1 (2004): 30-37.

[13] Garner, F. A., L. Shao, M. B. Toloczko, S. A. Maloy, and V. N. Voyevodin. "Use of self-ion bombardment to study void swelling in advanced radiation-resistant alloys." In 17th Int. Symp. Conf. on Environmental Degradation of Materials in Nuclear Power Systems, Ottawa, Canada, vol. 325. 2015.

[14] Mansur, Louis Kenneth. "Void swelling in metals and alloys under irradiation: an assessment of the theory." Nuclear Technology 40, no. 1 (1978): 5-34..

[15] Mansur, L. K. "Theory and experimental background on dimensional changes in irradiated alloys." Journal of Nuclear Materials 216 (1994): 97-123.

[16] Chen, Y., Yong Yang, Yina Huang, T. Allen, B. Alexandreanu, and K. Natesan. Void Swelling and Microstructure of Austenitic Stainless Steels Irradiated in the BOR-60 Reactor. No. NUREG/CR-7128. Argonne National Lab.(ANL), Argonne, IL (United States), 2012.

[17] Thelen, Mary Catherine, and Todd R. Allen. Advanced Test Reactor National Scientific User Facility 2010 Annual Report. No. INL/EXT-11-21785. Idaho National Laboratory (INL), 2011.

[18] https://neutrons.ornl.gov/hfir, 2021.

[19] Izhutov, ALEXEY L., Yuri M. Krasheninnikov, Igor Y. Zhemkov, ARTEM V. Varivtsev, Yuri V. Naboishchikov, Victor S. Neustroev, and Valentin K. Shamardin. "Prolongation of the BOR-60 reactor operation." Nuclear Engineering and Technology 47, no. 3 (2015): 253-259.

[20] http://www.niiar.ru/eng/node/224, 2021

[21] Shao, Lin, Jonathan Gigax, Di Chen, Hyosim Kim, Frank A. Garner, Jing Wang, and Mychailo B. Toloczko. "Standardization of accelerator irradiation procedures for simulation of neutron induced damage in reactor structural materials." Nuclear Instruments and Methods in Physics Research Section B: Beam Interactions with Materials and Atoms 409 (2017): 251-254.

[22] Was, G. S., Z. Jiao, E. Getto, K. Sun, A. M. Monterrosa, S. A. Maloy, O. Anderoglu, B. H. Sencer, and M. Hackett. "Emulation of reactor irradiation damage using ion beams." Scripta Materialia 88 (2014): 33-36.

[23] Zinkle, S. J., and L. L. Snead. "Opportunities and limitations for ion beams in radiation effects studies: Bridging critical gaps between charged particle and neutron irradiations." Scripta Materialia 143 (2018): 154-160.

[24] Nastasi, Michael, Nastasi Michael, James Mayer, James K. Hirvonen, and Mayer James. Ion-solid interactions: fundamentals and applications. Cambridge University Press, 1996.

[25] Was, Gary S. Fundamentals of radiation materials science: metals and alloys. springer, 2016.

[26] Was, Gary S., and T. Allen. "Radiation-induced segregation in multicomponent alloys: Effect of particle type." Materials characterization 32, no. 4 (1994): 239-255.

[27] Stiegler, J. O. Proceedings of the workshop on correlation of neutron and charged particle damage. No. CONF-760673-. Oak Ridge National Lab., Tenn.(USA), 1976.

[28] Garner, F. A. "Impact of the injected interstitial on the correlation of charged particle and neutron-induced radiation damage." Journal of Nuclear Materials 117 (1983): 177-197.

[29] BREEDEN, BRENDA K. "RADIATION EFFECTS and TRITIUM TECHNOLOGY FUSION REACTORS." (1976).

[30] Shao, Lin, Xinming Lu, Xuemei Wang, Irene Rusakova, Jiarui Liu, and Wei-Kan Chu. "Retardation of boron diffusion in silicon by defect engineering." Applied Physics Letters 78, no. 16 (2001): 2321-2323.

[31] Shao, Lin, C-C. Wei, J. Gigax, A. Aitkaliyeva, D. Chen, B. H. Sencer, and F. A. Garner. "Effect of defect imbalance on void swelling distributions produced in pure iron irradiated with 3.5 MeV self-ions." Journal of Nuclear Materials 453, no. 1-3 (2014): 176-181.

[32] Sun, C., D. Bufford, Y. Chen, M. A. Kirk, Y. Q. Wang, M. Li, H. Wang, S. A. Maloy, and X. Zhang. "In situ study of defect migration kinetics in nanoporous Ag with enhanced radiation tolerance." Scientific reports 4, no. 1 (2014): 1-6.

[33] Beyerlein, I. J., A. Caro, M. J. Demkowicz, N. A. Mara, A. Misra, and B. P. Uberuaga. "Radiation damage tolerant nanomaterials." Materials today 16, no. 11 (2013): 443-449.

[34] Bringa, Eduardo Marcial, J. D. Monk, A. Caro, A. Misra, L. Zepeda-Ruiz, M. Duchaineau, F. Abraham et al. "Are nanoporous materials radiation resistant?." Nano letters 12, no. 7 (2012): 3351-3355.

[35] Zhang, Xinghang, Khalid Hattar, Youxing Chen, Lin Shao, Jin Li, Cheng Sun, Kaiyuan Yu et al. "Radiation damage in nanostructured materials." Progress in Materials Science 96 (2018): 217-321.

[36] Wang, Tianyao, Hyosim Kim, Frank A. Garner, Kenneth L. Peddicord, and Lin Shao. "The Effect of Internal Free Surfaces on Void Swelling of Irradiated Pure Iron Containing Subsurface Trenches." Crystals 9, no. 5 (2019): 252.

CHAPTER 2

EXPERIMENT DESIGN AND PROCEDURE

In this chapter, the whole process, including specimen preparation, equipment, experiment design, and data characterization, will be introduced in detail. The sample preparation is the first and also very important step of the research, a clean sample with high purity can significantly improve the quality of the experiment and make the result more accurate. Single crystal pure Fe with the purity of 99.94+% was used in the study. All the samples were irradiated by using the Pelletron 3 MV Tandem accelerator with the energy of 1MeV, 2.5MeV, 3.5MeV, and 5MeV Fe^{2+} ions in the Texas A&M accelerator laboratory. The focused ion beam (FIB) and transmission electron microscope (TEM) techniques were used to analyze the data.

2.1 Sample Preparation

Fe of purity 99.94+% with the orientation of <111> were selected to use in the research. The use of single crystalline materials can avoid the effects of grain boundaries and minimize the data fluctuations caused by crystalline orientation dependence.

2.1.1 Sample Cutting and Polishing

The single crystal pure Fe used in this research was ordered from Accumet Materials Inc., Ossining, NY, USA. Float zone refining, Czochralski, or Bridgman techniques are

used to manufacturing these single crystal metals [1-4]. The purchased single crystal irons have the size of 5mm×5mm×1mm, they were cut into 3mm×3mm×1mm samples by using the Extec Labcut 150 cutter in our lab, as shown in Figure 2.1. The diamond cutoff saw was used in this cutter.

ACE Nano 2000T Grinder-polisher, as Figure 2.2 shows, was used to do the mechanical polishing for these single crystal pure Fe samples. First, the rough 600, 1200 SiC grit papers were used to remove the damage and deformation produced during the cutting process. Then, the 2400 grit SiC paper and 4000 grit SiC paper were used to remove the cosmetic damage on the surface for the final polishing. After that, specimens were immersed into acetone and cleaned by using the Ultrasonic cleaner. Finally, electropolishing was employed to further improve the quality of the specimen surface and remove the stress surface layer introduced by mechanical polishing.

Specimens used in the study were all electropolished by using TenuPol-5 electropolisher, as shown in Figure 2.3, with the solution of 5 vol% perchloric acid and 95 vol% methanol. The applied voltage is 20 V with an operating temperature of -20 ℃.

Figure 2.1 The Extec Labcut 150 cutter used in the study.

Figure 2.2 ACE Nano 2000T Grinder-polisher.

Figure 2. 3 TenuPol-5 electropolisher in MCF, Texas A&M University.

2.1.2 Sample Surface Quality Check

The penetration depth of 5 MeV Fe2+ is around 1.7 μm, and the ion range of 1MeV Fe2+ is only around 400 nm in Fe. In this study, the data analysis is closely related to the depth-dependent microstructure characterization. Thus, it is very important to ensure the specimen has a smooth and clean surface before any experiments.

The scanning electron microscope (SEM) was used on the Tescan LYRA-3 FIB-SEM instrument to check the surface quality. Figure 2.4 shows the SEM image of one of the single crystal pure Fe before and after mechanical polishing and electropolishing. These images were taken under 10 kV operation voltage with the magnification of 2.74 kx. The surface is generally smooth and clean after polishing, but still some small pits can be

observed in the figure, they are possibly generated during the electropolishing process due to the defect or dislocations result in the etching rate difference. Nevertheless, the clean and pits-free area is large enough for the data analysis.

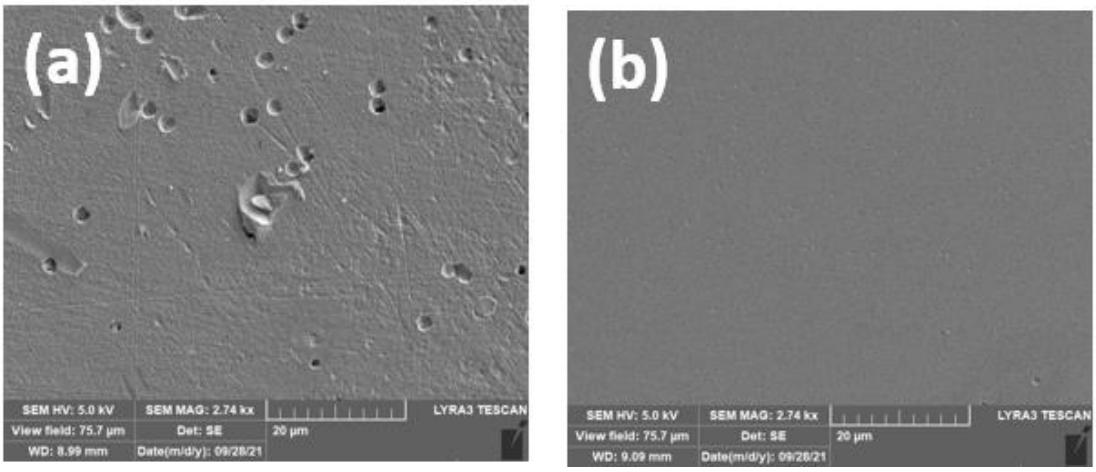

Figure 2.4 SEM images of the surface of a single crystal pure Fe (a) before and (b) after polishing.

2.2 Self-ion Irradiation by Using Accelerator

As discussed in Chapter 1, accelerators have been widely used as a vicarious method to test the neutron damage of materials due to the high efficiency and economy than testing in reactors. This study used the Pelletron 3 MV Tandem accelerator (model 9SDH-2), made by National Electrostatics Corporation (NEC), for self-ion irradiation.

2.2.1 Background of Accelerator

The Pelletron 3 MV Tandem accelerator (model 9SDH-2) was designed and manufactured by National Electrostatics Corporation (NEC). Figure 2.5 and Figure 2.6 show the picture and schematic of the 3MV accelerator in our lab. It has two sources, one is the Source of Negative Ions by Cesium Sputtering (SNICS) for heavy ions, like iron, copper, tungsten, and gold. It can also be used for proton irradiation. The other source is RF Charge Exchange Ion Source (Alphatross), this source is primarily used to produce He- beams but can also produce H^-, NH^-, and O^- beams. In this study, Fe self-ion irradiation was performed on the single crystal pure iron by using SNICS source. The SNICS source will be introduced in this section.

Figure 2.5 The picture of Pelletron 3 MV Tandem accelerator.

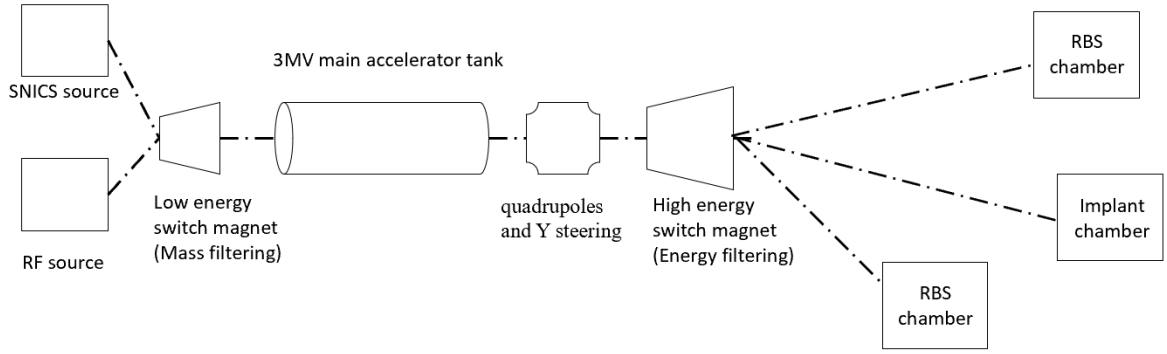

Figure 2.6 The schematic of Pelletron 3 MV Tandem accelerator.

Figure 2.7 shows the picture and schematic of the SNICS source. During irradiation, the oven generally will be heated to higher than 100℃, the cesium reserved in the oven will be evaporated to an area between the cathode, iron cathode was used in this study, and ionizer. The ionizer coils will also be heated to high temperature, and then thermal electrons can be produced. A part of Cs vapor will be ionized on the ionizer and become Cs^+ ions, and the others will condense on the cooled Fe cathode surface and form a thin Cs layer, as Figure 2.7 (b) shown. Under the target voltage, Cs^+ will bombard to the cathode and sputter Fe particles from the cathode surface through a condensed cesium layer. Fe^- ions are generated during the sputtering process due to the low electron affinity of Cs. Then, these negative ions are accelerated back toward the ionizer due to target voltage and focused into a negative beam.

However, some other kinds of negative beams will also be produced during the sputtering process, such as H^-, C^- and O^- ions, due to the impurity of the cathode. Thus, a

switch magnet is introduced to select the element with a certain mass based on the Lorentz force equation (2-1) and centripetal force equation (2-2).

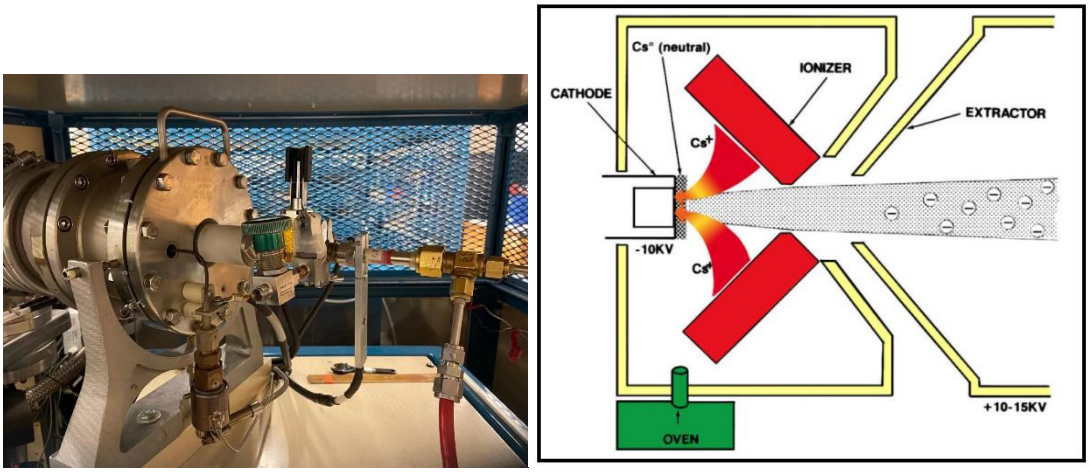

Figure 2.7 (a) Picture of SNICS source in our lab, (b) Schematic of the cesium sputtering operation produced by the SNICS [5].

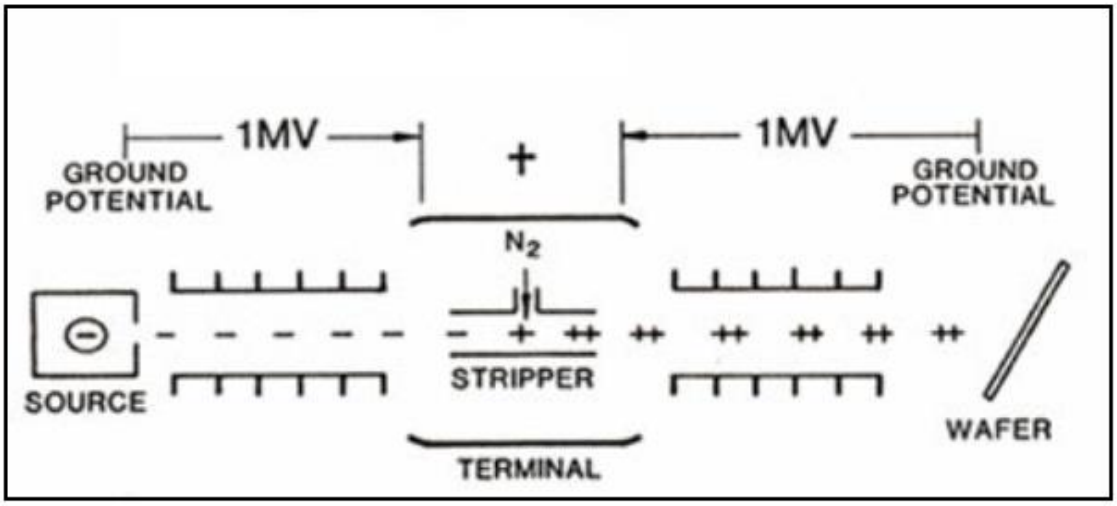

Figure 2.8 Schematic of the internal structure of main accelerator tank [6].

$$F = qvB \tag{2-1}$$

$$F = mv^2/r \tag{2-2}$$

Also, based on the kinetic energy equation:

$$E = \frac{1}{2}mv^2 \tag{2-3}$$

The relationship between magnetic flux density and ion's characteristics can be given:

$$q^2B^2 = 2Em/r \tag{2-4}$$

Here, q is the charge of ions, all ions have a charge of -1 in the low energy switch magnet; v is the velocity of ions; B is the magnetic flux density of the switch magnet; the kinetic energy E of ions depends on the cathode voltage and extraction voltage at the low energy side; r is the curvature of the ion's path in switch magnet field, it should be a constant for the given beamline.

In this study, Fe^- ions are selected to pass through the low energy switch magnet and bend into the main accelerator tank based on equation (2-4). Then, due to the high voltage terminal at the center of the tank, as shown in Figure 2.8, these Fe^- ions are accelerated toward the high voltage part. At the center, negative ions stop, and electrons will be stripped by nitrogen. As a result, positive ions Fe^{n+} are generated. The charge number n depends on how many electrons are lost and will continue to be accelerated. Subsequently, double charge ions Fe^{2+} are selected by the high energy switch magnet, based on equation (2-4), bend toward to the irradiation chamber.

2.2.2 Experiment Process

2.2.2.1 Defocused Beam

The beam scanning method is frequently selected to get a uniform beam area. However, the study found that the scanning, also called the rastering method, will affect void swelling and void density. The effect capability mainly depends on the scanning frequency [7]. Figure 2.9 shows the TEM micrographs for 3.5 MeV Fe^{2+} irradiation to pure iron with the temperature of 450 ℃ with rastered beam at different frequencies and irradiate with a defocused beam [7]. Compared with the defocused beam, it clearly shows that void density will decrease, and swelling will reduce with the increased scanning frequency [7]. To avoid such pulsing effect, the defocused beam is used in this study.

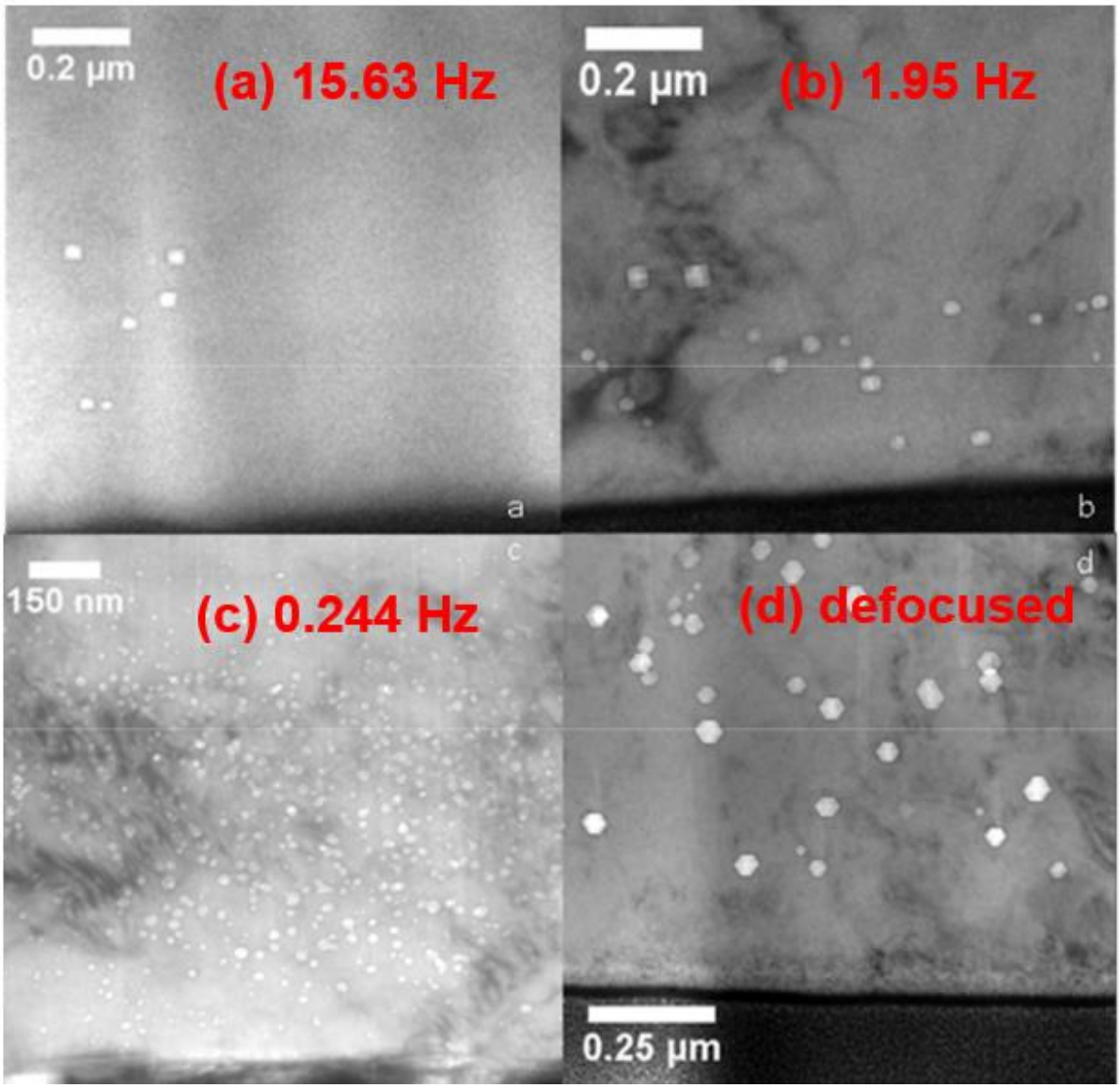

Figure 2.9 TEM figure for 3.5 MeV Fe2+ irradiation to pure iron with rastered beam at. (a) 15.63 Hz, (b) 1.95 Hz, (c) 0.244 Hz, and a (d) defocused beam. [7]

2.2.2.2 Beam deflection

Contamination of ion-bombarded surfaces is a well-known issue for various diagnostic and ion-modification techniques operating for minutes to hours of exposure. The contaminations (including C, O, and N) become severe when using high-flux ion beams over days of exposure to reach very high dpa levels. Our lab recently demonstrated that the primary source of carbon contamination on the specimen surface is due to the Coulomb drag imparted by the beam on the carbon atoms or other negatively charged elements within the beam pipeline [8]. For this study, a sequential beam deflection technique developed by us was used to significantly reduce carbon contamination. The key is to use multiple beam deflection to filter the contaminants out of the Fe beam due to their mass/charge difference. Figure 2.10 shows the schematic of the deflection process.

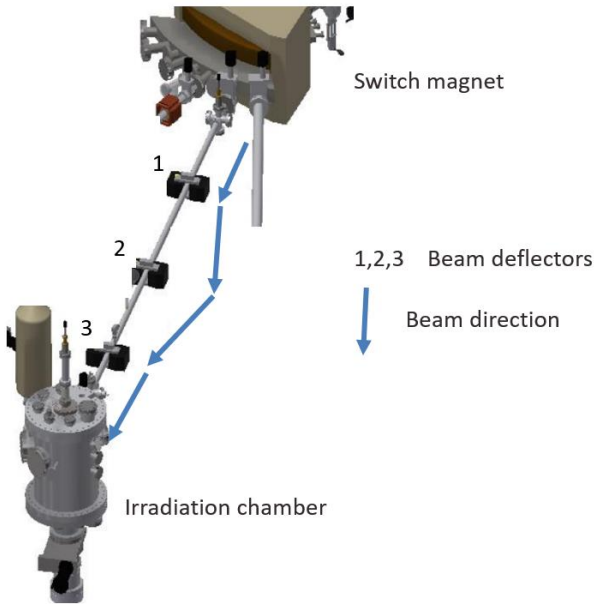

Figure 2.10 Schematic of the deflection working process.

2.2.2.3 Sample Mount and irradiation

After defocus and deflection, the iron beam has arrived at the target irradiation chamber. The last step before the irradiation is to decide the certain area and position of the beam to mount the sample. First, a piece of clean copper tape is pasted on the hot stage like Figure 2.11 (a) shown and burn by using the beam. Then, the sample will be mount on this specific area by using the silver paste, as shown in Figure 2.11 (b). Generally, the beam area is larger than the sample to ensure the interesting area can be fully covered. Figure 2.11 (c) shows a picture of the hot stage with the mounted sample in the irradiation chamber. It was heating by using a bulb.

(a) (b) (c)

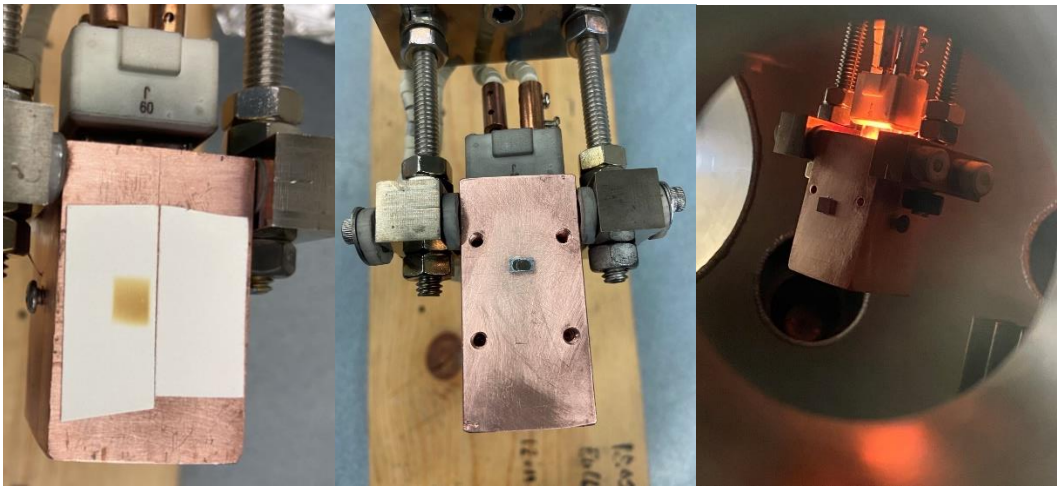

Figure 2.11 The picture of (a) A uniform beam burned area on the copper tape; (b) A single crystal pure Fe mounted on the stage by using silver paste; (c) A heating hot stage with the mounted sample in the irradiation chamber.

The other important parameter that needs to be confirmed before the experiment is the irradiation time. It can be decided by using equation (2-5).

$$Irradiation\ time\ [s] = \frac{Total\ fluence\ [\#\ of\ ions/cm^2]}{irradiation\ flux\ [\frac{\#\ of\ ions}{cm^2 \cdot s}]} \quad (2\text{-}5)$$

The flux depends on beam area and beam current:

$$Flux\ \left[\frac{\#}{cm^2 \cdot s}\right] = Beam\ current\ [A] \cdot \frac{1}{1.602 \times 10^{-19}[C]} \cdot \frac{1}{Beam\ area\ [cm^2]} \times \frac{1}{q} \quad (2\text{-}6)$$

Where q denotes the ion charge.

The total fluence is related to the interested peak dpa (displacement per atom) value. It can be calculated by using SRIM based on the Kinchin-Pease (KP) mode [9], and the displacement energy for single crystal pure iron is selected as 40 eV [10]. During irradiation, the vacuum was about 6×10-8 torr or better in the target chamber with the help of a liquid nitrogen trap. The temperature was kept within ± 5 ℃.

2.2.3 Experiment Matrix

Tables 2.1, 2.2, and 2.3 show the experiment matrix in the study. The energy dependent studies were carried out by using 5 MeV Fe^{2+} ions with the peak dpa of 50, 100, and 150 to electropolished single crystal pure Fe, under the roughly same dpa rate, $1.2 \times 10^{-3} dpa/s$, with fluctuation less than $0.1 \times 10^{-3} dpa/s$. The temperature is selected as 475 ℃, which is close to the maximum swelling temperature of pure iron [11-

14]. Also, at the same dpa rate and temperature, experiments were performed by Fe^{2+} ions of 1 MeV, 2.5 MeV, 3.5 MeV, respectively, to 50 and 100 peak dpa.

For the dpa rate dependent studies, single crystal pure Fe samples were irradiated by 5 MeV Fe2+ ions with different dpa rates, $2 \times 10^{-4} dpa/s$, $3 \times 10^{-4} dpa/s$, $1.2 \times 10^{-3} dpa/s$, and $6 \times 10^{-3} dpa/s$, respectively. the irradiation temperatures are fixed as 475 ℃.

Also, temperature dependent studies were performed on single crystal pure Fe irradiated by 5 MeV Fe^{2+} ions. The irradiation temperatures are 425 ℃, 475 ℃, and 525 ℃, respectively. The dpa rates are fixed as $6 \times 10^{-3} dpa/s$ for all irradiations.

Table 2.1 Experiment matrix at the dpa rate of 1.2×10^(-3) dpa/s with different energies and doses, the irradiation temperature is selected as 475 ℃.

Dose (DPA) / Energy (MeV)	50	100
1	475 ℃	475 ℃
2.5	475 ℃	475 ℃
3.5	475 ℃	475 ℃
5	475 ℃	475 ℃

Table 2.2 Experiment matrix of dpa rate dependent studies.

Dpa rate (dpa/s) / Temperature (℃)	2×10^{-4}	3×10^{-4}	1.2×10^{-3}	6×10^{-3}
475	5MeV	5MeV	5MeV	5MeV

Table 2.3 Experiment matrix of temperature dependent studies

Temperature / Dpa rate (dpa/s)	425 ℃	475 ℃	525 ℃
6×10^{-3}	5MeV	5MeV	5MeV

2.3 Specimen Characterization

After irradiation, the specimens need to do some preparation for the following analysis.

2.3.1 Focused Ion Beam (FIB)

The focused ion beam with kilo electron volt incident to the materials can sputter off atoms from the materials surface, induce chemical reactions, or deposit the incident ions on the materials [15]. The sputtering effect has been widely used as a technique to prepare TEM lamellas.

Figure 2.12 is the photo of the Tescan LYRA-3 Focused Ion Beam Microscope used in this study. It has a liquid metal ion source, gallium (Ga), due to its low melting point, stored in a reservoir connected with a very sharp Tungsten needle. After high voltage and ionization accelerate, gallium ions will be emitted with high energy [16]. The beam current can be changed from several picoamperes to several nano amperes. The LYRA-3 FIB instrument has both the SEM and FIB system together, as Figure 2.13 shown. The SEM system can produce secondary or backscattering electrons during the FIB system to obtain a real-time sample image.

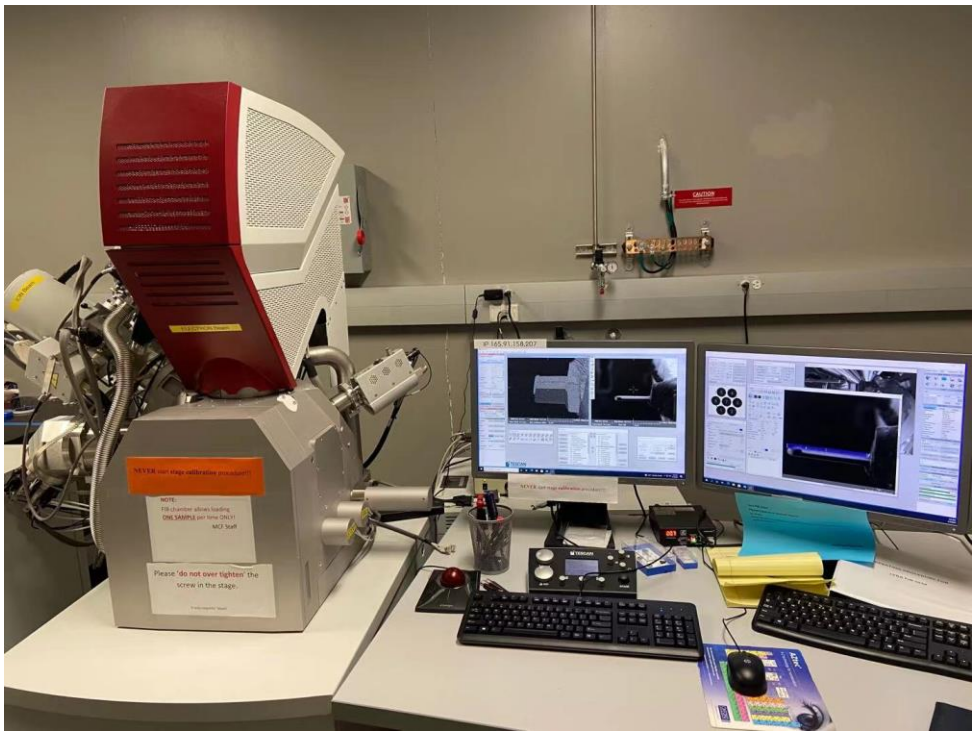

Figure 2.12 Photo of the Tescan LYRA-3 Model GMH Focused Ion Beam Microscope in MCF, Texas A&M University.

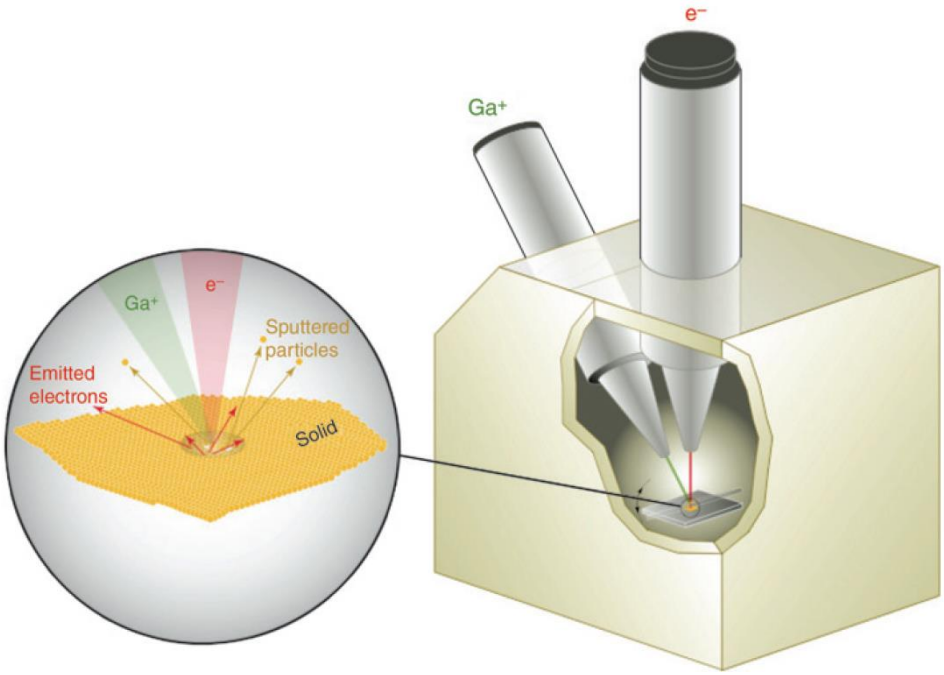

Figure 2.13 Schematic of the dual-beam FIB-SEM instrument [17].

Figure 2.14 shows the TEM lamella lift-out process by using FIB. At first, a platinum (Pt) layer is deposited on the sample surface, where is the electropolished irradiated region, with the size of 12 μm ×3 μm and the thickness is around 3μm as shown in Figure 2.14 (a). The Pt layer plays a role in protecting the sample surface from the damage of Ga ions during etching. Figure 2.14 (b) shows the SEM image after etching around the Pt layer by using FIB, the lamella has a thickness of around one μm at this step and the trench near it has a depth around 5 to 6 μm. Then, the U-cut method, also called C-cut method, is used to cut off the connections on the bottom and left edge and part of the right edge. This step is shown in Figure 2.14 (c).

A thin tungsten (W) needle, generally the tip thickness is less than 3 μm, is inserted by the manipulator and will be connected with the lamella edge by using Pt, as the SEM image shown in Figure 2.14 (d). In Figure 2.14 (e), this figure was taken in the In-Beam BSE (backscattered electrons) mode, which shows the clear contrast between the Pt layer and single crystal pure Fe. Because the backscattered electrons come from the deeper region compare to the secondary electrons come from the surface, BSE will generate the image with different contrast for different atomic mass [18-19]. The higher the atomic mass, the brighter the image, just like Figure 2.14 (e) shown.

Once the W needle has been attached to the lamella, it can be lifted out by cutting off the final connection, shown in Figure 2.14 (f). Figure 2.14 (g) and (h) show the process that the lamella, with a thickness around 1 μm, will be attached on a TEM grid by Pt deposition. However, a thin lamella with a thickness less than 200 nm is required to get a clear TEM image. Therefore, the lamella should be thinned by using the low current beam. Figure 2.14 (i) and (j) show the SEM and BSE images of the lamella after thinning to around 100 nm thickness, respectively.

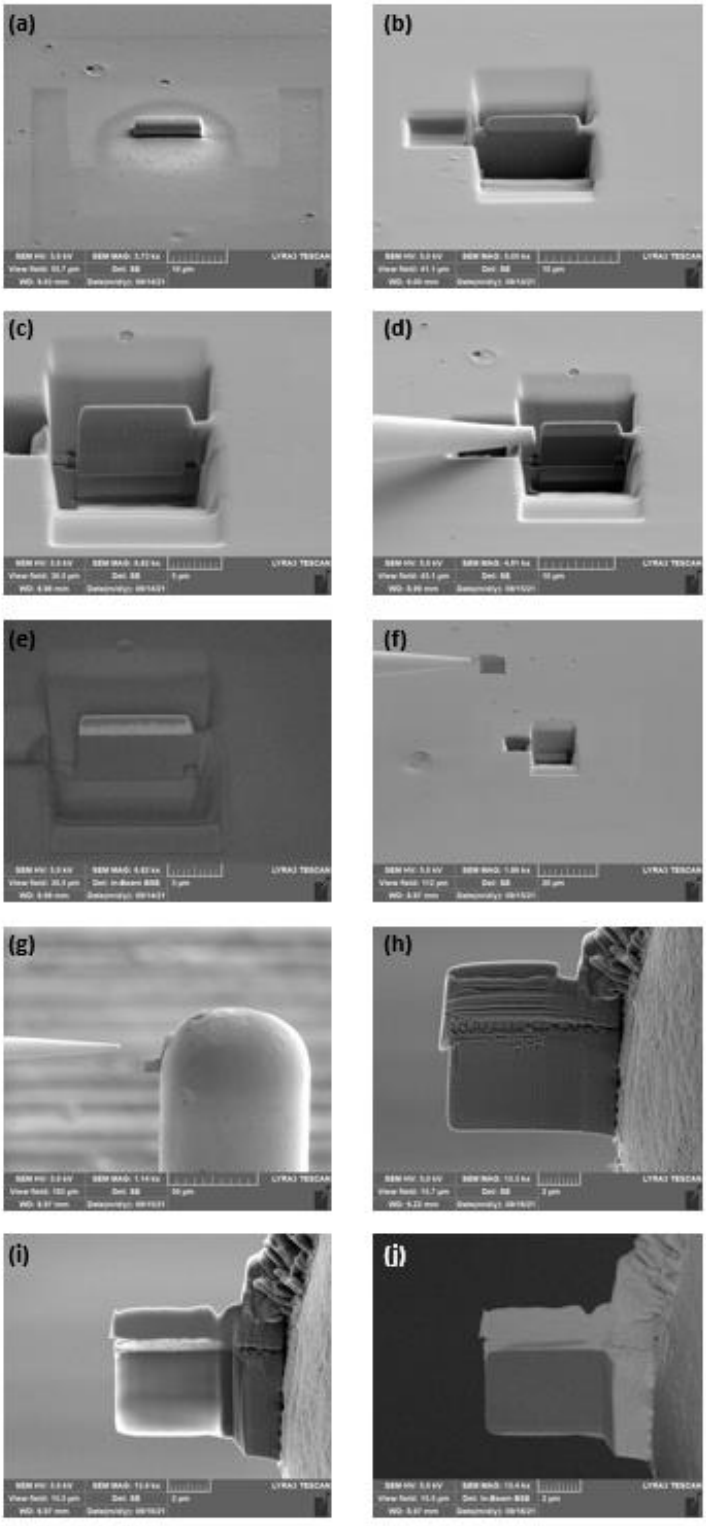

Figure 2.14 TEM lamella lift-out process.

2.3.2 Transmission Electron Microscopy (TEM)

Transmission Electron Microscopy (TEM) is an essential tool for the void swelling study. Figure 2.15 is a photo of the FEI Tecnai F20 TEM in Texas A&M University.

Figure 2.15 The photo of FEI Tecnai F20 TEM in MIC.

Two kinds of electron sources are widely used in TEM, thermionic source. Electrons can be emitted by heating, and electrons can also be produced by applying a high electric potential between the source and anode. This kind of electrons source is called field emission source. Figure 2.16 shows the schematic diagram of TEM [20], the field emission

source is used in the FEI Tecnai F20 TEM instrument. The emitted electrons from FEG (field emission gun) will be accelerated toward the sample. The electron beam is focused on the first condenser lens and the second mini condenser lens has the ability to converge the focused beam to a suitable angle for the expected observation mode. The beam collection angle is restricted by the condenser aperture [21]. Then, the electron beam passes through the specimen, the objective lens is used to focus the image, and objective aperture is used to select which kind of images want to get, like bright-field images or dark-field images, and also can control the contrast of the image [21], the bright-field images are used in the void swelling study. Selected area aperture is used for diffraction pattern mode. Images are projected on the screen and can be observed by using the charge-coupled device (CCD) camera. The intermediate lens and projective lens can change the magnification of the image [21].

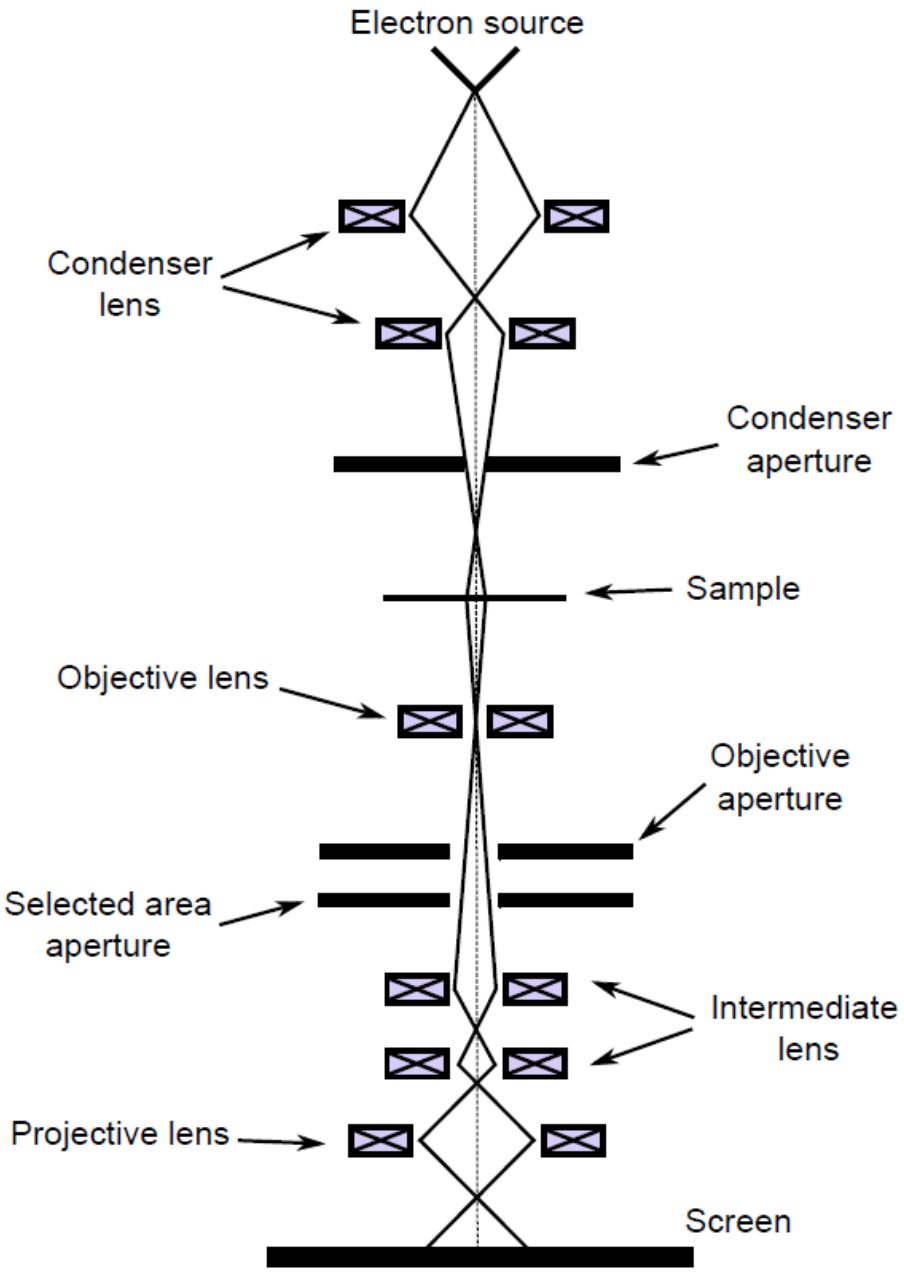

Figure 2.16 Schematic diagram of TEM [20].

Figure 2.17 shows two typical bright-field images of (a) 3.5 MeV Fe^{2+} irradiation to single crystal pure Fe, (b) 5MeV Fe^{2+} irradiation to single crystal pure Fe. The voids are observed in the images, the distribution of voids of 5 MeV irradiation is deeper than the distribution of 3.5 MeV irradiation and the voids size of 5 MeV is larger than 3.5 MeV which correspond to the expectation. The dark area on the top surface is the Pt layer, which is used to protect the specimen surface from FIB damage.

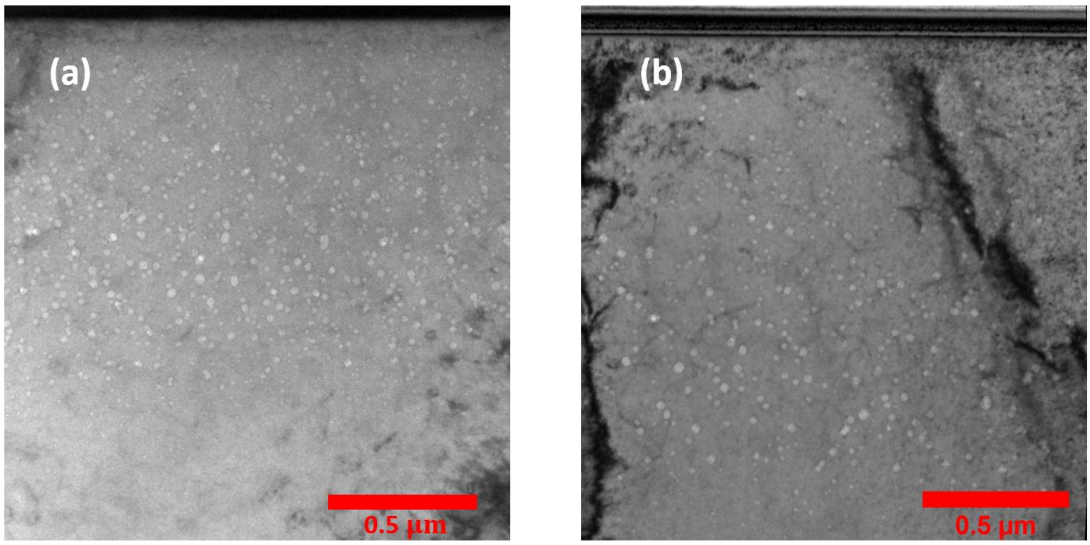

Figure 2.17 Typical bright-field images of (a) 3.5 MeV Fe2+ irradiation to single crystal pure Fe, (b) 5MeV Fe2+ irradiation to single crystal pure Fe.

Reference

[1] https://www.accumetmaterials.com/files/125592020.pdf

[2] Cahn, R. and Haasen, P., 1996. Physical metallurgy. 4th ed. Amsterdam: North-Holland, pp.821-824.

[5] https://www.pelletron.com/products/snics/

[6] https://www.pelletron.com/products/tandem-vs-single-ended/

[7] Gigax, Jonathan G., Eda Aydogan, Tianyi Chen, Di Chen, Lin Shao, Y. Wu, W. Y. Lo, Y. Yang, and F. A. Garner. "The influence of ion beam rastering on the swelling of self-ion irradiated pure iron at 450C." Journal of Nuclear Materials 465 (2015): 343-348.

[8] Gigax, Jonathan G., Hyosim Kim, Eda Aydogan, Frank A. Garner, Stu Maloy, and Lin Shao. "Beam-contamination-induced compositional alteration and its neutron-atypical consequences in ion simulation of neutron-induced void swelling." Materials Research Letters 5, no. 7 (2017): 478-485.

[9] Ziegler, James F., Matthias D. Ziegler, and Jochen P. Biersack. "SRIM–The stopping and range of ions in matter (2010)." Nuclear Instruments and Methods in Physics Research Section B: Beam Interactions with Materials and Atoms 268, no. 11-12 (2010): 1818-1823.

[10] Stoller, Roger E., Mychailo B. Toloczko, Gary S. Was, Alicia G. Certain, Shyam Dwaraknath, and Frank A. Garner. "On the use of SRIM for computing radiation damage exposure." Nuclear instruments and methods in physics research section B: beam interactions with materials and atoms 310 (2013): 75-80.

[11] Garner, F. A., M. B. Toloczko, and B. H. Sencer. "Comparison of swelling and irradiation creep behavior of fcc-austenitic and bcc-ferritic/martensitic alloys at high neutron exposure." Journal of Nuclear Materials 276, no. 1-3 (2000): 123-142.

[12] Gigax, J. G., Tianyi Chen, Hyosim Kim, Jing Wang, L. M. Price, Eda Aydogan, Stuart Andrew Maloy et al. "Radiation response of alloy T91 at damage levels up to 1000 peak dpa." Journal of Nuclear Materials 482 (2016): 257-265.

[13] Gigax, Jonathan G., Hyosim Kim, Tianyi Chen, F. A. Garner, and Lin Shao. "Radiation instability of equal channel angular extruded T91 at ultra-high damage levels." Acta Materialia 132 (2017): 395-404.

[14] Smidt, F. A., P. R. Malmberg, J. A. Sprague, and J. E. Westmoreland. "Swelling behavior of commercial ferritic alloys, EM-12 and HT-9, as assessed by heavy ion bombardment." In Irradiation Effects on the Microstructure and Properties of Metals. ASTM International, 1976.

[15] Melngailis, John. "Focused ion beam technology and applications." Journal of Vacuum Science & Technology B: Microelectronics Processing and Phenomena 5, no. 2 (1987): 469-495.

[16] Giannuzzi, Lucille A., and Frederick A. Stevie. "A review of focused ion beam milling techniques for TEM specimen preparation." Micron 30, no. 3 (1999): 197-204.

[17] Volkert, Cynthia A., and Andrew M. Minor. "Focused ion beam microscopy and micromachining." MRS bulletin 32, no. 5 (2007): 389-399.

[18] Wells, Oliver C., Richard J. Savoy, and Phillip J. Bailey. "Backscattered electron (BSE) imaging in the scanning electron microscope (SEM)-measurement of surface layer mass-thickness." Scanning Electron Microscopy 1982, no. 1 (1982): 25.

[19] Robinson, V. N. E. "Imaging with backscattered electrons in a scanning electron microscope." Scanning 3, no. 1 (1980): 15-26.

[20] Marturi, Naresh. "Vision and visual servoing for nanomanipulation and nanocharacterization in scanning electron microscope." PhD diss., Université de Franche-Comté, 2013.

[21] Williams, David Bernard, and C. Barry Carter. Transmission Electron Microscopy: Spectrometry David B. Williams and C. Barry Cart. IV. Plenum, 1996.

CHAPTER 3

FREE SURFACE EFFECT

3.1 Introduction

High radiation tolerance is required for the development of advanced generation IV reactors. As discussed in Chapter 1, accelerator-based ion irradiation has been widely used as the surrogation to reactor neutron irradiation. However, due to the consideration for the credibility of ion irradiation, the surface effect, in which the free surface can act as sinks to remove point defects during irradiation, must be taken into account.

Void denuded zones have been widely observed in both ion-irradiated and reactor irradiated metals [1-5]. An exponential reduction of point defects is performed towards the free surface. The analytical solutions of defect distribution can be obtained using rate theory to assume that surface is the perfect defect sink [6]. Based on the theory proposed by Konobeev et al., the vacancy depletion depth is approximated proportional to $(D_V/K)^{1/4}$, where D_V is the vacancy diffusivity and K is the dose rate [7].

Usually, the diffusion equation can be written as [6]:

$$\frac{\partial_v}{\partial_t} = K + D_v \frac{\partial^2 v}{\partial x^2} - K_{iv} iv - K_{sv} s_v v \tag{3-1}$$

$$\frac{\partial_i}{\partial_t} = K + D_i \frac{\partial^2 i}{\partial x^2} - K_{iv} iv - K_{si} s_i i \tag{3-2}$$

In these equations, v is the atom fraction of vacancies, i denotes the atom fraction of interstitials, x is the distribution depth away from the surface, K is the production rate of Frenkel pairs, which is the same as dpa (displacement per atom) rate. The diffusion

coefficient of vacancies and interstitials are expressed as D_v and D_i, respectively, which are assumed to be constant. K_{iv} is the recombination rate between vacancies and interstitials, K_{sv} and K_{si} are the annihilation rate of vacancies and interstitials to sinks with the fraction of s_v and s_i of the lattice sites. Sinks in these equations are considered to be perfect sinks, which will not be depleted [6].

The recombination rate between vacancies and interstitials is [6]

$$K_{iv} = 4\pi r_{iv}(D_i + D_v)/\Omega \tag{3-3}$$

Generally, $D_i \gg D_v$, then,

$$K_{iv} \cong 4\pi r_{iv} D_i/\Omega \tag{3-4a}$$

Also,

$$K_{sv} = 4\pi r_{sv} D_v/\Omega \tag{3-4b}$$

and

$$K_{si} = 4\pi r_{si} D_i/\Omega \tag{3-4c}$$

Here, r_{iv} is the critical radius of the recombination volume between vacancy and interstitial, which is slightly temperature dependent only. r_{sv} and r_{si} are the critical annihilation radius of vacancy and interstitial to sinks [6].

To simplify the equations, let

$$D_v v = V \tag{3-5a}$$

and

$$D_i i = I \tag{3-5b}$$

Substituting them to equations (3-1) and (3-2) if assuming a steady-state, which means

$$\frac{\partial_v}{\partial_t} = \frac{\partial_i}{\partial_t}=0 \tag{3-5c}$$

then, equations (3-1) and (3-2) can be rewritten as

$$\frac{d^2V}{dx^2} + K = \frac{K_{iv}}{D_i D_v} IV + \frac{K_{sv}}{D_v} s_v V \tag{3-6a}$$

and

$$\frac{d^2I}{dx^2} + K = \frac{K_{iv}}{D_i D_v} IV + \frac{K_{si}}{D_i} s_i I \tag{3-6b}$$

Single crystal pure Fe samples were used in this study. Thus, only the surface will act as sinks to absorb point defects, and grain boundaries not exist inside the samples [6]. Then, it can be assumed that $s_v = s_i$.

Thus, based on equations (3-4b) and (3-4c),

$$\frac{K_{sv}}{D_v} s_v = \frac{K_{si}}{D_i} s_i \tag{3-7}$$

then

$$I = V \tag{3-8}$$

If neglect the diffusion to surface, i.e., when $\frac{d^2V}{dx^2} = 0$, the solution can be obtained from equations (3-6a) and (3-6b) as V_0 [6],

$$V_0 = (\frac{K}{f_0^{1/2}})[(1+Q)^{1/2} - Q^{1/2}] = K[f_0(1+2S)]^{-1/2} \tag{3-9}$$

here,

$$Q = \frac{s_i^2 K_{si}^2 D_v}{4KK_{iv}D_i} = \frac{s_i^2 K_{si}^2}{4D_i^2 f_0} = \frac{s_v^2 K_{sv}^2}{4D_v^2 f_0} \quad (3\text{-}10)$$

and f_0 is a production rate related to the defect diffusion and recombination

$$f_0 = KK_{iv}/D_i D_v \quad (3\text{-}11)$$

f_s is introduced to simplify the calculation

$$f_s = (K_{iv}V_0/D_i D_v)^2 = f_0/(1+2s) \quad (3\text{-}12)$$

Where, S can be defined as the generalized dimensionless sink concentration, which is proportional to the ratio of defects annihilation rate by sinks and defects recombination rate [6] .

$$S = Q + Q^{\frac{1}{2}}(1+Q)^{\frac{1}{2}} = s_i K_{si} D_v/2K_{iv}V_0$$
$$= s_i K_{si}/2D_i f_s^{1/2} = s_v K_{sv}/2D_v f_s^{1/2} \quad (3\text{-}13)$$

It is obvious that S should be equal to 0 if all defects are removed by recombination, and no sinks are present. Back to equation (3-10), if $Q \gg 1$, which means sinks performed an outstanding role to remove point defects than recombination. S will be a very large value, and

$$V_0 = KD_i/s_i K_{si} = KD_v/s_v K_{sv} = K/2Sf_s^{1/2} \quad (3\text{-}14)$$

If $Q \ll 1$, the recombination will be dominant to remove defects, then

$$V_0 = (KD_iD_v/K_{iv})^{1/2} = K/f_0^{1/2} \tag{3-15}$$

For convenience, the solution in equation (3-9) is normalized to a dimensionless defect concentration as

$$Y = \frac{V}{V_0} \tag{3-16}$$

Substitute them into equations (3-6a) and (3-6b), then

$$\frac{d^2Y}{dx^2} = f_s^{1/2}[(Y+S)^2 - (1+S)^2] \tag{3-17}$$

The free surface can act as sinks to remove defects, the boundary condition can be given as

$$Y = 0, \text{ at } x = 0 \tag{3-18}$$

The solution is

$$Y = 1 - 12A(S+1)[A\,e^X + e^{-X}]^{-2} \tag{3-19}$$

here

$$A = 5 + 6S + [(5+6S)^2 - 1]^{1/2} = [(3S+3)^{1/2} + (3S+2)^{1/2}]^2 \tag{3-20}$$

X is the dimensionless distance

$$X = x[f_s^{1/2}(1+S)/2]^{1/2} = x[f_0^{1/2}(1+S)/2(1+2S)^{1/2}]^{1/2} \qquad (3\text{-}21)$$

The solution of normalized defect concentration Y is only related to the value of S for any materials. Figure 3.1 shows the distribution of steady-state defect concentration with different values of S from 0 to infinite [6].

The solution of Y in equation (3-19) can be approximated as

$$Y \cong 1 - e^{-\beta X} \qquad (3\text{-}22)$$

In this equation

$$\beta = [4(2+3S)/3(S+1)]^{1/2} \qquad (3\text{-}23)$$

From figure 3.1, the solutions of defect concentration Y do not significantly differ with the value of sink concentration from zero to infinite [6]. In this study, single crystal pure Fe was used to avoid the effect of grain boundaries. Due to the less sensitivity to sinks, the value of S can be simplified to 0, then

$$\beta \approx 1.63, \text{ and } \quad X = x[f_0^{\frac{1}{2}}/2]^{1/2} \qquad (3\text{-}24)$$

If we assume a cutoff of Y, for example $\frac{1}{2}$, the void can only nucleate at the depth where the value of Y is larger than $\frac{1}{2}$, then the vacancy depletion depth

$$x = (\frac{\sqrt{2}ln2}{\beta})(f_0^{-\frac{1}{4}}) \qquad (3\text{-}25)$$

Based on equations (3-4) and (3-11),

$$f_0 \propto (\frac{K}{D_v}) \qquad (3\text{-}26)$$

Thus,

$$x \propto (D_v/K)^{1/4} \tag{3-27}$$

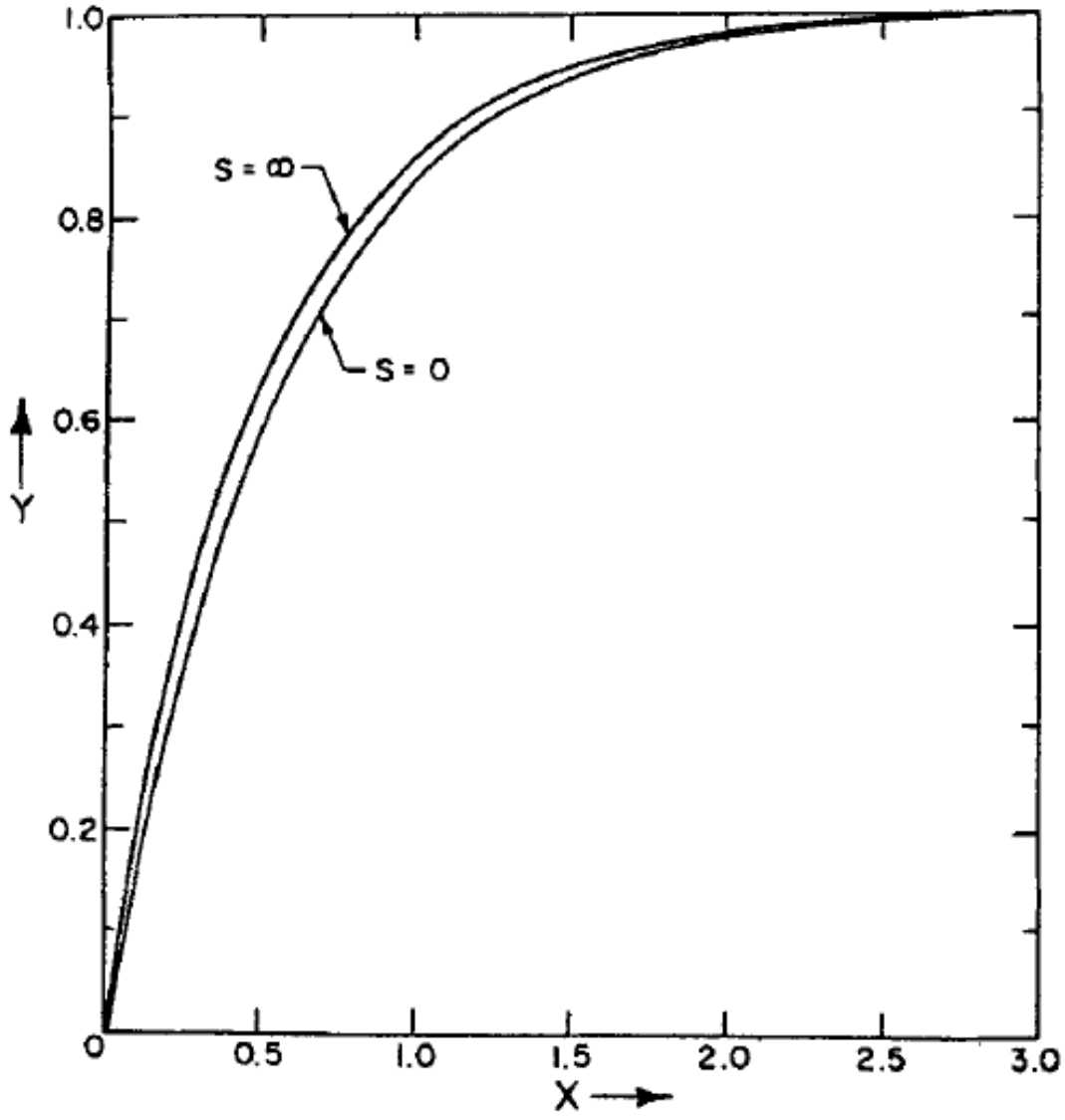

Figure 3.1 The profiles of steady-state defect concentration with S=0 and S=∞, all the solutions with 0<S<∞ are between these two lines [6].

The vacancy depletion depth can be considered void denuded zone width if assuming voids can only be nucleated when the vacancy supersaturation level exceeds a critical value. Y. Sekio1 et al. have observed that the void denuded zone width is a K dependent value under different neutron fluxes [8].

The void denuded zone must be excluded for void swelling testing to avoid the influence of surface effect during irradiation. Such regions can be identified easily by using TEM. Nevertheless, the region deeper than the void denuded zone may also be influenced by the surface if the vacancy supersaturation is high enough to overcome the surface sink effect to nucleate voids. It is not a negligible question because the surface effect may influence the majority testing region of the low energy irradiation, such as 1 MeV Ni self-ion irradiation, which was widely used in early studies.

This chapter introduces a method to quantitatively define the surface affected region by void swelling studies in self-ion irradiation to single crystal pure Fe.

3.2 Experimental Procedure

<111> oriented single crystal pure Fe with the purity of 99.94+% (ordered from Accument Materials Inc., Ossining, NY, USA) were used in the study. The specimens were cut into 3mm×3mm×1mm small pieces using the Extec Labcut 150 cutter and then mechanically polished using ACE Nano 2000T Grinder-polisher on SiC papers from 400 grit down to 4000 grit with the rotate speed of 200 rpm. In addition, TenuPol-5

electropolisher was used for electropolishing to improve the quality of specimen surface further. The detailed process has been introduced in Chapter 1, section 1.

Single crystal pure Fe specimens were irradiated by Fe^{2+} ions with the energy of 1 MeV, 2.5 MeV, 3.5 MeV, and 5 MeV, respectively. The irradiation temperature, 475℃, is selected as the maximum swelling temperature of Fe [9-12]. A static defocused uniform beam with the size around 5 mm ×5 mm was produced to avoid the pulse beam effect due to rastering [13]. The beam was deflected three times using magnet deflectors to filter out carbon contamination, as introduced in Chapter 2 [14]. During irradiation, the target chamber was maintained at a high vacuum level, better than 6×10-8 torr, using the turbopump with a roughing pump. A liquid nitrogen cold trap located in the target chamber was used to improve the vacuum.

Table 3.1 shows the irradiation fluences of different energies and doses, calculated by using SRIM with the displacement energy of 40 eV, as discussed in Chapter 2.

Table 3.1 The irradiation fluences ($\frac{ions}{cm^2}$) of different energies and doses.

	1 MeV	2.5 MeV	3.5 MeV	5 MeV
50 peak dpa	3.9×10^{16}	4.64×10^{16}	4.93×10^{16}	5.04×10^{16}
100 peak dpa	7.8×10^{16}	9.28×10^{16}	9.86×10^{16}	1.08×10^{17}

After irradiation, focused ion beam (FIB) was used to prepare the TEM lamella by using 30 keV Ga^+ ions until the thickness was around 200 nm. Then, the 5 keV Ga^+ beam was used for the final thinning to make lamella thickness less than 100 nm. Finally, bright-field TEM characterization was taken under 200 keV e^- beam by using FEI Tecnai F20. The thickness of lamella at different depths was measured by using the electron energy loss spectroscopy (EELS) technique. ImageJ, an open-source image analysis tool [15-16], was used for void analysis like size and position.

3.3 Results

3.3.1 Void Denuded Zone

3.3.1.1 Energy Dependent

Figure 3.2 shows the bright field cross-sectional TEM micrographs of single crystal pure Fe irradiated at 475 ℃ with the energy and dose of (a-1) 1 MeV at 50 peak dpa, (a-2) 2.5 MeV at 50 peak dpa, (a-3) 3.5 MeV at 50 peak dpa, (a-4) 5 MeV at 50 peak dpa, (b-1) 1 MeV at 50 peak dpa, (b-2) 2.5 MeV at 100 peak dpa, (b-3) 3.5 MeV at 100 peak dpa, and (b-4) 5 MeV at 100 peak dpa, respectively. All the irradiation were performed with the same dpa rate 1.2×10^{-3} dpa/s, the fluctuation is less than 0.1×10^{-3} dpa/s. The red lines are the corresponding dpa curves of 1 MeV, 2.5 MeV, 3.5 MeV and 5 MeV Fe^{2+} irradiation to pure Fe calculated by using SRIM based on the Kinchin-Pease (KP) mode with the displacement energy of 40 eV.

Voids appear in all images from 1 MeV to 5 MeV, and voids distribute deeper with the increase of irradiation energy. The void denuded zone can be observed in all micrographs. Figure 3.3 shows the magnified TEM micrographs of single crystal Fe irradiated by Fe ions with different energies and doses in the near-surface region. The widths of the void denuded zone were measured by using ImageJ.

The widths of void denuded zones increase with the increase of ion energies for the same dose. For 50 peak dpa, the denuded zone width for 1 MeV is 71 nm (shown in figure 3.3 (a-1)), for 2.5 MeV is 80 nm (figure 3.3 (b-1)), for 3.5 MeV (figure 3.3 (c-1)) and 5 MeV (figure 3.3 (d-1)) are 98 nm and 109 nm, respectively. It also found that the widths of void denuded zones decrease with the dose increase at the same irradiation energy. The width decreases from 71 nm (50 peak dpa) to 61 nm (100 peak dpa, as shown in figure 3.3 (a-2)) for 1 MeV irradiation. For 2.5 MeV, the denuded zone width decreases from 80 nm for 50 peak dpa to 73 nm for 100 peak dpa, as figure 3.3 (b-2) shown. Figure 3.3 (c-1) and (c-2) show that the width decreases from 98 nm for 50 peak dpa to 82 nm for 100 peak dpa. Also, the width decreases from 109 nm for 5 MeV 50 peak dpa to 90 nm for 5 MeV 100 peak dpa (figure 3.3 (d-2)). All the values of void denuded zone widths are shown in table 3.2.

Table 3.2 Widths of observed void denuded zones (nm) for Fe irradiated by different energies and doses at the peak dpa rate of 1.2×10^{-3} dpa/s. The temperature is 475 ℃ for all irradiations.

	1 MeV	2.5 MeV	3.5 MeV	5 MeV
50 peak dpa	71	80	98	109
100 peak dpa	61	73	82	90

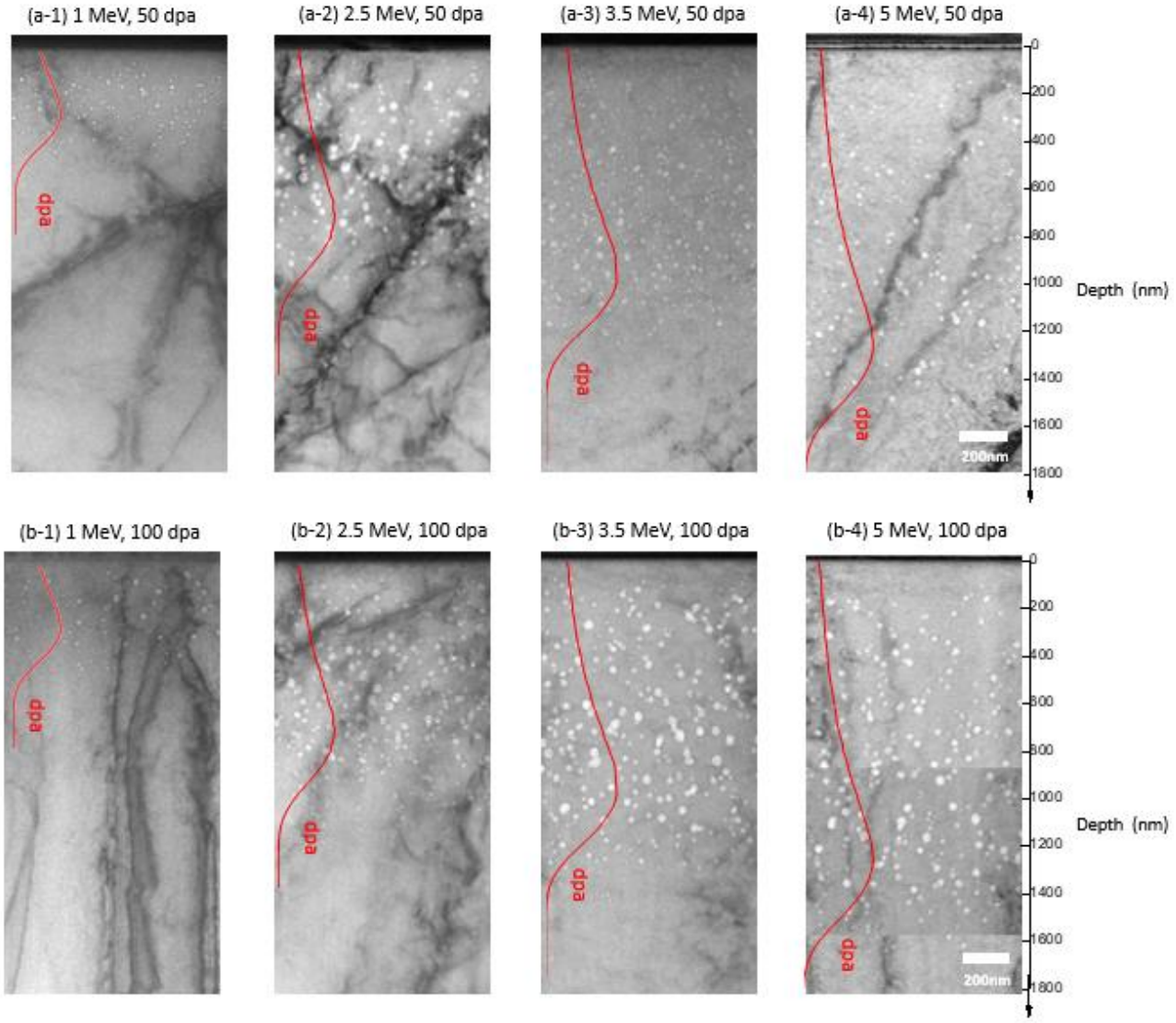

Figure 3. 2 Cross-sectional TEM micrographs of single crystal pure Fe irradiated at 475 ℃ by Fe ions with the energy and dose of (a-1) 1 MeV at 50 peak dpa, (a-2) 2.5 MeV at 50 peak dpa, (a-3) 3.5 MeV at 50 peak dpa, (a-4) 5 MeV at 50 peak dpa, (b-1) 1 MeV at 50 peak dpa, (b-2) 2.5 MeV at 100 peak dpa, (b-3) 3.5 MeV at 100 peak dpa, and (b-4) 5 MeV at 100 peak dpa.

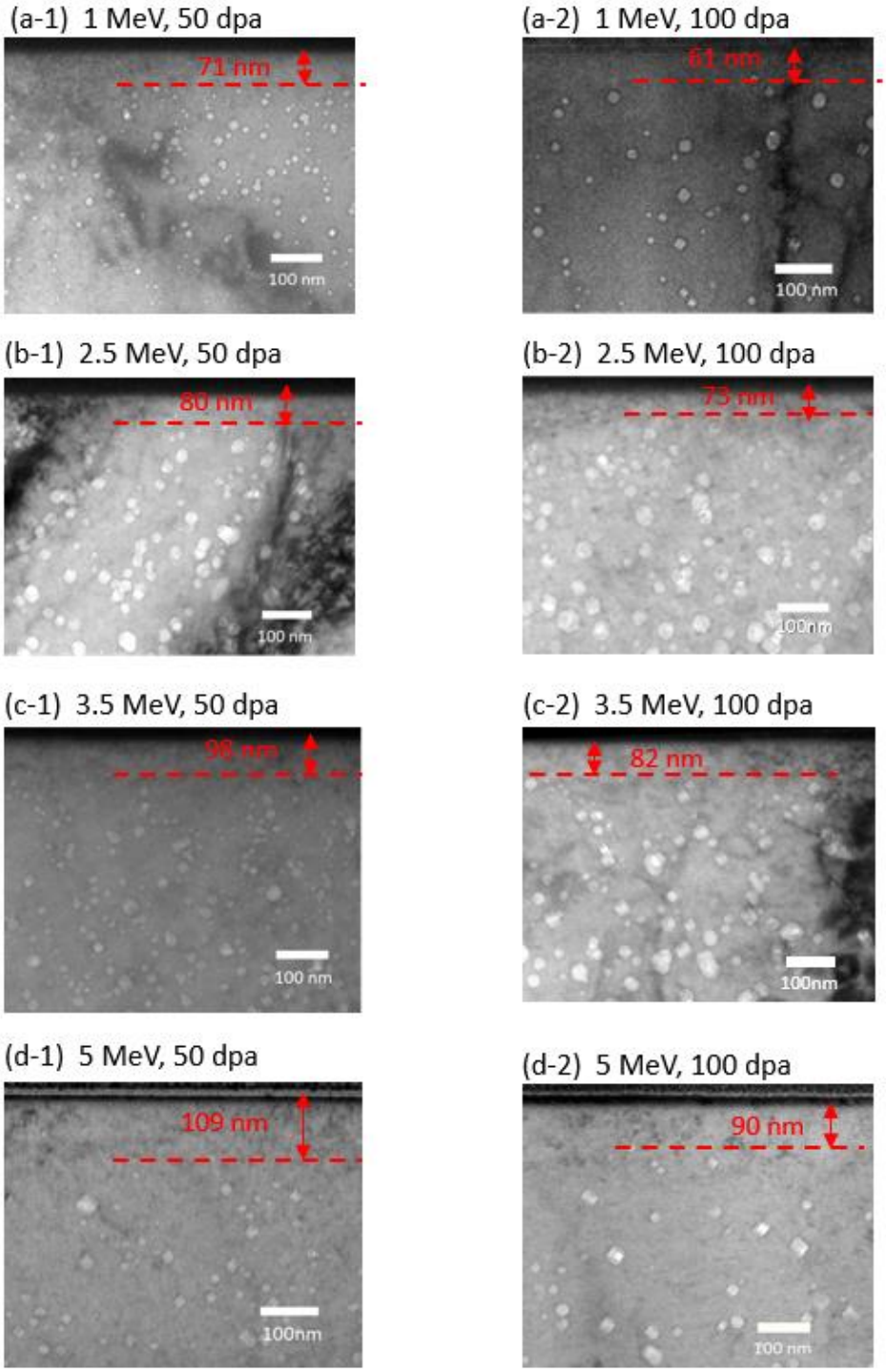

Figure 3. 3 Cross-sectional TEM micrographs of single crystal Fe irradiated by Fe ions at 475 ℃ with different irradiation energies in the near-surface region.

It is notable that only a tiny part of the TEM micrographs are selected to be shown here due to the limited space in the paper. For example, only the parts of TEM micrographs which have the void closest to the surface for different energies and doses are selected to be displaced in figure 3.3 to show the void denuded zone. The statistics are obtained from the whole region of TEM micrographs, generally the width is no less than 4 μm. Thus, the amount of voids used for analysis at each depth is much more than the number shown in the images. Figure 3.4 shows the statistics of the void size distribution at each 200 nm depth start from surface until to the region no voids can be observed at all for 1 MeV, 2.5 MeV, 3.5 MeV, and 5 MeV irradiations with the dose of 50 peak dpa and 100 peak dpa, separately. As figure 3.4 shown, the statistics are sufficient to show gaussian-like size distributions at each depth interval. The red line is the Gauss fitting curve for each depth point.

The surface sputtering effect must be taken into account to determine the final width of the void denuded zone. Sputtering of surface atoms by incident energetic ions results from cascades of atomic collisions. For example, as shown in figure 3.5, atom 2 and atom 4 were sputtered out due to the energetic incident ion-induced cascades collisions [17]. The sputtering yields are related to the local nuclear stopping power [17], which is a function of the surface local dpa rate $K_{surface}$. With the increase of incident beam energies, the local stopping power in the near-surface region will decrease due to the shift of the nuclear stopping power peak away from the surface. Then, lower incident energies will lead to higher sputtering yields and have a stronger influence on the definition of the void denuded zone. Calculated by using SRIM with the mode of "monolayer collision steps/surface

sputtering", the sputtering yields for different energies of incident Fe ions to single crystal pure Fe are obtained. The values are shown in table 3.3.

Table 3.3 Sputtering yields and thickness for incident Fe ions to single crystal pure Fe with the energy of 1 MeV, 2.5 MeV, 3.5 MeV, and 5 MeV separately.

Incident Fe ions energy (MeV)	1 MeV	2.5 MeV	3.5 MeV	5 MeV
Sputtering atoms per bombarding ion	2.11	1.35	1.16	0.95
Sputtering thickness (50 peak dpa) (nm)	12.4	8.0	6.8	5.6
Sputtering thickness (100 peak dpa) (nm)	24.8	16.0	13.6	11.2

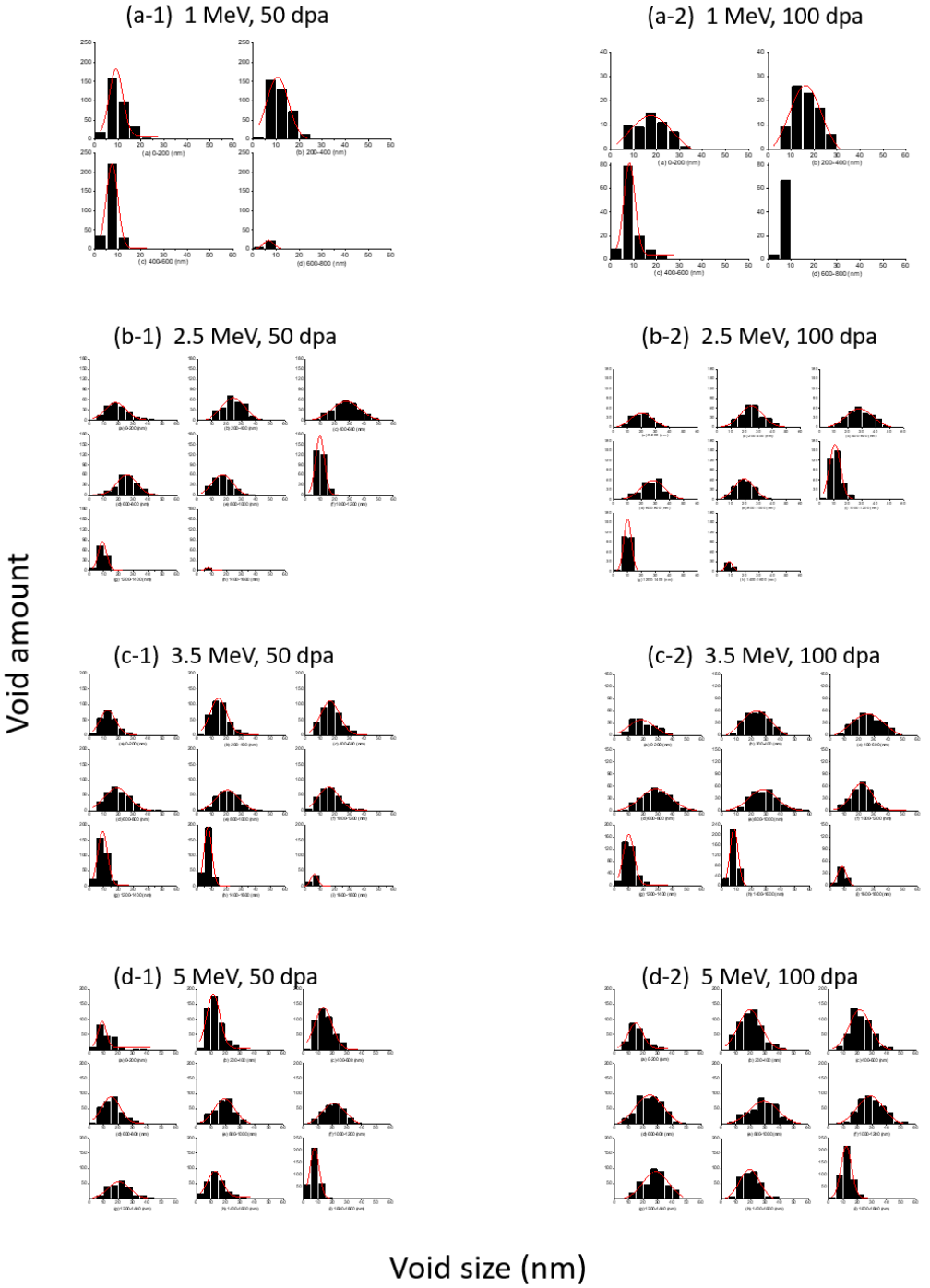

Figure 3. 4 Statistics of the void size distribution at each 200 nm start from surface until to the depth no voids can be observed of single crystal pure Fe irradiated at 475 ℃ by Fe ions with the energy and dose of (a-1) 1 MeV at 50 peak dpa, (a-2) 1 MeV

at 100 peak dpa, (b-1) 2.5 MeV at 50 peak dpa, (b-2) 2.5 MeV at 100 peak dpa, (c-1) 3.5 MeV at 50 peak dpa, (c-2) 3.5 MeV at 100 peak dpa, (d-1) 5 MeV at 50 peak dpa, (d-2) 5 MeV at 100 peak dpa.

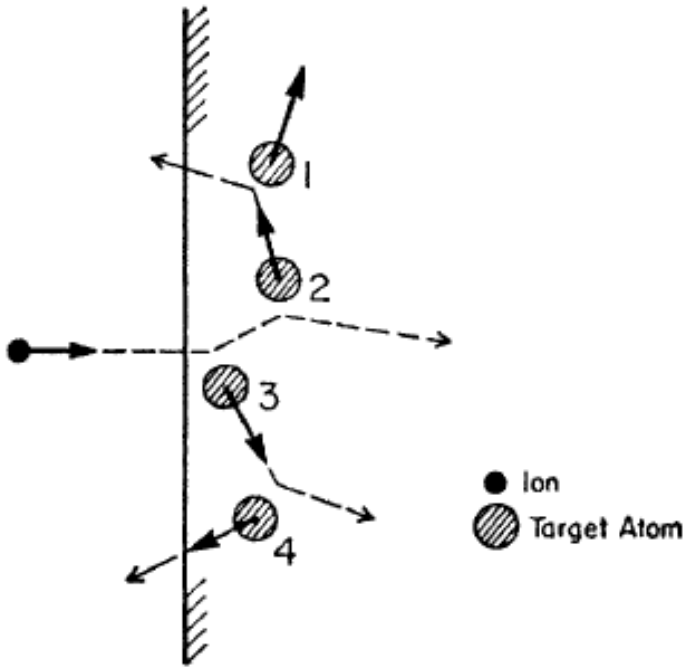

Figure 3. 5 Sputtering atoms 2 and 4 result from cascades collisions [17].

Since the local stopping power is linked to the local dpa rate, it decreases with the increase of incident beam energy. Thus, due to the vacancy depletion width is proportional to $(D_V/K)^{1/4}$ [7], the width will increase with the increase of incident beam energy. Then, the width of void denuded zone can be identified as the summation of sputtering depth and vacancy depletion width. However, the question is how to define an appropriate local dpa rate to estimate the vacancy depletion width. Figure 3.6 (a) shows the local dpa rate of the single crystal Fe irradiated by 5 MeV Fe ions at 475℃ with the peak dpa rate of 1.2×10^{-3} dpa/s, the local dpa rate in the near-surface region is almost an order of magnitude smaller than the peak value. For the low energy irradiation, the shallow dpa peak means high nonuniform of local dpa rate along the ion path, as the local dpa rate of 1 MeV irradiation shown in figure 3.6 (b).

In order to evaluate the effect of different dpa rate values, three different depth regions, (1) from surface to 200 nm depth, (2) surface to 400 nm depth, (3) surface to 600 nm depth, were selected to calculate the average local dpa rate $K_{average}$. Figure 3.7 shows the fitting curves of vacancy depletion zone width $(D_V/K)^{1/4}$ with the average dpa rate $K_{average}$ obtained from three different depth regions with the irradiation of 1 MeV, 2.5 MeV, 3.5 MeV, and 5 MeV, respectively. There is no significant difference between the 0 to 200 nm and 0 to 400 nm regions. The raised value of 1 MeV irradiation in the 0 to 600 region because of the shallow distribution of 1 MeV dpa rate, the depth of 1 MeV peak dpa rate is only around 270 nm, as figure 3.6 (b) shown. The value of $(D_V/K)^{1/4}$ is not sensitive to the region of average dpa rate.

Based on the relationship $\Delta x \propto (D_V/K)^{1/4}$, the best fitting for the width of the void denuded zone is given as

$$\Delta x\ (nm) = 17.24\ (\frac{1}{K})^{\ 1/4} \qquad (3\text{-}28)$$

Where K is the average dpa rate obtained from the region of 0 to 200 nm depth for each energy, respectively, Δx is calculated as the summation of corresponding sputtering loss and the width measured from TEM micrographs. The comparison of the fitting curve and experimental data is shown in figure 3.8.

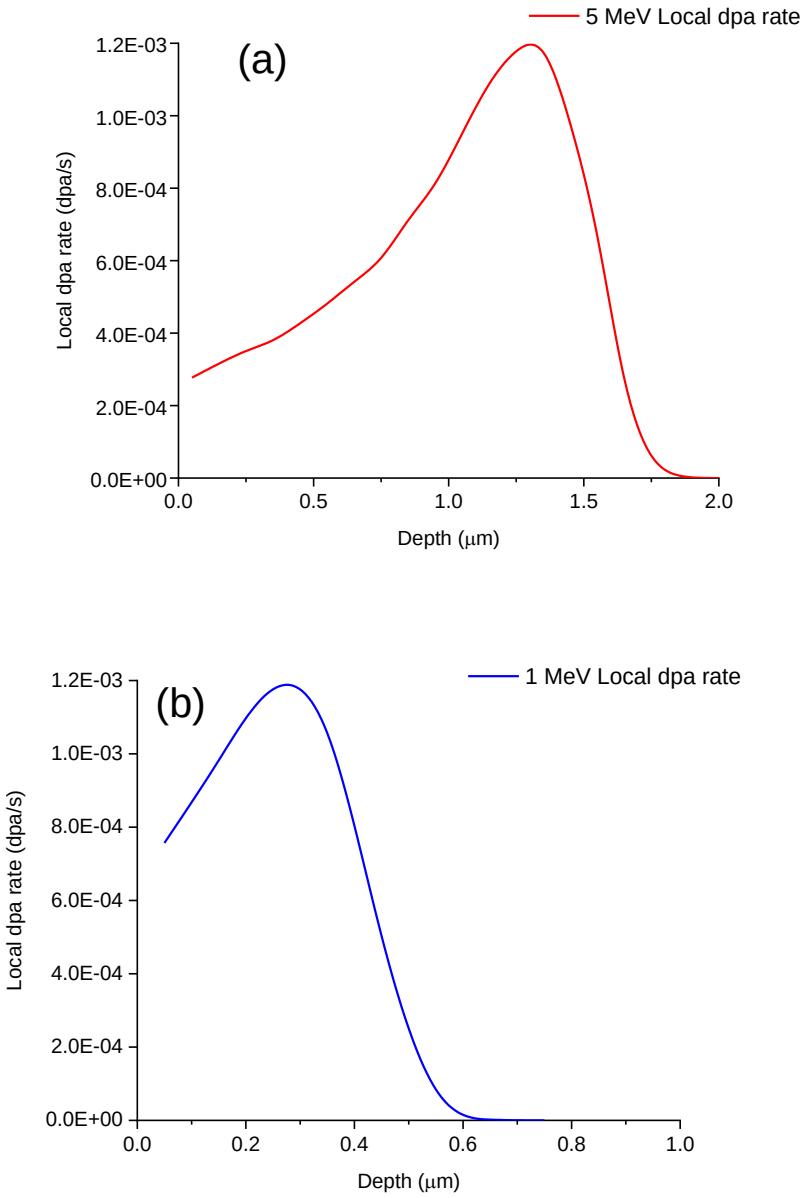

Figure 3. 6 Local dpa rate of the single crystal Fe irradiated by (a) 5 MeV Fe ions and (b) 1 MeV Fe ions at 475℃ with the peak dpa rate of 1.2×10^{-3} dpa/s.

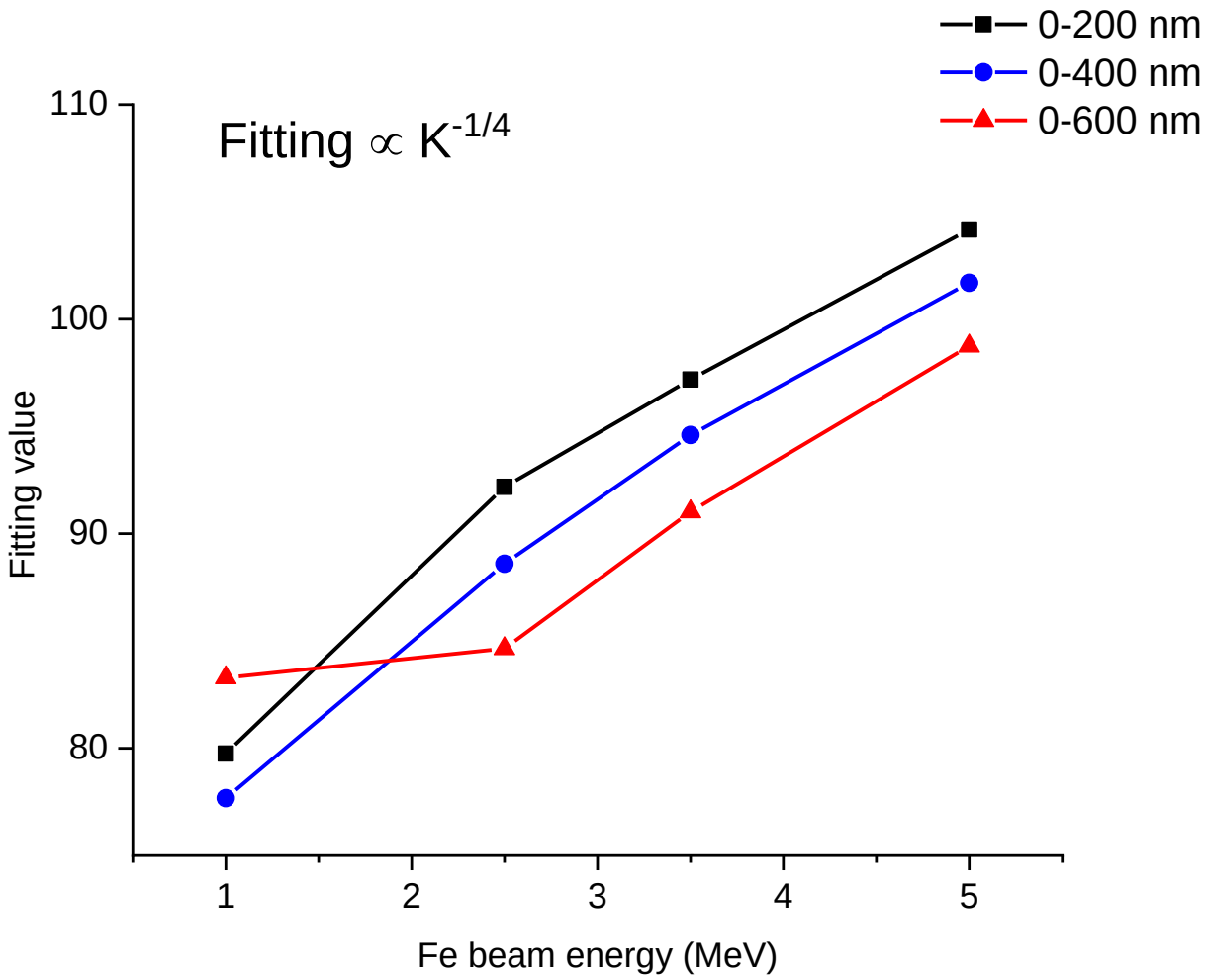

Figure 3. 7 Fitted width of the vacancy depletion zone proportional to $(\frac{1}{K_{average}})^{1/4}$, the average dpa rate $K_{average}$ is obtained from three different depth regions, 0 to 200 nm, 0 to 400 nm, and 0 to 600 nm, with the irradiation energy of 1 MeV, 2.5 MeV, 3.5 MeV, and 5 MeV, respectively.

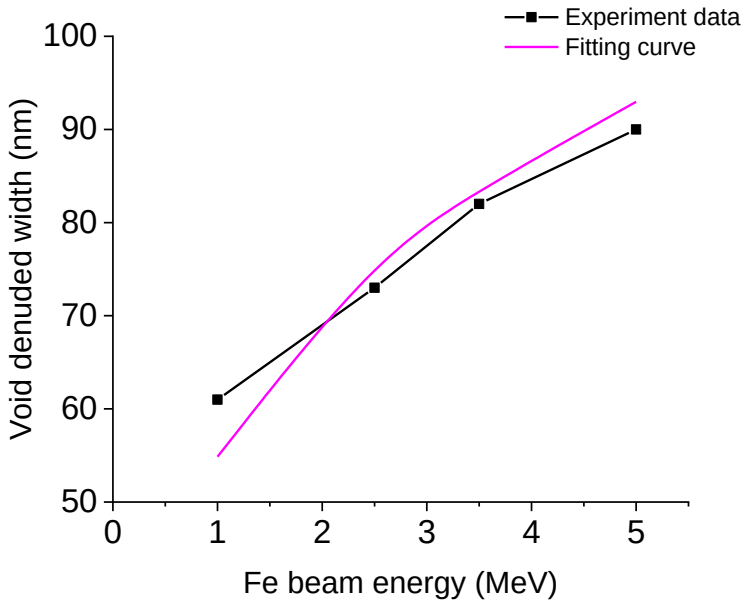

Figure 3. 8 Comparison of the void denuded width from experiment and fitting data with the temperature of 475 C.

3.3.1.2 Dpa Rate Dependent

The above discussed the void denuded zone of single crystal pure Fe irradiated by Fe ions with different energies, and the irradiation temperature is 475 ℃. The dpa rate is fixed as 1.2×10^{-3} dpa/s with the fluctuation of less than 0.1 × 10-3 dpa/s.

To study the width of the void denuded zone at different dpa rates, three more irradiations were performed by 5 MeV Fe^{2+} ions with the peak dpa rate of 6×10^{-3} dpa/s, 3×10^{-4} dpa/s, and 2×10^{-4} dpa/s, respectively. All the samples were irradiated at 475 ℃. which means the vacancy diffusion coefficient D_v keeps the same value.

Figure 3.9 compares the cross-sectional TEM micrographs of Fe irradiated by 5 MeV Fe^{2+} ions at the peak dpa rate of 6.0×10^{-3} dpa/s, 1.2×10^{-3} dpa/s, 3.0×10^{-4} dpa/s, and

2.0×10^{-4} dpa/s, respectively. The width of the void denuded zone is 177 nm for 2.0×10^{-4} peak dpa rate, 151 nm for 3.0×10^{-4} peak dpa rate, 109 nm for 1.2×10^{-3} peak dpa rate, and 59 nm for 6.0×10^{-3} dpa/s. The void denuded zone width increases with decreasing of peak dpa rate. The values of observed void denuded zone width are shown in table 3.4.

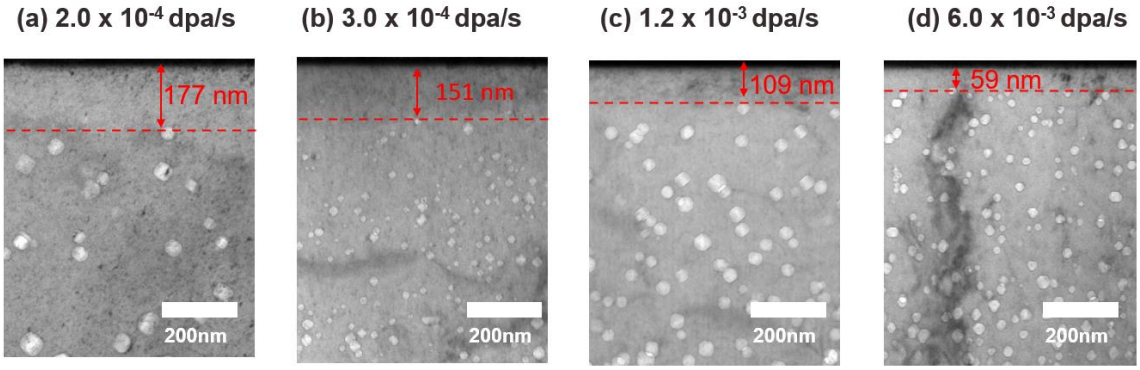

Figure 3. 9 Cross sectional TEM images of Fe irradiated at the peak dpa rate of (a) 2.0×10^{-4}, (b) 3.0×10^{-4} dpa/s, (c) 1.2×10^{-3} dpa/s, and (d) 6.0×10^{-3} dpa/s, respectively. The temperature was 475 °C for all irradiations.

Table 3.4 Widths of observed void denuded zones for Fe irradiated by 5 MeV Fe^{2+} ions at different peak dpa rates. The temperature is 475 ℃ for all irradiations.

Peak dpa rate (dpa/s)	6.0×10^{-3}	1.2×10^{-3}	3.0×10^{-4}	2.0×10^{-4}
Void denuded zone width (nm)	59	109	151	177

Add the sputtering loss calculated by using SRIM, as table 3.3 shown, to the experimentally observed void denuded zone width for all energy dependent irradiations (1 MeV, 2.5 MeV, 3.5 MeV, and 5 MeV) with the same peak dpa rate, 1.2×10^{-3} dpa/s. And add the sputtering loss to the observed width of the void denuded zone for dpa rate dependent irradiations (6.0×10^{-3} dpa/s, 1.2×10^{-3} dpa/s, 3.0×10^{-4} dpa/s, and 2.0×10^{-4} dpa/s) by 5 MeV Fe^{2+} ions. Figure 3.10 plots the relationship between the width of void denuded zone Δx and the dpa rate K. Note that the sputtering loss used the same value for different peak dpa rates because the ion flux is not high enough to have simultaneous arrival of more than one ion at the same spot. All irradiations were performed at the same temperature 475 °C. The linear fitting in figure 3.10 shows good applicability of the relationship $\Delta x \propto (\frac{D_v}{K})^{1/4}$ for a wide range of irradiations.

The best fitting of Fe irradiated by Fe ions at the irradiation temperature of 475 °C gives

$$\Delta x = -20.002 + 17.26(\frac{1}{K})^{\frac{1}{4}} \quad (3\text{-}29)$$

K is the dpa rate (dpa/s), the average local dpa rate from the range of 0 to 200 nm was used in the fitting.

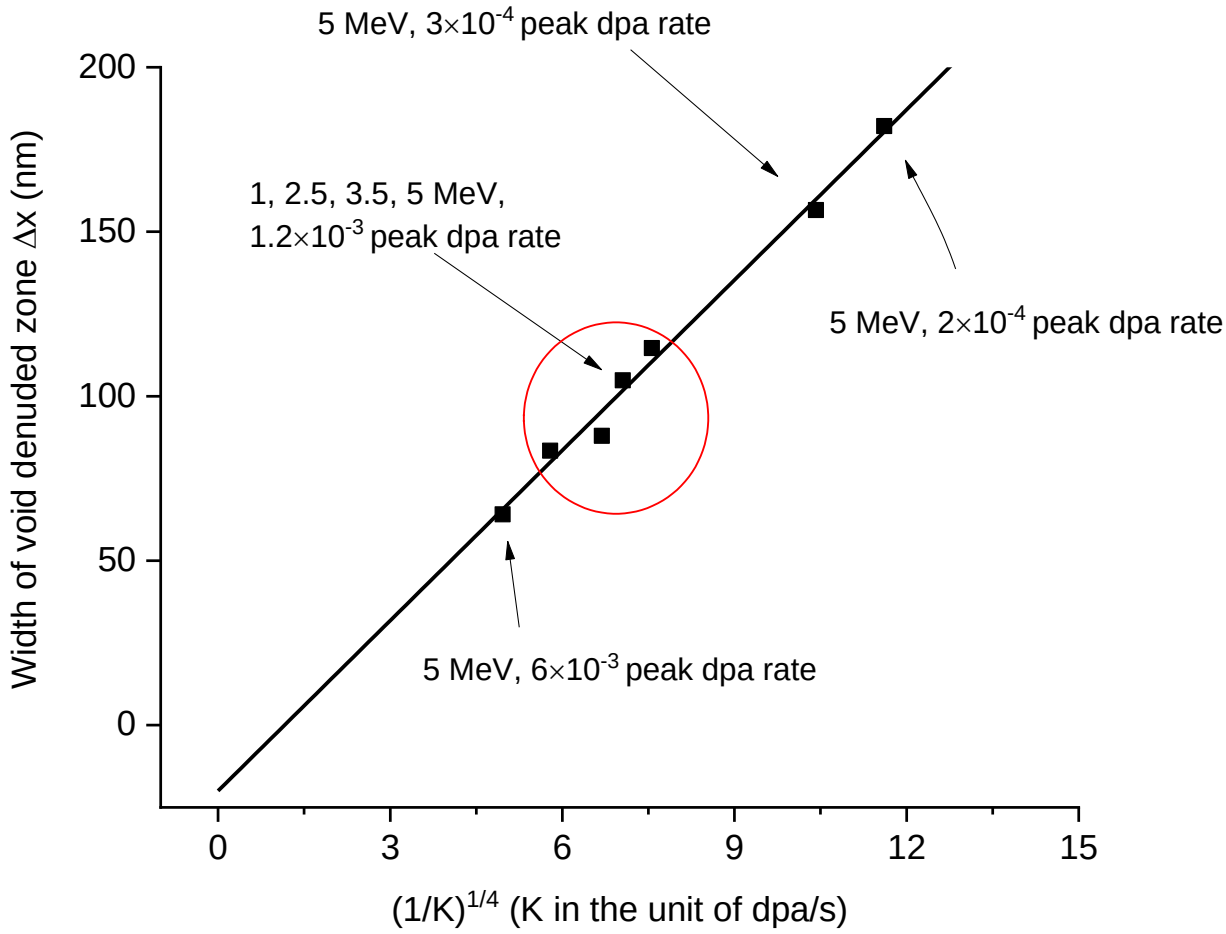

Figure 3. 10 Void denuded zone width Δx for different K values and the fitting curve. The data include these obtained from energy dependent irradiations (1, 2.5, 3.5, and 5 MeV) and dpa rate dependent irradiations (6.0×10^{-3} dpa/s, 1.2×10^{-3} dpa/s, 3.0×10^{-4} dpa/s, and 2.0×10^{-4} dpa/s). All irradiations were at 475 °C.

3.3.1.3 Temperature Dependent.

Section 3.3.1.1 and 3.3.1.2 obtained the good applicability of the relationship between the void denuded width and dpa rate for a wide range of Fe ion irradiations. However, the result was limited to the fixed temperature of 475 °C. Because the value of vacancy diffusivity will change with different irradiation temperatures, as the following equation shown

$$D_v = D_0 e^{\left(\frac{-E_v}{k_B T}\right)} \tag{3-30}$$

D_v is the vacancy diffusion coefficient, D_0 is a constant, E_v denotes the vacancy activation energy (eV), T is the temperature, k_B is the Boltzmann constant,

$$k_B = 8.617 \times 10^{-5}\ (eV \cdot K^{-1}) \tag{3-31}$$

To study the temperature effect for the width of the void denuded zone, three Fe ions irradiation to pure Fe were performed at the temperature of 425 °C, 475 °C, and 525 °C, respectively. The peak dpa rates were kept at 6.0×10^{-3} dpa/s for all of the irradiations. Figure 3.11 shows the cross-sectional TEM micrographs of these three irradiations. The observed void denuded width from TEM images is 36 nm at 425 °C irradiation, 59 nm at 475 °C irradiation, and 92 nm at 525 °C irradiation. The values of width are shown in table 3.5.

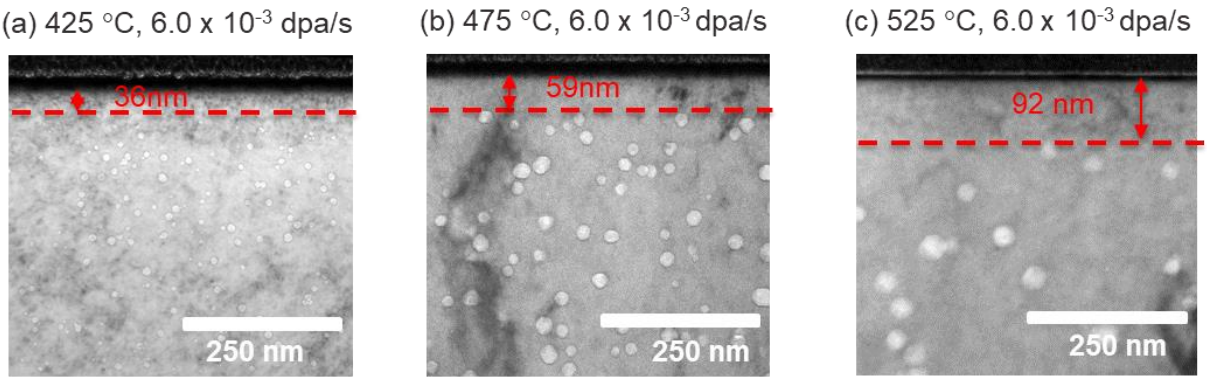

Figure 3. 11 Cross-sectional TEM micrographs of pure Fe irradiated by 5 MeV Fe^{2+} ions at (a) 425 °C, (b) 475 °C, and (c) 525 °C. The peak dpa rates were kept at 6.0×10^{-3} dpa/s for all irradiations.

Table 3.5 Widths of observed void denuded zones for Fe irradiated by 5 MeV Fe^{2+} ions at 425°C, 475°C, and 525°C, respectively. The peak dpa rate is 6.0×10^{-3} dpa/s for all irradiations..

Temperature (°C)	425	475	525
Void denuded zone width (nm)	36	59	92

Based on the equations (3-27)

$$\Delta x \propto (D_V/K)^{1/4} \tag{3-27}$$

and equation (3-30)

$$D_v = D_0 e^{(\frac{-E_v}{k_B T})} \tag{3-30}$$

It can be obtained that

$$\ln(K \cdot \Delta x^4) \propto \frac{-E_v}{k_B T} \tag{3-32}$$

K is the average dpa rate, Δx is the void denuded zone width with the consideration of sputtering loss.

Figure 3.12 shows the relationship between the void denuded zone width and the reciprocal of $k_B T$.

The fitting in figure 3.12 gives the vacancy activation energy

$$E_v = 1.65 \pm 0.03\ eV \tag{3-33}$$

Then, the general expression for the void denuded zone width Δx in Fe can be obtained as

$$\Delta x = -20.002 + 1.037 \times 10^4 \times \left(\frac{\exp(-\frac{1.65}{k_B T})}{K}\right)^{1/4} \tag{3-34}$$

here, k_B is the Boltzmann constant, $k_B = 8.617 \times 10^{-5}\ (eV \cdot K^{-1})$; T is the irradiation temperature, and the unit is kelvin; K is the dpa rate with the unit of dpa/s.

This equation can be used to predict the void denuded zone width for Fe irradiated by Fe ions at different conditions.

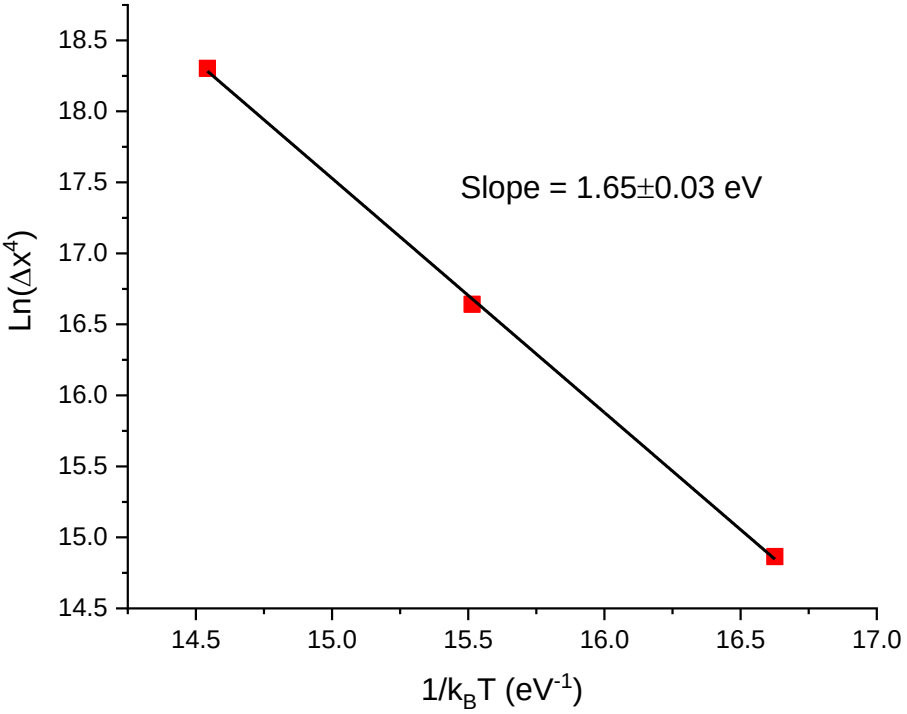

Figure 3. 12 The relationship between the void denuded zone width and the reciprocal of k_BT. The irradiations were performed with 5 MeV Fe ions at 425 °C, 475 °C, and 525 °C, with the same peak dpa rate of 6.0×10^{-3} dpa/s. Δx is the width of the void denuded zone with the consideration of sputtering loss.

3.3.2 Surface Effect Region Beyond Denuded Zone

The last section introduced the quantitative method to define the width of the void denuded zone of Fe irradiated by Fe ions. However, if the vacancy supersaturation is high enough to overcome the surface sink effect to nucleate voids, the free surface can still affect the region beyond the void denuded zone. Furthermore, the surface effect will change the profiles of void swelling. Therefore, this section will introduce the method to define the surface effect region beyond the void denuded zone.

Figure 3.13 plots the void swelling distribution of pure Fe irradiated by Fe^{2+} ions with the energy of 1 MeV, 2.5 MeV, 3.5 MeV, and 5 MeV, respectively. The irradiation doses are 50 peak dpa and 100 peak dpa. The temperature is 475 ℃ for all irradiations. The solid lines are dpa profiles with corresponding irradiation energies, and the dash lines are the Fe ions implantation ranges. The widths of the void swelling regions decrease with the decrease of irradiation energies. The region becomes very narrow for the low energy irradiations. For example, the swelling region width can reach around 2000 nm for 5 MeV irradiation, but only 600 nm width for the 1 MeV irradiation. Thus, due to the surface effect, the region that can be safely used for the void swelling study of low energy irradiation will be very limited, especially if considering the injected interstitial effect introduced in the next chapter. Thus, it is very important to find a method to avoid the surface effect region.

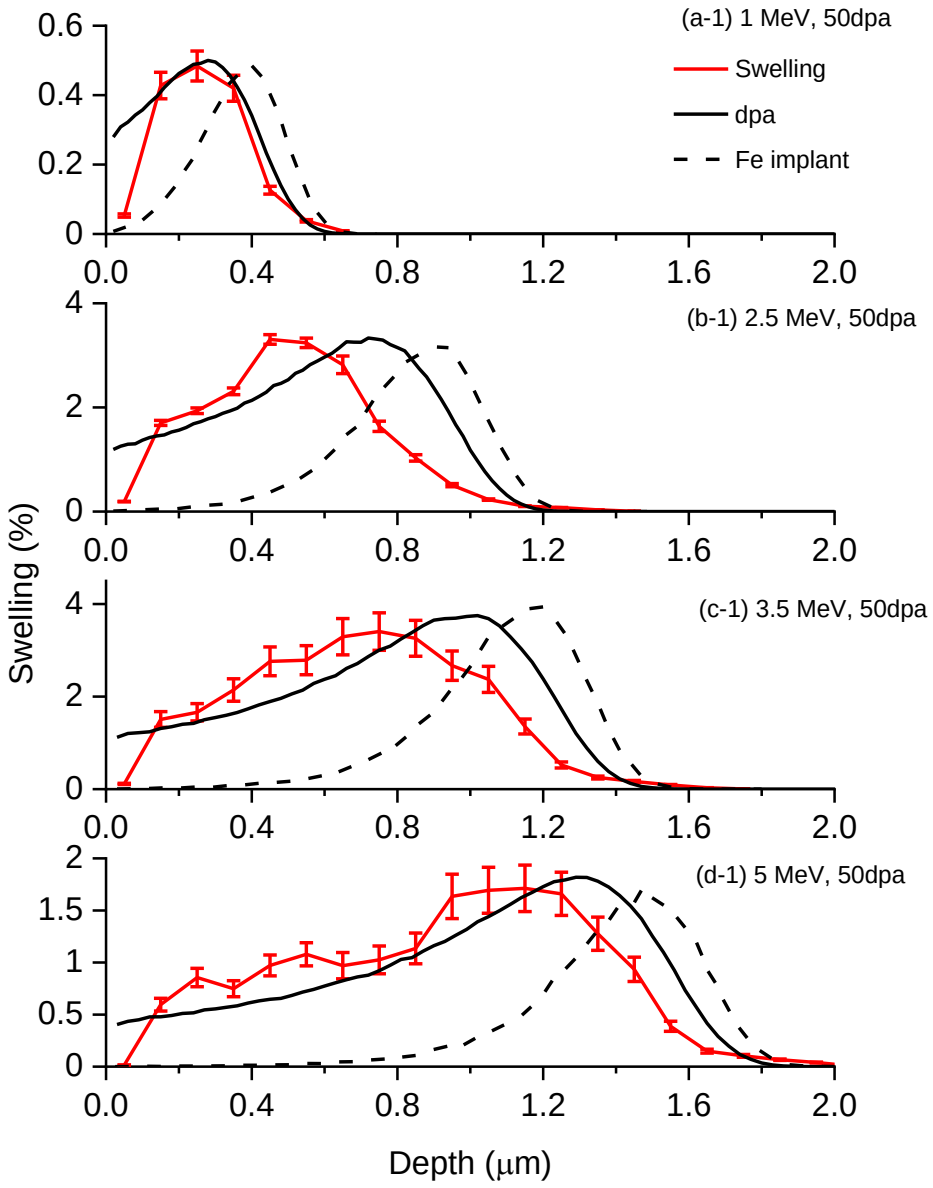
(a-1) 1 MeV, 50dpa
Swelling
dpa
Fe implant
(b-1) 2.5 MeV, 50dpa
(c-1) 3.5 MeV, 50dpa
(d-1) 5 MeV, 50dpa
Swelling (%)
Depth (μm)

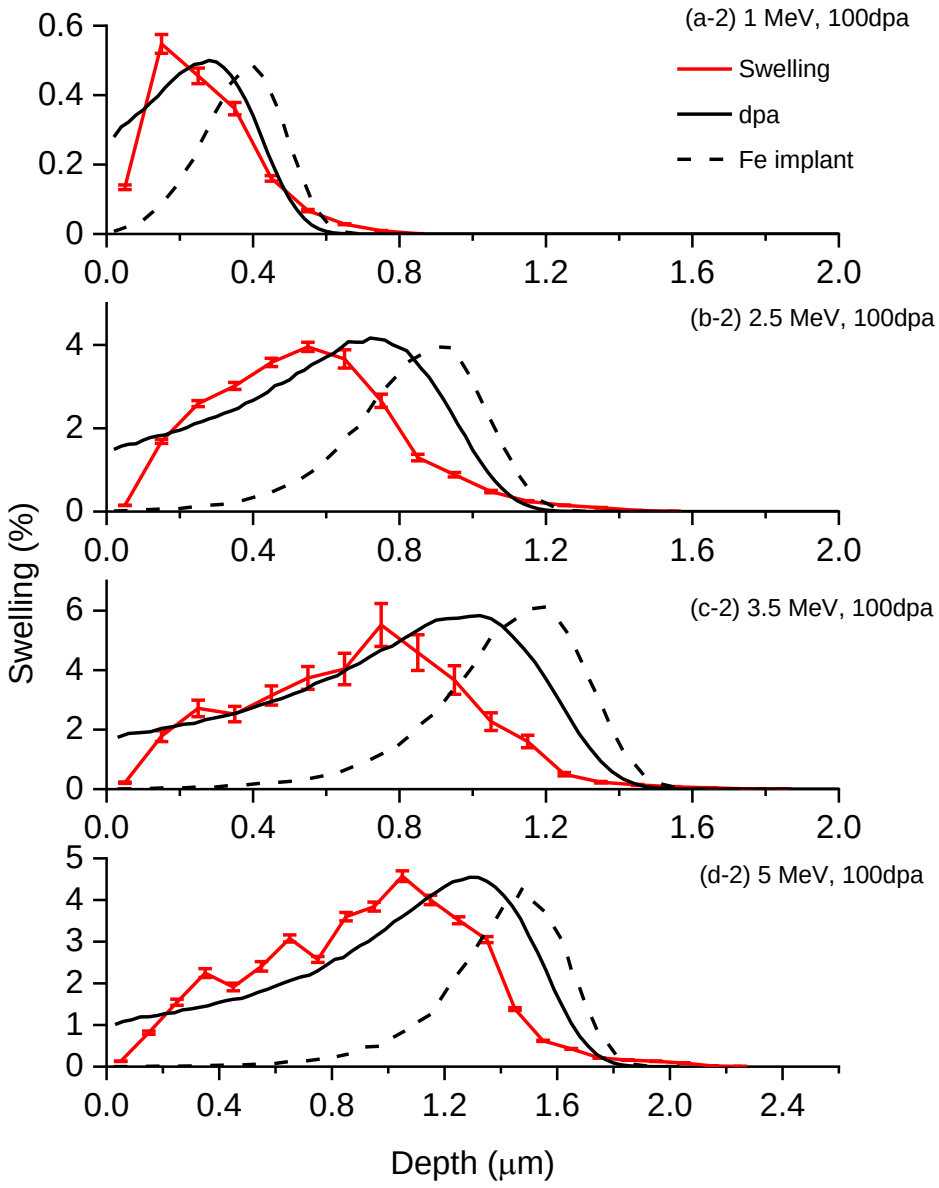

Figure 3. 13 The void swelling distribution of pure Fe irradiated by Fe2+ ions with the energy of (a-1) 1 MeV, 50 dpa, (a-2) 1 MeV, 100 dpa, (b-1) 2.5 MeV, 50 dpa, (b-2) 2.5 MeV, 100 dpa, (c-1) 3.5 MeV, 50 dpa, (c-2) 3.5 MeV, 100dpa, (d-1) 5 MeV, 50 dpa, and (d-2) 5 MeV, 100 dpa. All irradiations have the same temperature at 475 ℃ and at the same peak dpa rate of $1.2 \times 10^{-3}\ dpa/s$. The solid lines are dpa profiles with corresponding irradiation energies, and the dash lines are the Fe ions implantation ranges.

Figure 3.14 shows the curves of void swelling versus local dpa in pure Fe irradiated by Fe ions with the energy of 1 MeV, 2.5 MeV, 3.5 MeV, and 5 MeV, respectively. The irradiation doses are 50 peak dpa and 100 peak dpa. All have the same temperature of 475 ℃ and the fixed peak dpa rate of $1.2 \times 10^{-3}\ dpa/s$. The void swelling curves show the parallel shifting between 50 peak dpa and 100 peak dpa for all irradiations. At first, the void swelling increases fast in the near-surface region and then slows down and approaches another growth stage with a relatively lower swelling rate. For example, in the 5 MeV irradiation, the swelling rate is around 0.35% per dpa, then it decreases to around 0.06% per dpa for the third depth point, as shown in figure 3.14 (a).

Suppose the swelling of 5MeV irradiation with the dose of 50 peak dpa shows a truly dpa dependent relationship. In that case, the swelling of 100 dpa irradiation should follow the same tendency, and the parallel shifting should not happen. It was because of the free surface effect, the void swelling in the near-surface region was suppressed. Figure 3.15 shows the schematic of swelling versus local dpa values for two depth locations. These two lines indicate two different depths. Figure 3.15 (a) shows the expected swelling versus local dpa if there is no surface effect. The blue arrows represent the swelling growth at the same depth point with the increase of local dpa for different samples. All the depth points should follow the same swelling-dpa dependence relationship due to the absence of the surface effect. However, if the surface effect exists and suppresses the void swelling, the swelling rate at different depths will differ. As figure 3.15 (b) shown, under the surface effect, the shallow point may follow a low swelling per dpa, and the second depth point

will follow a slightly increased swelling per dpa. The parallel shifting is shown due to the swelling rate difference.

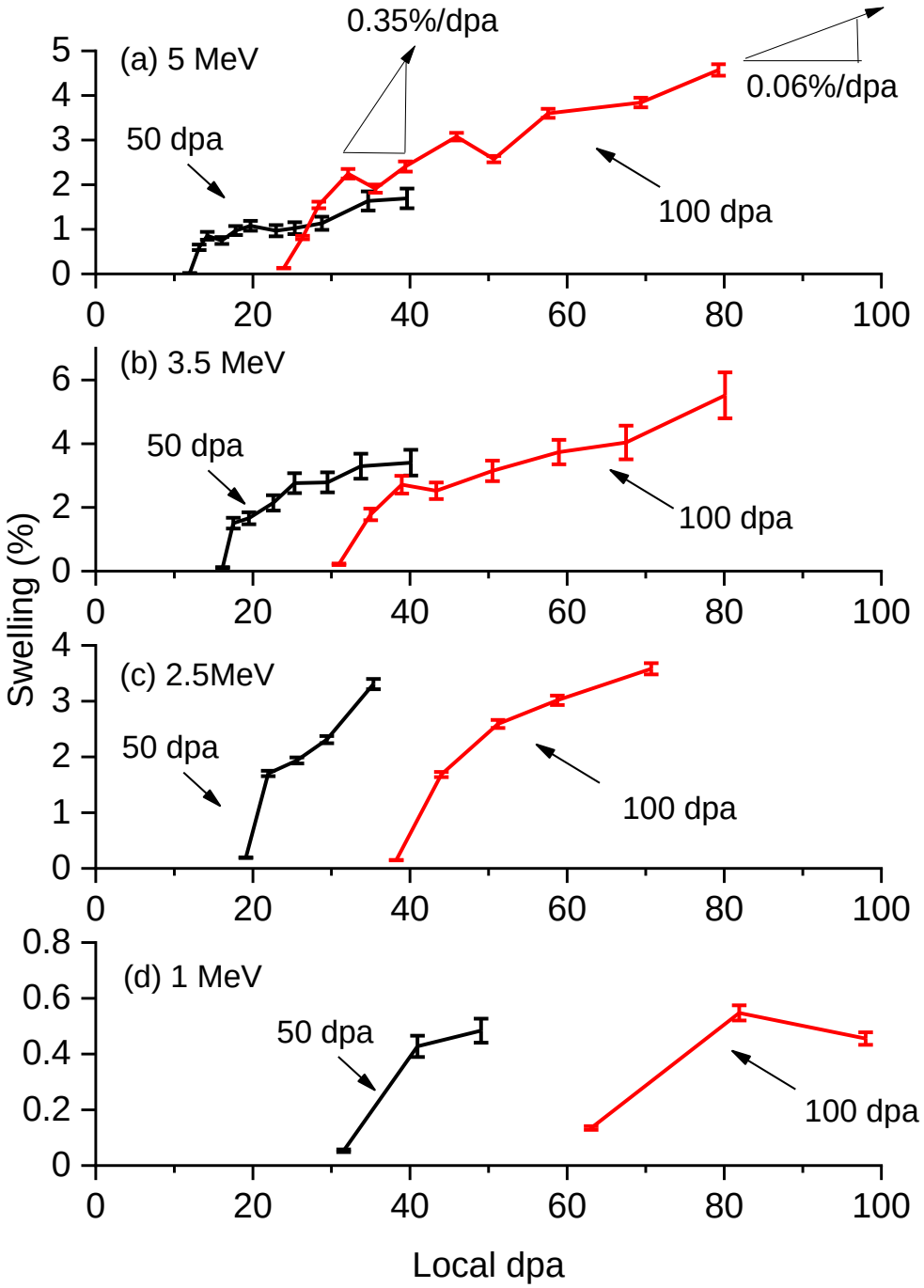

Figure 3. 14 Void swelling versus local dpa in Fe irradiated by Fe ions with the energy of (a) 5 MeV, (b) 3.5 MeV, (c) 2.5 MeV, and (d) 1 MeV. All irradiations have the same temperature at 475 ℃, and the peak dpa rate is fixed as 1.2×10^{-3} dpa/s.

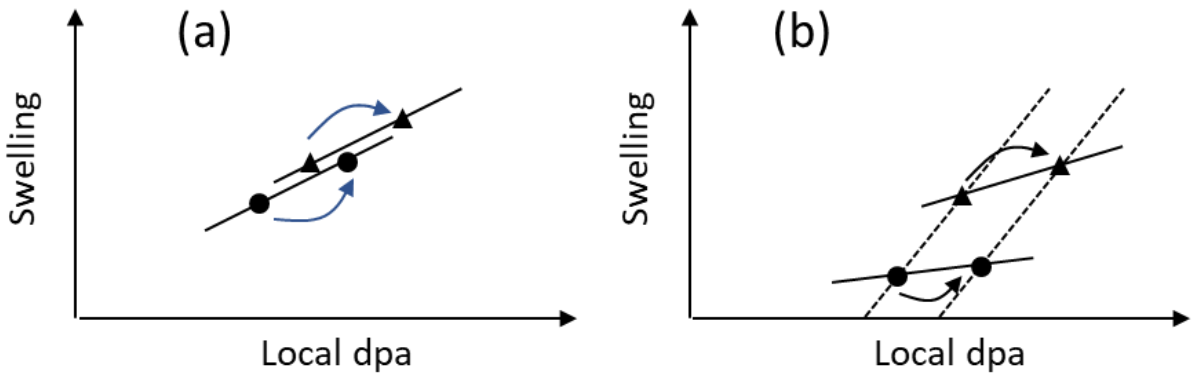

Figure 3. 15 Schematics of swelling versus local dpa values for two depth locations for (a) both depth points follow the same swelling rate and (b) two depth points have different swelling rates.

Back to figure 3.14, the first depth point of swelling curves of all irradiation conditions is located either completely or partially in the void denuded zones. Their swelling values are either zero or very close to zero. The parallel shifting was shown for all the points for the second swelling points in all 100 dpa curves. The third depth points of 100 dpa irradiation curves (figure 3.14 a, b, and c) join other high dpa points. Hence, this depth point is not affected by the surface effect. Note depth slab is 100 nm thick, and the first depth point starts at 50 nm. The studies roughly suggest that swelling is affected for the first 200 nm in all irradiation conditions.

Figure 3.16 shows the void density as a function of depth for irradiation of (a-1) 5 MeV, (b-1) 3.5 MeV, (c-1) 2.5 MeV, and (d-1) 1 MeV Fe, and void density as a function of local dpa for irradiation of (a-2) 5 MeV, (b-2) 3.5 MeV, (c-2) 2.5 MeV, and (d-2) 1 MeV, respectively. The dash curves are dpa profiles, and the solid curves are Fe profiles. On the

left side, figure 3.16 (a-1), (b-1), (c-1), and (d-1) compare the void densities distribution as a function of depth. The void densities of all irradiation conditions quickly rise up in the near surface region (around 100 to 200 nm depths), then the void densities start to decrease with the increase of depth and reach the minimum value at the depth roughly the same as the local dpa peak depth. After that, the void densities recover and start increasing to a local peak value at the deeper region, which is around 200 to 400 nm depth deeper than the local dpa peak depth for all irradiation conditions from 1 MeV to 5 MeV.

The right side of figure 3.16 shows the void densities distribution as a function of local dpa. As guidance, blue arrowed lines refer to the direction of increasing depths towards the dpa peak (depths shallower than the dpa peak), while red arrowed dot lines refer to the direction of increasing depths beyond the dpa peak (depth deeper than the dpa peak). For all irradiation conditions, the void densities increase quickly with the increase of local dpa in the near surface region (around 100 to 200 nm depths). Then, void densities start decreasing with the increase of local dpa and reach the minimum value at the local dpa peak position. In the region where the depths are deeper than the dpa peak and the regions where the depths are shallower than the dpa peak position, the void densities roughly follow the same local dpa dependence. They do not have obvious differences for the two regions.

The absence of hysteresis in the density-dpa relationship suggests that injected interstitial effect does not influence void densities (or such effect turns to be minimal or ignorable). The injected interstitials effect may change overall swelling or void sizes but do not diminish voids. Otherwise, the curves for depths deeper than the dpa peak should

be systematically lower than the depth region shallower than the dpa peak since the peak of the injected interstitial is located deeper than the dpa peak.

Thus, if the void density will not be affected by injected interstitials effect, then the void density distribution as a function of local dpa in the region deeper than the local dpa peak position (where will not be affected by the free surface effect because such region is far away from the surface) will represent the true relationship between void density and local dpa. Thus, the curves can be used to quantitatively determine the region where will be affected by the free surface. As the green arrows shown in figure 3.16 (a-2), (b-2), (c-2), and (d-2), point out the depths where the steep rise of surface point or its extension begins to intersect the reference curves. The measured depths are 202 nm (for 5 MeV), 193 nm (for 3.5 MeV), 136 nm (for 2.5 MeV), and 110 nm (for 1 MeV). The depths of the ending point of the surface effect increase with the increase of beam energies. Such trend changes are expected considering that the near-surface local dpa rates increase with decreasing beam energies. Although the depths of the surface-effect-affected zones are deeper than the void denuded zones (as observed from the present studies), both are related to the vacancy profiles at the surface, which have characteristic depths proportional to $(D_V/K)^{1/4}$ [18].

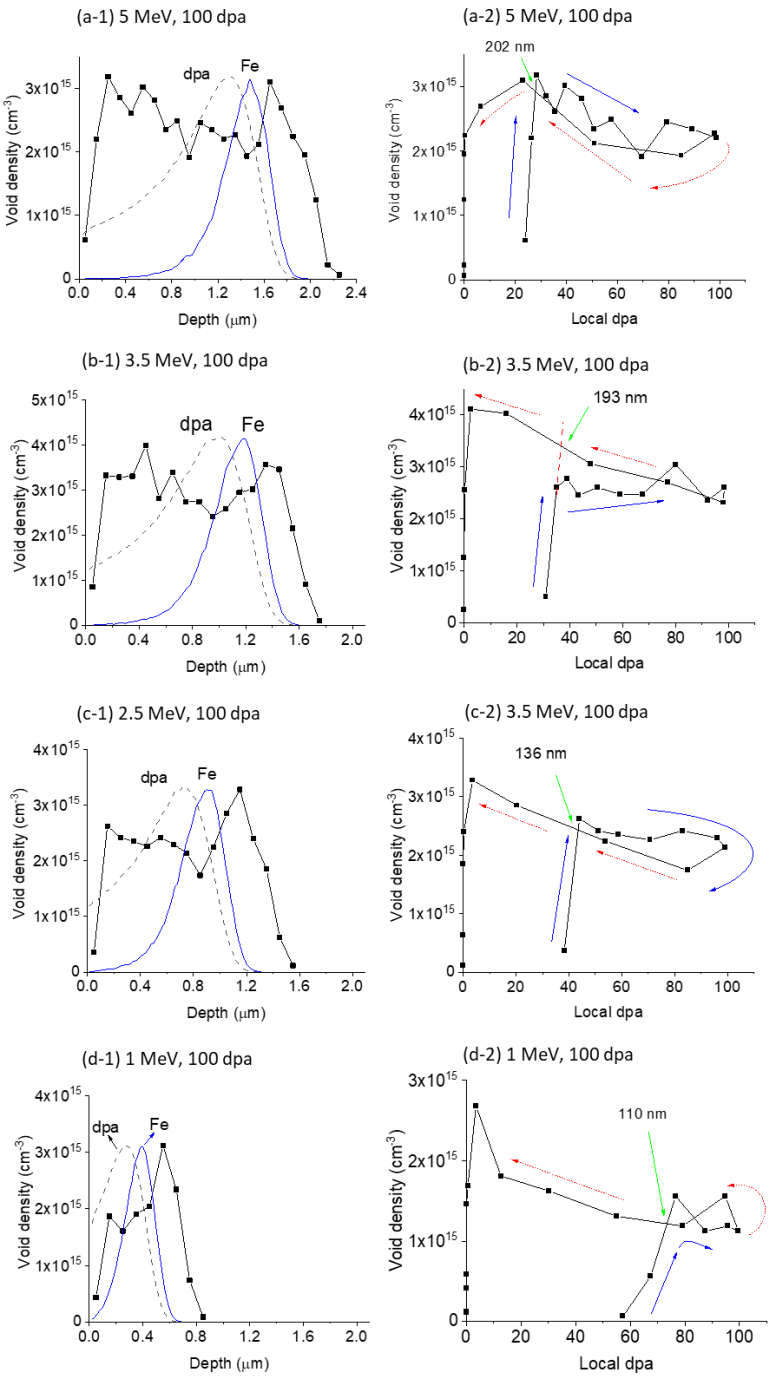

Figure 3. 16 Void density as a function of depth for irradiation of (a-1) 5 MeV, (b-1) 3.5 MeV, (c-1) 2.5 MeV, and (d-1) 1 MeV Fe, and void density as a function of local dpa for irradiation of (a-2) 5 MeV, (b-2) 3.5 MeV, (c-2) 2.5 MeV, and (d-2) 1 MeV. The dash curves are dpa profiles and the solid curves are Fe profiles. The arrowed

blue lines refer to increasing depth towards the dpa peak location, and the arrowed red dot lines refer to increasing depth away from the dpa peak location.

3.3.3 MOOSE Simulation

The analytical solutions of one-dimensional defect distribution in the near-surface region of a bulk containing defect trapping sites were given in the previous studies [6]. The solutions consider various conditions, from defect trapping dominated case to the defect recombination dominated case [6]. The change from one extreme case to the other does not change too much the profile shape. The normalized profile is approximated by $1 - \exp(-\beta X)$, where X is a function of depth, vacancy diffusivity, and local dpa rate. The solutions did not differentiate interstitials and vacancies. Also, the solutions are point defect distribution, which is not exactly the experimentally measured void swelling. To close the gap, we modeled the defect interactions and defect-surface interactions using rate theory implemented in MOOSE, the Multi-Physics Object Oriented Simulation Environment [19]. The defect reaction equations, including defect annihilation, trapping, and diffusion, are given by

$$\frac{\partial C_v}{\partial t} = f_{survive} K_0 - K_{\perp,v} \rho_\perp C_v - K_{iv} C_v C_i + \nabla D_v \nabla C_v \qquad (3\text{-}35)$$

And

$$\frac{\partial C_i}{\partial t} = [f_{survive}(1 - f_{i-cluster}) K_0 + K_{II}] - K_{\perp,i} \rho_\perp C_i - K_{iv} C_i C_v + \nabla D_i \nabla C_i \qquad (3\text{-}36)$$

Where C_v and C_i are concentrations of vacancies and interstitials, $f_{survive}$ is the survival fraction of defects after damage cascade creation, K_0 is the defect creation rate, $K_{\|}$ is the

Fe introduction rates as the injected interstitial source, $K_{\perp}$ is the dislocation sink strength, K_{iv} is the point defect recombination rate, D_v and D_i are diffusivities of vacancies and interstitials, respectively. For defect creation rate K_0 as a function of depth, SRIM-2013 code was used to create the input file. The major parameters used in the simulation are listed in table 3.6.

The same approach has been previously used to understand injected interstitial effects and details of void profiles in self-ion-irradiated Fe. Further details can be found in reference 20 [20]. The modeling has no intention to predict void growth and full-scale defect clustering involving void growth and dislocation evolution. Rather, the modeling is used to provide some insights into surface effect, using a simplified approach. The simplifications assumed that (1) dislocations, as the major biased defect sink for interstitials, are fixed without time evolution, (2) voids, as neutral defect sinks for interstitials and vacancies are ignored.

The void nucleation rate at the moment of forming stable void nuclei is approximated by using vacancy supersaturation level, calculated by [20]

$$\log(J_V) = 5.41547 \log(S_v) - 14.6586 \tag{3-37}$$

$$S_v = \frac{D_v C_v - D_i C_i}{D_v C_v^*} \tag{3-38}$$

Figure 3.17 (a) shows the normalized nucleation rate in pure Fe irradiated by 5 MeV Fe ions at three peak dpa rates (2×10^{-4}, 1.2×10^{-3}, and 6×10^{-3} dpa/s). Note that the dpa rates and irradiation temperature of 475 ℃ match the experimental conditions. The peak value normalizes the nucleation rates at the location of the peak dpa. In the near-surface region, nucleation rates are reduced, corresponding to the formation of void denuded zones. The profile difference extends to deep depths but is most noticeable from the surface up to about half of the Fe projected range (~500 nm). Comparisons show that the void nucleation profiles are higher for lower peak dpa rates. Consequently, lower dpa rates create narrower void denuded zones.

Table 3.6 Parameters used for the present simulations.

Property	Value	Unit	Source
T	475	℃	
Peak dpa rate	$1.2 \cdot 10^{-3}$	DPA/sec	
D_{0_v}	$8.016 \cdot 10^{11}$	nm^2/s	[21]
D_{0_I}	$2.09 \cdot 10^{11}$	nm^2/s	[22]
E_{m_v}	0.86	eV	
E_{m_i}	0.17	eV	[22]
$r_{\perp_v}$	1.2	nm	[23]
$r_{\perp_i}$	3.6	nm	[23]
$\rho_{\perp}$	10^{-5}	$\#/nm^2$	[24]
∂_{Fe}	0.286	nm	at 475 ℃
$f_{survive}$	25	%	[25]
$f_{i-cluster}$	30	%	[26]

Figure 3.17 (b) shows the void nucleation rate distribution in the very shallow depth region, for irradiation using the peak dpa rate of 1.2×10^{-3} dpa/s. There are two characteristic depths marked. The shallow one (at the depth of 101 nm) is the void denuded zone as identified from figure 3.3. The thickness loss (11 nm) due to sputtering, estimated from SRIM code, is added to TEM identified void denuded zone (90 nm). The deep marker (at the depth of 200 nm) refers to the boundary of the swelling-affected region. Both depths fall into modeling predicted region which have reduced void nucleation rates.

The corresponding normalized nucleation rate at the boundary of the void denuded zone is 0.3%. The rate at the boundary of the swelling affected zone is 2%. Note that the rates are normalized to the peak value at the dpa peak location. Since the void denuded zone is sensitive to the local dpa rate, instead of peak dpa rate, as observed in figure 3.8, it makes more sense to compare the local rate in the near surface region. If the rate at the depth of 250 nm, 3%, is used for the normalization, then the void denuded zone corresponds to 10% of the value at 250 nm, and the swelling-affected zone corresponds to 66% of the value at 250 nm. In the previous studies, it is assumed that void absence occurs when the vacancy concentration falls below a critical fraction of the bulk value. This critical number was not experimentally determined. The faction values of 10% for creating void denuded zone and 66% for creating swelling-affected zones, in comparison with local average at deeper depth are useful for future modeling estimation.

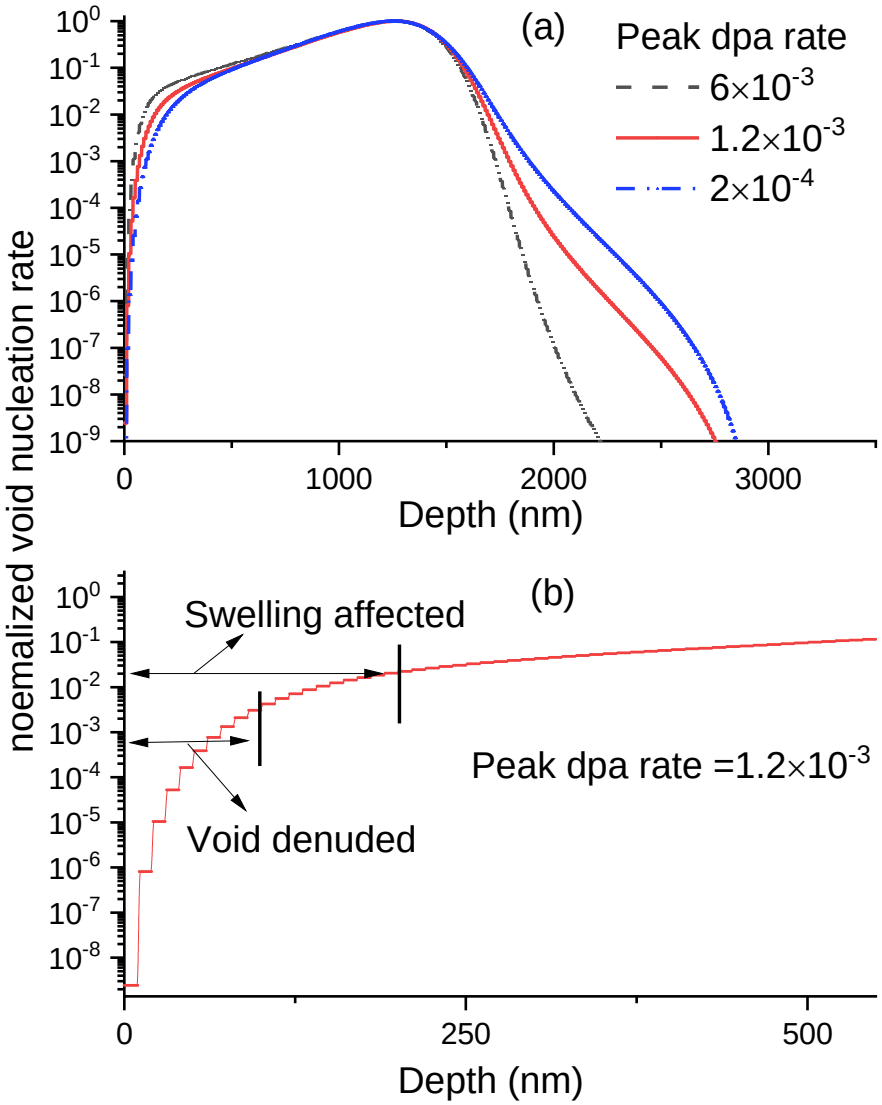

Figure 3. 17 (a) Depth profiles of normalized void nucleation rates in Fe irradiated by 5 MeV Fe ions at the peak dpa rates of 2×10^{-4}, 1.2×10^{-3}, and 6×10^{-3} dpa/s, and (b) the profile for the peak dpa rate of 1.2×10^{-3} dpa/s. Depth profiles of normalized void nucleation rates in Fe irradiated by 5 MeV Fe ions at the peak dpa rates of 2×10^{-4}, 1.2×10^{-3}, and 6×10^{-3} dpa/s, and (b) the profile for the peak dpa rate of 1.2×10^{-3} dpa/s.

Reference

[1] Han, W. Z., M. J. Demkowicz, E. G. Fu, Y. Q. Wang, and A. Misra. "Effect of grain boundary character on sink efficiency." Acta materialia 60, no. 18 (2012): 6341-6351.

[2] Millett, Paul C., Anter El-Azab, Srujan Rokkam, Michael Tonks, and Dieter Wolf. "Phase-field simulation of irradiated metals: Part I: Void kinetics." Computational materials science 50, no. 3 (2011): 949-959.

[3] Sekio, Yoshihiro, Shinichiro Yamashita, Norihito Sakaguchi, and Heishichiro Takahashi. "Void denuded zone formation for Fe–15Cr–15Ni steel and PNC316 stainless steel under neutron and electron irradiations." Journal of Nuclear Materials 458 (2015): 355-360.

[4] Chen, C. W., and R. W. Buttry. "Void formation and denudation in ion-irradiated nickel." Radiation Effects 56, no. 3-4 (1981): 219-228.

[5] Zinkle, So J., and K. Farrell. "Void swelling and defect cluster formation in reactor-irradiated copper." Journal of Nuclear Materials 168, no. 3 (1989): 262-267.

[6] Lam, Nghi Q., Steven J. Rothman, and Rudolf Sizmanns. "Steady-state point-defect diffusion profiles in solids during irradiation." Radiation Effects 23, no. 1 (1974): 53-59.

[7] Konobeev, Yu V., A. V. Subbotin, V. N. Bykov, and V. I. Tscherbak. "Grain boundary void denuded zone in irradiated metals." physica status solidi (a) 29, no. 2 (1975): K121-K124.

[8] Sekio, Y., I. Yamagata, N. Akasaka, and N. Sakaguchi. "Evaluation of irradiation-induced point defect migration energy during neutron irradiation in modified 316 stainless steel." (2018).

[9] Garner, F. A., M. B. Toloczko, and B. H. Sencer. "Comparison of swelling and irradiation creep behavior of fcc-austenitic and bcc-ferritic/martensitic alloys at high neutron exposure." Journal of Nuclear Materials 276, no. 1-3 (2000): 123-142.

[10] Gigax, J. G., Tianyi Chen, Hyosim Kim, Jing Wang, L. M. Price, Eda Aydogan, Stuart Andrew Maloy et al. "Radiation response of alloy T91 at damage levels up to 1000 peak dpa." Journal of Nuclear Materials 482 (2016): 257-265.

[11] Gigax, Jonathan G., Hyosim Kim, Tianyi Chen, F. A. Garner, and Lin Shao. "Radiation instability of equal channel angular extruded T91 at ultra-high damage levels." Acta Materialia 132 (2017): 395-404.

[12] Smidt, F. A., P. R. Malmberg, J. A. Sprague, and J. E. Westmoreland. "Swelling behavior of commercial ferritic alloys, EM-12 and HT-9, as assessed by heavy ion bombardment." In Irradiation Effects on the Microstructure and Properties of Metals. ASTM International, 1976.

[13] Gigax, Jonathan G., Eda Aydogan, Tianyi Chen, Di Chen, Lin Shao, Y. Wu, W. Y. Lo, Y. Yang, and F. A. Garner. "The influence of ion beam rastering on the swelling of self-ion irradiated pure iron at 450á C." Journal of Nuclear Materials 465 (2015): 343-348.

[14] Gigax, Jonathan G., Hyosim Kim, Eda Aydogan, Frank A. Garner, Stu Maloy, and Lin Shao. "Beam-contamination-induced compositional alteration and its neutron-atypical consequences in ion simulation of neutron-induced void swelling." Materials Research Letters 5, no. 7 (2017): 478-485.

[15] Schneider, Caroline A., Wayne S. Rasband, and Kevin W. Eliceiri. "NIH Image to ImageJ: 25 years of image analysis." Nature methods 9, no. 7 (2012): 671-675.

[16] Abràmoff, Michael D., Paulo J. Magalhães, and Sunanda J. Ram. "Image processing with ImageJ." Biophotonics international 11, no. 7 (2004): 36-42.

[17] Sigmund, Peter. "Theory of sputtering. I. Sputtering yield of amorphous and polycrystalline targets." Physical review 184, no. 2 (1969): 383.

[18] E. M. Bringa, J. D. Monk, A. Caro, A. Misra, L. Zepeda-Ruiz, M. Duchaineau, F. Abraham, M. Nastasi, S. T. Picraux, Y. Q. Wang, and D. Farkas, Are Nanoporous Materials Radiation Resistant?, Nano Letters 12, 3351–3355 (2012).

[19] D. Gaston, Nucl. Eng. Des. 239, 1768-1778 (2009).

[20] M.R. Short, D.R. Gaston, M. Jin, L. Shao, F.A. Garner, Modeling injected interstitial effects on void swelling in self-ion-irradiation experiments, J. Nucl. Mat. 471, 200-207 (2016).

[21] Borodin, V. A., & Vladimirov, P. V. (2007). Diffusion coefficients and thermal stability of small helium–vacancy clusters in iron. Journal of nuclear materials, 362(2-3), 161-166.

[22] Soneda, N., Ishino, S., & De la Rubia, T. D. (2001). Vacancy loop formation by'cascade collapse'in a-Fe: A molecular dynamics study of 50keV cascades. Philosophical magazine letters, 81(9), 649-659.

[23] Shastry, V., & Diaz de la Rubia, T. (1999). The interaction between point defects and edge dislocation in bcc iron. 126-128.

[24] H. Bhadeshia, R. Honeycombe, Steels: Microstructure and Properties: Microstructure and Properties, Butterworth-Heinemann, 2011, p. 23.

[25] Malerba, L. (2006). Molecular dynamics simulation of displacement cascades in α-Fe: A critical review. Journal of nuclear materials, 351(1-3), 28-38.

[26] Malerba, L. (2006). Molecular dynamics simulation of displacement cascades in α-Fe: A critical review. Journal of nuclear materials, 351(1-3), 28-38.

CHAPTER 4

INJECTED INTERSTITIALS EFFECT

4.1 Introduction

Injected interstitial effect has been well known due to the suppressive of void swelling in ion irradiated metals [1-6]. Two sources can introduce the injected interstitials. First, during irradiation, the implanted ions will be introduced into the materials as the extra atoms. Also, due to the distribution difference of the collision-produced interstitials and vacancies [1], interstitials will distribute at the deeper region compared to vacancies.

The injected interstitial effect has been well known in the semiconductor industry for modeling dopant diffusion [7-8]. Dopants such as boron atoms in silicon diffuse exclusively via an interstitial diffusion mechanism, in which boron needs the assistance of a silicon interstitial to start diffusion [9]. Silicon has high efficiency in point defect recombination. Hence, the point defects created from collisions are ignored in modeling. For interstitials responsible for boron diffusion, they come from excessive interstitials introduced at the projected range. As a good practice in computation simplification, interstitials are assumed to be equal to the implanted dopants. This is called “+1” model in semiconductor modeling [8].

In “+1” model, Si interstitials are assumed to be equal to implanted ions, regardless of the types of ion species implanted. This is due to the fact that implanted atoms quickly

occupy the lattice locations, and an equal number of interstitials is created. The same thing occurs in metals. Interstitials in metal diffuse as dimmers. This means that a newborn interstitial will push a lattice atom to form a dimmer. One of the interstitials in the dimmer will push the next neighbor to form a new dimmer, and the other atom in the original dimmer will take the lattice site to become a substitutional atom. In other words, trace atoms or implanted ions can stop diffusion, but the induced interstitials will continuously diffuse.

The first key point of the above discussion is that the diffusivity of implanted ion species should not be used in modeling injected interstitial effect. Rather, the diffusivity of self-interstitials should be used. The second key point is that, since interstitials interact with defect sinks of various types, rate theory modeling, which considers defect clustering, defect-sink interactions, and sink evolution, needs to be used. Such a full-scale modeling capability linkable to experimental time and length scale, however, is yet to be developed.

4.2 Experiment Procedure

The <111> oriented single-crystal Fe of purity 99.94+% (purchased from Accumet Materials Inc., Ossining, NY, USA) was used. The high purity and the absence of grain boundaries avoid or minimize the complexity from defect-impurity trapping and defect-

grain boundary interactions. The specimens were cut into small pieces, mechanically polished by using SiC papers from 400 grit down to 4000 grit, and electropolished as the last step. The twin-jet electro polisher with the solution of 5% perchloric acid and 95% methanol was used for the electropolishing.

Specimens were irradiated with Fe2+ ions of 1 MeV, 2.5 MeV, 3.5 MeV, and 5 MeV, respectively, all to 100 peak dpa. The irradiation temperature was 475 ℃. A static beam of 5 mm in diameter was used to avoid the pulse beam effect [10]. The multi-beam deflectors were used to filter out contaminants [11]. The vacuum was kept at 6×10-8 torr or better during irradiation. Multiple thermocouples were mounted on the hot stage for temperature reading. The overall temperature fluctuation during irradiations was less than ± 5°C. All irradiations were performed using roughly the same peak dpa rate at 1.2×10-3 dpa/s. Fluence determination and damage calculations used the Stopping and Range of Ions in Matter (SRIM) codes [12]. The Kinchin-Pease (KP) model was selected [13]. The Fe displacement energy was 40 eV [14].

FIB technique was used to prepare the TEM lamella. TEM characterization used FEI Tecnai F20 operated at 200 kV. ImageJ was used for void analysis [15]. Local swelling was calculated by $Swelling\ \% = V\%/(1 - V\%)$, where $V\%$ is the volume fraction of voids.

4.2 Results

In Figure 4.1, voids distributions as a function of depth were shown for 1 MeV, 2.5 MeV, 3.5 MeV, and 5 MeV irradiations compared with the corresponding Cross-sectional TEM micrographs. On the left side is the typical cross-sectional TEM micrograph. The middles are SRIM-calculated dpa and Fe implant profiles. On the right side are the plots of void density as a function of void sizes (measured by using ImageJ) at each depth point. The depth interval for 5 MeV, 3.5 MeV, and 2.5 MeV irradiations are 200 nm, and for 1 MeV irradiation is 100 nm depth due to the shallow voids distribution. It should be noted that the analysis regions are much wider than the TEM image selected to be shown here. The total number of counted voids are 1300 (for 5 MeV), 2200 (for 3.5 MeV), 1785 (for 2.5 MeV), and 997 (for 1 MeV), respectively. As the right figures shown in figure 4.1, the heigh of each depth interval was scaled to the total analytical amount of the voids in such region with a given size. It is obvious that the Gauss-like distributions are shown for all energies and all depth intervals. Then, the average void size can be obtained from each depth and used for later discussion. The dash curves represent the changes of average void size as a function of depth. It shows that, at first, the average void size increases with increasing depth and reaches the maximum value at the depth a little shallower than the depth of the dpa peak. Then the average void size decreases and reaches the minimum value at the deepest region. For example, as shown in figure 4.1 a, for the 5 MeV irradiation, the average void size in the near-surface region (at a depth of 100 nm) is 15 nm, it reaches the largest size as 29 nm at a depth of 1100nm, then the average void size

turns to decrease and reaches the minimum size of 11 nm at a depth of 2000 nm. For the 1 MeV irradiation, like shown in figure 4.1 (d), the sizes of the voids are obviously smaller than other irradiation conditions (2.5 MeV, 3.5 MeV, and 5 MeV). This phenomenon will be introduced as evidence that there is no “safe zone” for the 1 MeV Fe irradiation.

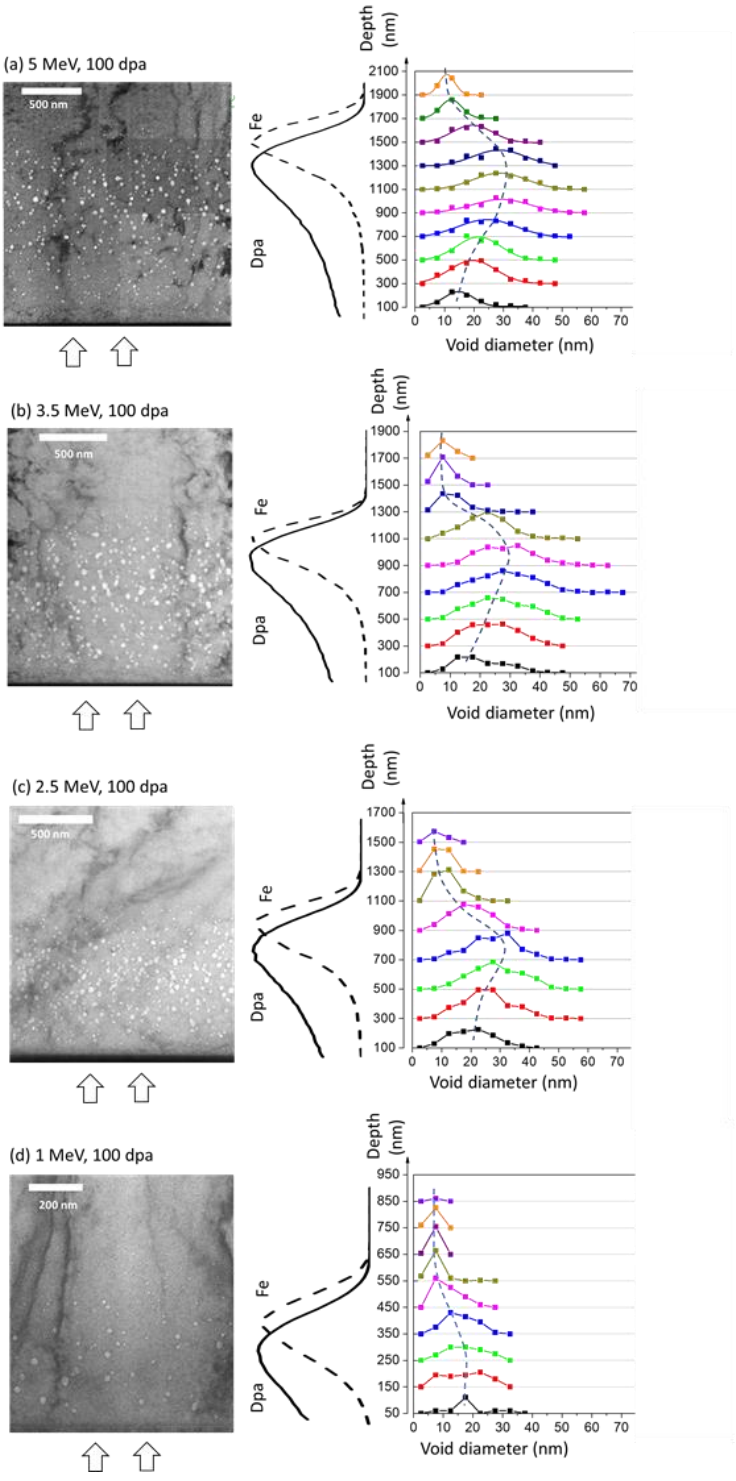

Figure 4. 1 Cross-sectional TEM micrographs and void statistical analysis as a function of depth for (a) 5 MeV, (b) 3.5 MeV, (c) 2.5 MeV, and (d) 1 MeV Fe ion irradiation at 475°C. SRIM-calculated dpa and Fe profiles are also shown.

Figure 4.2 shows the average void size distribution as a function of depth (left figures) and the average void size changes with local dpa (right figures) for 1 MeV, 2.5 MeV, 3.5 MeV, and 5 MeV irradiations. In the left figure, the dashed line refers to the local dpa distribution calculated by using SRIM. It clearly shows that the average void size increase with increasing depth and reaches the maximum value slightly shallower than the dpa peak positions. It results from the injected interstitials effect. If the injected interstitials do not affect such regions, the average void size peak should distribute at the same depth as the local dpa peak.

The injected interstitial effect is amplified by plotting the void sizes as a function of local dpa, as the right figures show. The average void size increase with increasing local dpa, and then it drops suddenly before the local dpa reaches the peak value. Also, the average void sizes in the region deeper than the local dpa depth are systematically smaller than the region shallower than the local dpa depth.

If there is no injected interstitials effect, the void size should increase with increasing local dpa and grow to the maximum size at the peak dpa depth. Furthermore, the hysteresis behavior of average void size shallower and deeper than the peak dpa depth should not happen. The dpa dependence curves should be the same for depths shallower than the dpa peak and depths deeper than the peak.

Two assumptions are required to quantitatively define the depth points where the injected interstitials have a role in affecting the voids and define where the void sizes begin to deviate from the “expected” curves. The first assumption is that the local swelling is

proportional to the local dpa, which can be easily justified from the well-known observation that swelling increases linearly as a function of dpa, i.e., about 1% per dpa for some FCC metals and about 0.2% per dpa for some BCC metals.

The second assumption is that the competitive growth Ostwald ripening theory can be used to predict the void swelling evolution in irradiated materials. Generally, the classical Ostwald ripening theory indicates that the size of the precipitates will increase with time, and the density will decrease. Under non-zero volume approximation, precipitate sizes changes have additional dependence on total precipitate volumes. The sizes are proportional to the square root of the total volume. One big challenge is that classical Ostwald ripening theory is for a closed system in which total solute numbers are conservative. The number of solutes in precipitates may change, but the total of precipitated and un-precipitated atoms is a constant. However, In ion/neutron irradiation, the number of total defects increases as a function of time, which is an open system. To link the classical Ostwald ripening theory (the volume is conservative) and the non-conservative Ostwald ripening, the time evolution of voids is treated as step height like distribution. Hence, the volume is fixed for a certain time window, the newly added void volume during ripening can be approximated as the starting void volume. If so, void sizes will evolve as a function of the square root of total swelling, or alternatively, local dpa values (based on the first assumption). On the right side of Figure 4.2, the dashed line refers to the plot of average void size as a function of $\sqrt{local\ dpa}$ with a fitting parameter. Then, the dashed line can be used as the reference to identify the injected interstitials effect start point. On the right side of figure 4.2, the arrows show the starting point of injected

interstitials effect. For example, for 5 MeV irradiation (a-2), the injected interstitial effect's starting point is 950 nm. For 3.5 MeV irradiation, as shown in figure 4.2 (b-2), the starting depth of injected interstitials effect is 750 nm, and 550 nm for 2.5 MeV irradiation (as shown in figure 4.2 (c-2)). However, the average void size for 1 MeV irradiation, as shown in figure 4.2 (d-2), starting decrease with the increase of local dpa even at the first depth point. The trend is completely off compared to other irradiation conditions. It also can be used as evidence that there is no “safe zone” for such low energy irradiations. The whole region will be affected by both the surface effect and injected interstitials effect.

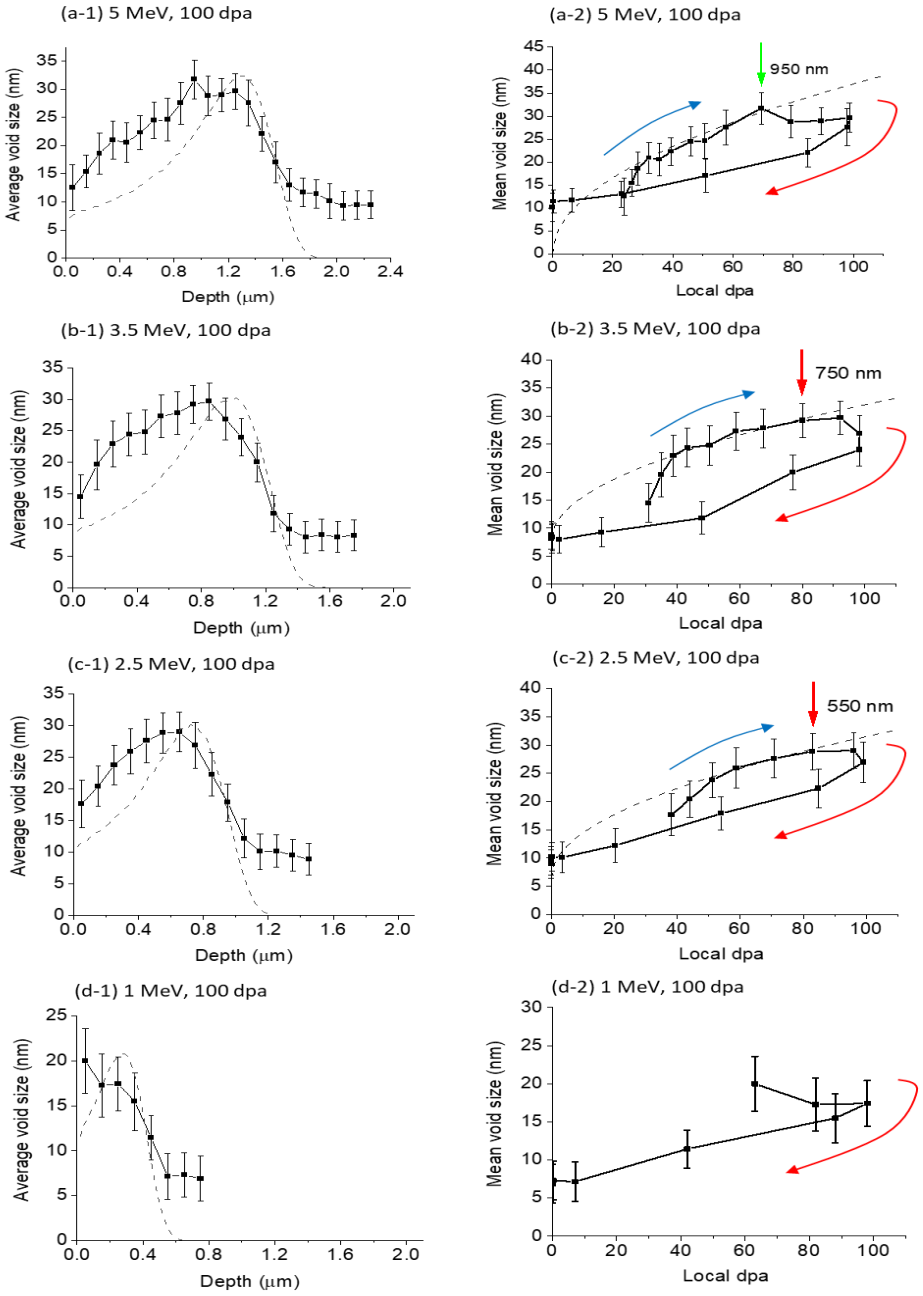

Figure 4.2 Void size as a function of depth for irradiation of (a-1) 5 MeV, (b-1) 3.5 MeV, (c-1) 2.5 MeV, and (d-1) 1 MeV Fe, and void size as a function of local dpa for irradiation of (a-2) 5 MeV, (b-2) 3.5 MeV, (c-2) 2.5 MeV, and (d-2) 1 MeV.

Reference

[1] Lin Shao, C.-C. Wei, J. Gigax, A. Aitkaliyeva, D. Chen, B.H. Sencer, F.A. Garner, Effect of defect imbalance on void swelling distributions produced in pure iron irradiated with 3.5 MeV self-ions, J. Nucl. Mat. 453, 176-181 (2014).

[2]E. Kuramoto, N. Yoshida, N. Tsukuda, K. Kitajima, N.H. Packan, M.B. Lewis, L.K. Mansur, Simulation irradiation studies on iron, J. Nucl. Mater., 103&104, 1091 (1981)

[3] D.L. Plumton, W.G. Wolfer, Suppression of void nucleation by injected interstitials during heavy ion bombardment, J. Nucl. Mater., 120, 245-253 (1984)

[4] E.H. Lee, L.K. Mansur, M.H. Yoo, Spatial variation in void volume during charged particle bombardment — the effects of injected interstitials, J. Nucl. Mater., 85&86, 577-581 (1979).

[5] D.B. Bullen, G.L. Kulcinski, R.A. Dodd, Swelling suppression by injected self-interstitials, Nucl. Instr. Methods Phys. Res., B10/11, 561-564 (1985)

[6] J.B. Whitley, G.L. Kulcinski, P. Wilkes, H.V. Smith Jr., The depth dependent damage profile in nickel irradiated with nickel or copper ions, J. Nucl. Mater. 79, 159-169 (1979)

[7] L. Shao, X. Lu, X. Wang, I. Rusakova, J. Liu, W.-K. Chu, Retardation of boron diffusion in silicon by defect engineering, Appl. Phys. Lett., 78, 2321-2323 (2001).

[8] M. Giles, Transient Phosphorus Diffusion Below the Amorphization Threshold, J. Electrochem. Soc. 138, 1160 (1991).

[9] Lin Shao, Jiarui Liu, Quark Y Chen, Wei-Kan Chu, Boron diffusion in silicon: the anomalies and control by point defect engineering, Materials Science and Engineering: R: Reports 42, 65-114 (2003).

[10] Jonathan G Gigax, Eda Aydogan, Tianyi Chen, Di Chen, Lin Shao, Y Wu, WY Lo, Y Yang, FA Garner, The influence of ion beam rastering on the swelling of self-ion irradiated pure iron at 450°C, J. Nucl. Mat. 465, 343-348 (2015).

[11] Jonathan G. Gigax, Hyosim Kim, Eda Aydogan, Frank A Garner, Stu Maloy, Lin Shao, Beam-contamination-induced compositional alteration and its neutron-atypical consequences in ion simulation of neutron-induced void swelling, Mat. Res. Lett. 5, 478-485 (2017).

[12] J.F. Ziegler, M.D. Ziegler, J.P. Biersack. "SRIM–The stopping and range of ions in matter (2010)." Nuclear Instruments and Methods in Physics Research Section B: Beam Interactions with Materials and Atoms 268, 1818-1823 (2010).

[13] Roger Stoller, Mychailo B. Toloczko, Gary S. Was, A.G. Certain, S. Dwaraknath, Frank A. Garner, On the use of SRIM for computing radiation damage exposure, Nucl. Instrum. Methods Phys. Res. B 310, 75-80 (2013).

[14] A.Yu. Konobeyev, U. Fischer, Y.A. Korovin, S.P. Simakov, Evaluation of effective threshold displacement energies and other data required for the calculation of advanced atomic displacement cross-sections, Nuclear Energy and Technology 3, 169–175 (2017).

[15] Schneider, C.A., Rasband, W.S., Eliceiri, K.W. "NIH Image to ImageJ: 25 years of image analysis". Nature Methods 9, 671-675, 2012.

CHAPTER 5

SUMMARY

Based on the above studies, the boundaries of the surface effect and injected interstitial effect have been identified quantitatively for all irradiations with different energies. Combining them together, a "safe analysis zone" is provided for the void swelling analysis, as figure 5.1 shown. In this figure, the boundaries of the void denuded zones are represented by the hollow circles. The ending points of the surface effect region were indicated by using the solid black squares. The solid red circles refer to the starting point of the injected interstitial effect regions. The Fe ions projected range, calculated by using SRIM, is represented by using the solid black triangles. Then, the "safe analysis zone" for void swelling studies can be defined as the shadowed blue region shown. In this safe zone, the swelling analysis will not be affected by either the surface effect and the injected interstitial effect. It should be noted that there is no safe zone for the 1 MeV irradiation because the whole region will be affected by the surface effect and injected interstitial effect.

Figure 5.1 clearly shows that the surface effect regions for all irradiations are beyond the void denuded zones (the width are measured from TEM micrographs plus the sputtering thickness loss calculated by using SRIM). The width of the surface effect region is generally twice larger than the width of the void denuded zone. The boundaries of the surface-affected zones are 202 nm (for 5 MeV), 193 nm (for 3.5 MeV), 136 nm (for 2.5 MeV), and 110 nm (for 1 MeV). As discussed in chapter 3, the local average dpa rate K will increase with the decrease of irradiation energies. Then the larger local average dpa

rate will lead to the reduction of the void denuded zone width and the surface effect region width. The K values, averaged from depth 0 to 200 nm, are 3.3×10^{-4} dpa/s for 5 MeV, 4.5×10^{-4} dpa/s for 3.5 MeV, 5.6×10^{-4} dpa/s for 2.5 MeV, and 1.1×10^{-3} dpa/s for 1 MeV. The studies found that the void denuded zone width is proportional with $(D_v/K)^{1/4}$, if normalize the value of $(D_v/K)^{1/4}$ for 5 MeV, 3.5 MeV, and 2.5 MeV irradiations by using the value of $(D_v/K)^{1/4}$ for 1 MeV irradiation, the normalized values are 1.4, 1.3 and 1.2 for 5 MeV, 3.5 MeV, and 2.5 MeV respectively. Similar to the normalized void denuded zone widths, the width of the surface effect region can be normalized based on 1 MeV irradiation. The normalized surface effect regions give 1.6, 1.5, and 1.1 for 5 MeV, 3.5 MeV, and 2.5 MeV irradiations respectively. Both the prediction and observation are in good agreement.

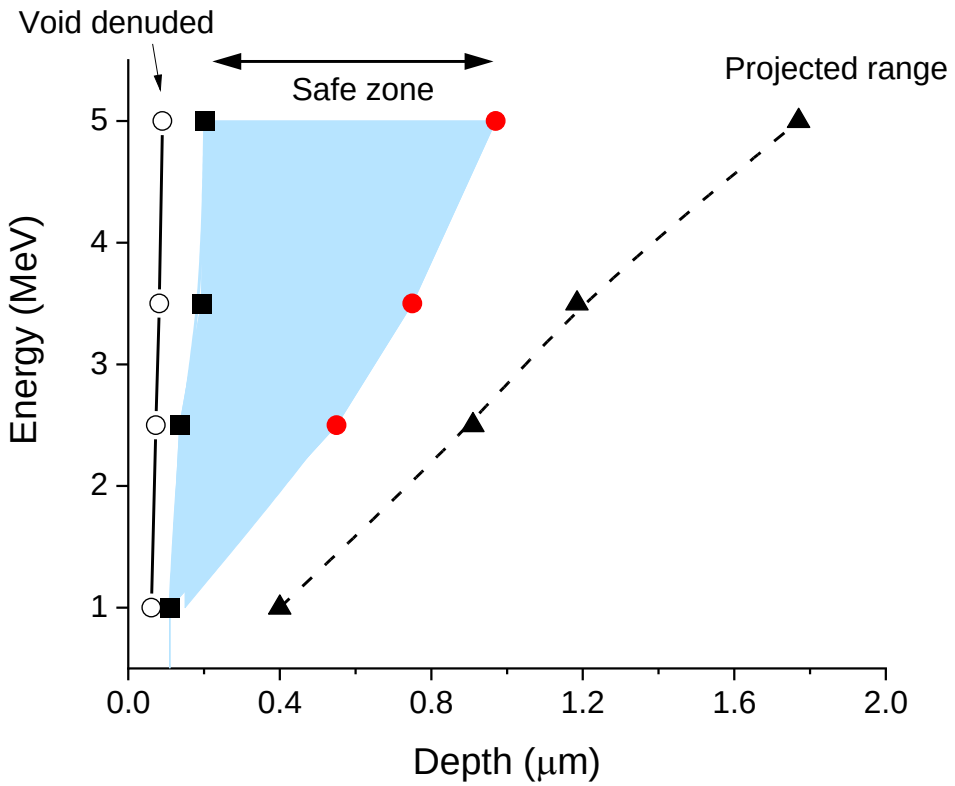

Figure 5. 1 The plots of the safe zones in Fe irradiated by self ions of different beam energies. The hollow circles refer to the void denuded zones. The solid squares refer to the boundary of the surface-effect affected zones. The solid circles refer to the boundary of the injected interstitials, The triangles refer to the projected ranges. The shadowed regions refer to the safe zones.

For the injected interstitial effect regions, the boundaries of the starting point have been quantitatively identified based on the void size changes (as figure 4.2 shown). The depths are 950 nm for 5 MeV irradiation, 750 nm for 3.5 MeV irradiation, and 550 nm for 2.5 MeV irradiation. For 1 MeV irradiation, the whole range is affected by the injected interstitial effect. That is why there is no safe zone for such low-energy irradiation. The depth of the injected interstitial effect can be normalized by using the Fe ion projected

range (the values are 1770 nm for 5 MeV, 1185 nm for 3.5 MeV, and 910 nm for 2.5 MeV, respectively). After normalization, it gives a roughly similar value for all irradiation conditions. The normalized depth of the injected interstitial effect zones is around 0.5 to 0.6, such value can be used as the approximation of the injected interstitial region.

Figure 5.2 (a)-(d) shows the distributions of the average void size as a function of local swelling for 5 MeV, 3.5 MeV, 2.5 MeV, and 1 MeV irradiations. The blue arrows show the direction of the depth increase before the region of the dpa peak location, and the red arrows show the direction of increasing depth after the region of the dpa peak location. The average void size almost shows the same tendency as a function of swelling before and after the dpa peak depth, no obvious hysteresis are observed for 5 MeV, 3.5 MeV, and 2.5 MeV irradiations. The curve of 1 MeV irradiation is different because there is no safe analysis zone for the whole irradiated region due to the reason discussed before. So the average void size vs. swelling of 1 MeV will not be discussed here.

For 5 MeV, 3.5 MeV, and 2.5 MeV irradiations, the distribution of the average void sizes shows a very similar tendency as a function of swelling. They all have the similar largest sizes around 25 to 30 nm, and the smallest sizes are also very close, around 5 to 10 nm.

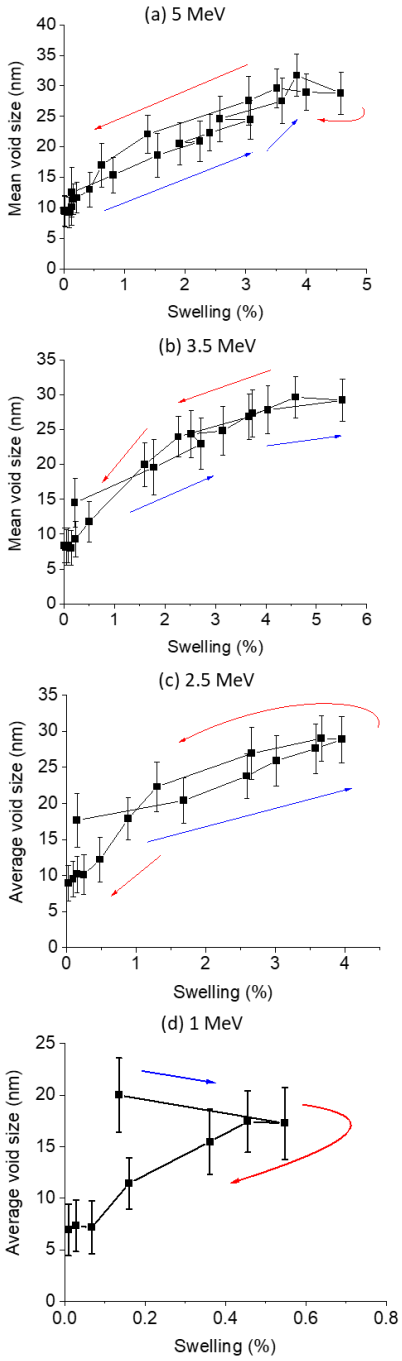

Figure 5. 2 Void sizes as a function of local swelling for Fe irradiation of (a) 5 MeV, (b) 3.5 MeV, (c) 2.5 MeV, and (d) 1 MeV.

Then, such a phenomenon indicates that the injected interstitial effect will suppress and reduce the local void swelling but will not affect the void size directly, no matter how strong of the effect is. The shrinkage of the void size is due to the change of the swelling. In other words, the injected interstitial effect can suppress the void swelling but will not influence the Ostwald ripening process itself.

Based on the safe zone as shown in figure 5.1, the distributions of void swelling as a function of local dpa for 5 MeV, 3.5 MeV, and 2.5 MeV irradiations in the safe region are selected to be shown in figure 5.3. The swelling data for 1 MeV irradiation are not shown here because there is no safe region in the whole range. The dashed line in figure 5.3 is a linear fitting curve of void swelling with local dpa. It clearly shows that the swelling data in the safe zone for all irradiations are reasonably converged to the same dependence curve. The slope of the fitting curve is given as 0.07. It means that for Fe ions irradiation to pure Fe, the void swelling rate in the safe region, which will not be affected by either the surface effect and injected interstitial effect, is 0.07% per dpa.

The study provides the methods to quantitatively identify the safe zone for data analysis of void swelling of an arbitrary ion-target system. The average void size and density as a function of local dpa and depth can be used for the determination of the surface effect region and injected interstitial effect region. Thus, no more complicated modeling process is required. The other important result is that whether voids can be observed or not after irradiation can not be used as a criterion to define the region is safe or not for swelling analysis. Because if the vacancy supersaturation is high enough, the voids can be nucleated even under the free surface or injected interstitial effect, as the 1 MeV irradiation shows.

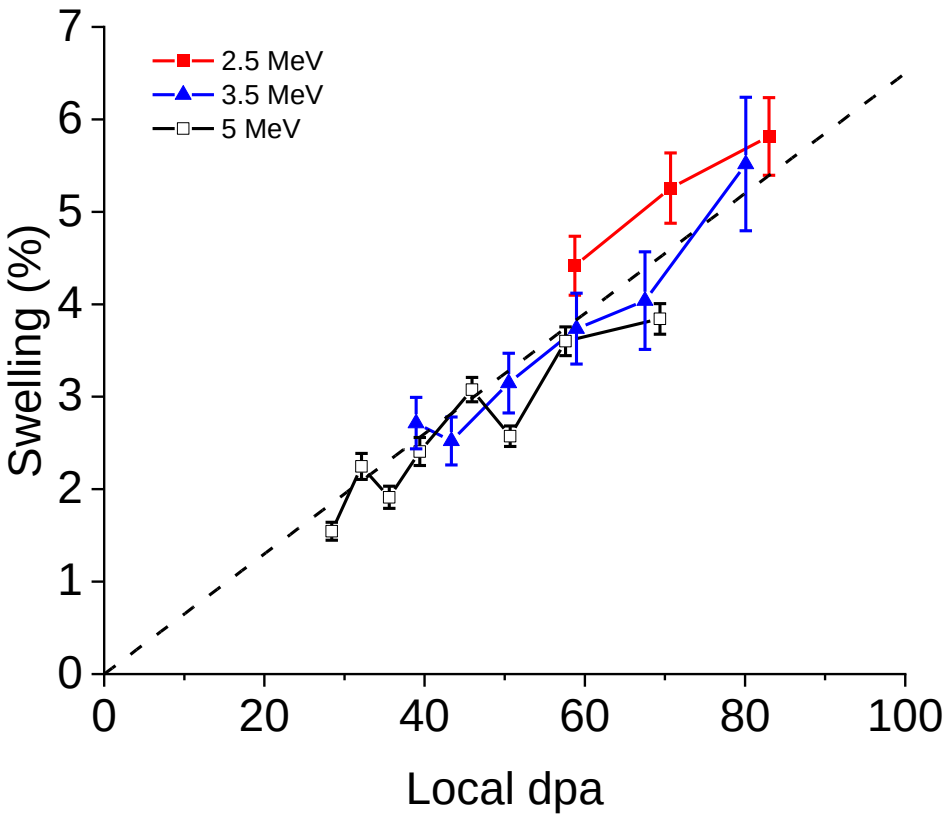

Figure 5. 3 Void swelling as a function of local dpa in Fe irradiated by 2.5 MeV, 3, MeV, and 5 MeV ions up to 100 peak dpa. Only data points in the safe zones identified in figure 5.1 are included.

In summary, the methods to quantitatively define the surface effect region and injected interstitials effect region are introduced in detail in this study based on the void swelling, void size, and void density analysis. The studies found that,

(1) The TEM measured void denuded zones are linearly proportional To $\left(\frac{exp\,(-\frac{E}{kT})}{K}\right)^{1/4}$.

(2) In the near surface region, a turnover trend is shown for the void density distribution as a function of local dpa. Such a phenomenon can be used to identify the surface effect region quantitatively. Due to the local dpa rate will increase with the decrease of irradiation energy, the width of the surface effect region will increase with the increase of irradiation energies (from 1 MeV to 5 MeV).

(3) For all irradiations, the widths of the surface effect region measured by using the above method are deeper than the width of the void denuded zone (considering the sputtering thickness loss calculated by using SRIM). Thus, whether voids appear or not cannot be used as a criterion to judge the surface effects, especially for the low-energy irradiations.

(4) The void size changes as a function of local dpa exhibit a hysteresis behavior in which voids at depth beyond the peak dpa location are systematically smaller than the depth points shallower than the peak dpa location. Thus, the deviation of void size changes can be used to quantitatively determine the depth where the injected interstitial effect begins to influence swelling.

(5) If using the projected range to normalize the corresponding injected interstitial effect width, the normalized depth of the injected interstitial affected zones is around 0.5 to 0.6, which can be used as an approximate estimation.

(6) There is no hysteresis behavior of the void size distribution as a function of local swelling. Both in the region deeper than the local dpa peak position and shallower than the dpa peak position, the void sizes roughly show the same dpa dependence distributions. It indicates that the injected interstitial effect can suppress the void swelling but will not influence the Ostwald ripening process itself. In other words, the injected interstitials will affect the void swelling but will not directly change the void size.

(7) The 1 MeV irradiation to pure Fe shows no safe zone for void analysis, even the voids can be observed from TEM micrographs after irradiation. Thus, ion irradiation testing by using accelerators at such low energy becomes questionable.

(8) The study provides useful/critical data analysis information of void swelling of an arbitrary ion-target system.